2015-04-29

Improving Channel Estimation and Tracking Performance in Distributed MIMO Communication Systems

Radu Alin David
Worcester Polytechnic Institute

Improving Channel Estimation and Tracking Performance in Distributed MIMO Communication Systems

by

Radu Alin David

A Dissertation

Submitted to the Faculty

of the

WORCESTER POLYTECHNIC INSTITUTE

In partial fulfillment of the requirements for the

Degree of Doctor of Philosophy

in

Electrical and Computer Engineering

by

May 2015

APPROVED:

Professor D. Richard Brown III, Major Advisor

Professor John A. McNeill, Department of ECE, WPI

Doctor Patrick Bidigare, BBN Technologies

Professor Andrew G. Klein, Department of Engineering and Design, WWU

To my parents.

Abstract

This dissertation develops and analyzes several techniques for improving channel estimation and tracking performance in distributed multi-input multi-output (D-MIMO) wireless communication systems. D-MIMO communication systems have been studied for the last decade and are known to offer the benefits of antenna arrays, e.g., improved range and data rates, to systems of single-antenna devices. D-MIMO communication systems are considered a promising technology for future wireless standards including advanced cellular communication systems. This dissertation considers problems related to channel estimation and tracking in D-MIMO communication systems and is focused on three related topics: (i) characterizing oscillator stability for nodes in D-MIMO systems, (ii) the development of an optimal unified tracking framework and a performance comparison to previously considered sub-optimal tracking approaches, and (iii) incorporating independent kinematics into dynamic channel models and using accelerometers to improve channel tracking performance.

A key challenge of D-MIMO systems is estimating and tracking the time-varying channels present between each pair of nodes in the system. Even if the propagation channel between a pair of nodes is time-invariant, the independent local oscillators in each node cause the carrier phases and frequencies and the effective channels between the nodes to have random time-varying phase offsets. The first part of this dissertation considers the problem of characterizing the stability parameters of the oscillators used as references for the transmitted waveforms. Having good estimates of these parameters is critical to facilitate optimal tracking of the phase and frequency offsets. We develop a new method for estimating these oscillator stability parameters based on Allan deviation measurements and compare this method to several previously developed parameter

estimation techniques based on innovation covariance whitening. The Allan deviation method is validated with both simulations and experimental data from low-precision and high-precision oscillators.

The second part of this dissertation considers a D-MIMO scenario with N_t transmitters and N_r receivers. While there are $N_t \times N_r$ node-to-node pairwise channels in such a system, there are only $N_t + N_r$ independent oscillators. We develop a new unified tracking model where one Kalman filter jointly tracks all of the pairwise channels and compare the performance of unified tracking to previously developed suboptimal local tracking approaches where the channels are not jointly tracked. Numerical results show that unified tracking tends to provide similar beamforming performance to local tracking but can provide significantly better nullforming performance in some scenarios.

The third part of this dissertation considers a scenario where the transmit nodes in a D-MIMO system have independent kinematics. In general, this makes the channel tracking problem more difficult since the independent kinematics make the D-MIMO channels less predictable. We develop dynamics models which incorporate the effects of acceleration on oscillator frequency and displacement on propagation time. The tracking performance of a system with conventional feedback is compared to a system with conventional feedback and local accelerometer measurements. Numerical results show that the tracking performance is significantly improved with local accelerometer measurements.

Acknowledgements

I would like to first thank my advisor, Rick Brown, who has been throughout the years a great professor and mentor for me. I can't stress how fortunate I have been to work with him over the years. His guidance and insight have made me a better person.

I am really thankful to have had a great dissertation committee. I would like to thank Pat Bidigare for working with me so closely and giving me a great perspective on the distributed communications world. Thank you to Professor Klein: the hardcore theory classes have prepared me for a lot of this work. And special thanks to Professor McNeill for providing me with lab equipment and great insight into phase noise and also for convincing me that analog still rules the world.

I would like to thank Kim for all the support in the lab. Her help with experiments, writing and documenting work was irreplaceable and her ability to listen to my many rants was commendable. Many thanks to Bengi who was always a window of light and serenity in stressful situations and who assured me that self-doubt was mostly misplaced. Thanks to Travis for helping me understand what a software defined radio is, especially the software side of it.

I would also like to thank my other WPI friends who have made the lab a better workplace: Rui, Sabah, Raquel, Stefan, Alex, it was great to have met you all. Thanks to Laurentiu for being my friend for the past two years. Thanks to Min for welcoming me back to WPI.

I am thankful to Professor Michalson and Professor Emanuel for preparing me for this world by being my advisors and mentors during my undergraduate years and for supporting me when I needed it most.

Finally, I would like to thank my parents, to whom I dedicate this dissertation. They have supported me unconditionally on this adventure for nine years, and I could not have done it without their trust and faith in me. I will be forever grateful.

Contents

List of Figures

List of Tables

Chapter 1

Introduction

This chapter describes the basic setting in distributed MIMO communication systems and provides motivation for the research questions considered in this dissertation.

1.1 Motivation

The last two decades have witnessed a fundamental shift in wireless communication systems away from single-antenna transceivers and toward Multi-Input Multi-Output (MIMO) communication. A MIMO system uses multiple transmit and receive antennas to exploit channel diversity and allow for multiple transmissions at the same time and on the same radio channel. The problem of multiple input multiple output systems has been studied in great detail [1–4]. MIMO techniques have resulted in several important breakthroughs for wireless devices including increased range, increased spectral efficiency, reduced interference, and improved security [1, 5–9]. The theory and practice of MIMO communication has matured to the point where MIMO is now in several recent WiFi and cellular standards including 802.11n, 802.11ac, long-term evolution (LTE), WiMAX, and International Mobile Telecommunications (IMT)-Advanced. In addition, massive MIMO systems have been proposed in which a very large number of transmit antennas is used to focus energy into a very small area [10]. The applicability of MIMO techniques is often limited, however, by physical and economic constraints. For example, the form factor of hand-held devices typically limits the number of antennas to only one or two. Consequently, the significant advantages of MIMO communication are simply not available to antenna- and/or cost-constrained devices.

While it is true that single-antenna devices are precluded from using MIMO communication techniques, it is also the case that these devices typically do not exist in isolation. Rather, single-antenna devices are often members of a network with many other single-antenna devices. If multiple devices in the network can coordinate their communication and pool their antenna resources, they can form a virtual antenna array and emulate a MIMO transceiver. This technique is called "distributed"-MIMO (D-MIMO) or virtual-MIMO in the literature [11].

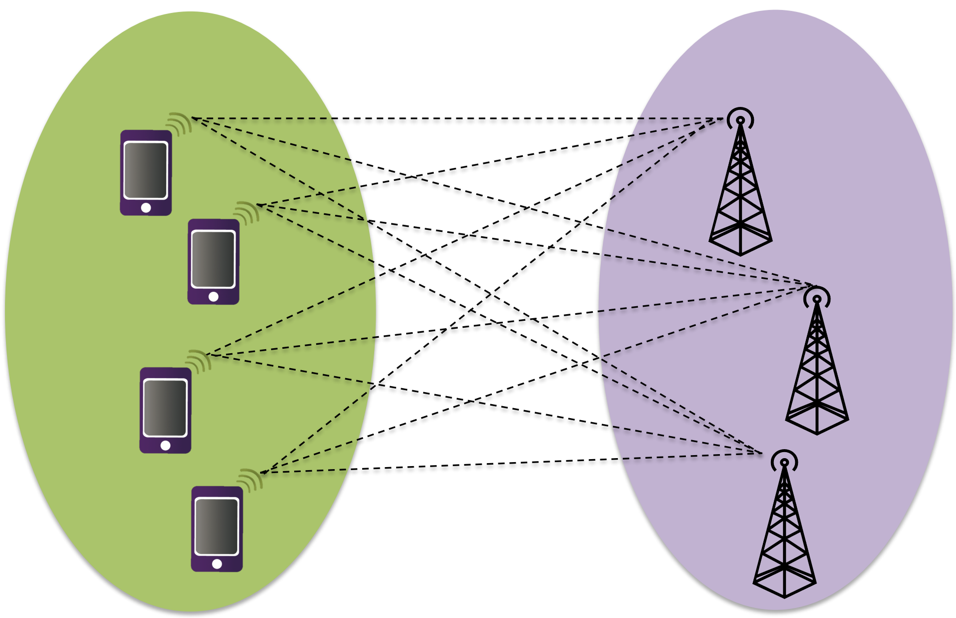

Figure 1.1: D-MIMO communication system: independent nodes can form beams.

One well-studied example of D-MIMO is distributed beamforming [12–30]. The goal in a distributed beamforming system is to control the phases and frequencies of the carriers at each transmit node so that the pass-band signals combine constructively at an intended receiver, as shown in Fig. 1.2. This results in the formation of a ”virtual” antenna that steers a beam in the direction of the receiver. Such a system can have many uses. For example, one can imagine combining multiple cellular base stations to increase the area of coverage. Or reversely, a cluster of mobile phones could benefit from such a system if they could combine their transmission to reach an out of range base-station. In wireless sensor networks, where nodes have limited transmit energy, combining transmission could lower the transmit power [31]. One could also imagine a jamming system in which a cluster of nodes could flood an malicious receiver with energy to prevent it from receiving signals.

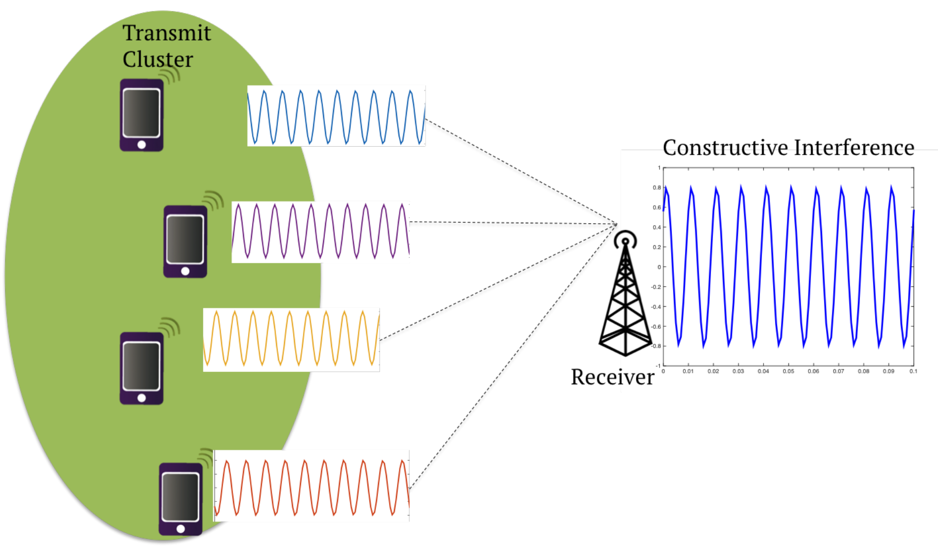

Figure 1.2: Beamforming example: Each transmitter’s carrier is aligned such that it combines at the receiver.

Similarly, distributed nullforming systems use the degrees of freedom available from many transmit antennas to combine destructively in order to protect a receiver from interference [32–34]. Fig. 1.3 shows an example system where four transmitters are aligning their signals such that the receiver sees a very small signal. This can be useful in situations where there are multiple receivers [35]. A distributed transmission cluster can cause unwanted interference from the sidelobes of a virtual beamformer array [36]. Thus, steering nulls towards a set of ”protected” receivers could allow them to communicate with other transmit clusters, as sketched in Fig. 1.4.

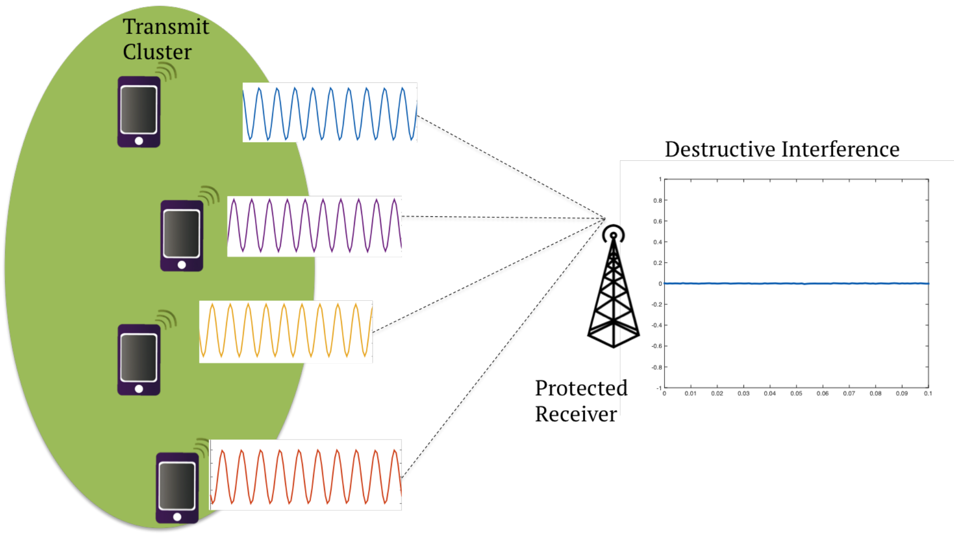

Figure 1.3: Nullforming example: The carriers are aligned such that they cancel out when reaching the receiver.

An additional challenge of nullforming compared to beamforming is that the amplitude of the signals transmitted needs to be scaled. While for beamforming the required result is the sum of all the signals, irrespective of amplitude, for nullforming there needs to be cancellation in both phase and amplitude [37].

Even in systems with time-invariant channels, the independent oscillators at each node in the distributed transmission system cause the effective channels between each transmitter and receiver to become time-varying [38] . This is due to the inherent instability of the crystal oscillators used in almost all communication systems. In a point to point single antenna communication system, such as a mobile phone connected to a cellular base station, these time-varying channels do not pose a great problem. The frequency offset can be estimated and compensated before demodulating the signal [39]. Similarly, in

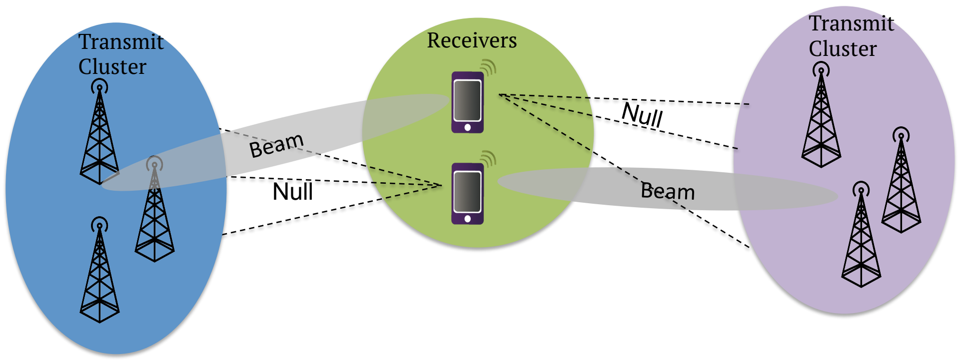

Figure 1.4: Nullforming use case: each of the two receivers only sees the beams from the respective transmit cluster.

conventional MIMO systems, the antennas at the transmitter are all driven by a single node with one oscillator. This makes it relatively straightforward to control the phases of the pass-band signals from each antenna and to steer beams and nulls. In D-MIMO systems, each antenna in the system is driven by an independent local oscillator. Even if the signals combine as a beam or null at a particular time, the oscillators will drift apart randomly over time and the beam or null will be lost. Moreover, if the nodes move, this can cause a loss of coherence. So a key challenge of D-MIMO systems is that we must be able to model and track independent oscillator dynamics and independent kinematics in order to achieve synchronization. Additional synchronization methods based on timing analysis also exist [16, 40–46]. In order to motivate the experimental work in this dissertation, in Appendix A we show the behavior of an ideal beamformer with two transmitters and one receiver. It has been shown that tracking methods, e.g., Kalman filtering, can be quite effective at estimating and predicting the time-varying phase and frequency offsets in each independent transmit/receive oscillator pair and, consequently, in enabling distributed beamforming with devices using low-cost oscillators [47, 48]. However, it is well-known that the Kalman filter requires exact knowledge of the process and measurement noise parameters [49, 50]. In the context of tracking carrier phase offsets, the Kalman filter must have exact knowledge of the short-term and long-term stability parameters of the oscillators in the system as well as exact knowledge of the statistics of the phase measurement error. In addition, the number of channels in a cluster with many transmit and receive nodes grows quickly, and tracking each of the channels can pose some challenges.

1.2 Problem Statement

In this dissertation our aim is to answer the following problems:

- How can we estimate oscillator stability parameters to ensure optimal tracking performance? Can we develop methods that accurately characterize the low-precision oscillators in commodity radios and high-precision oscillators used in recent D-MIMO field tests [51]?
- Since the number of pairwise channels typically exceeds the number of independent oscillators in D-MIMO systems, is there an optimal unified tracking framework for exploiting common information to achieve optimal tracking performance? How much better does unified tracking perform with respect to previously studied individual tracking?
- Can we incorporate kinematic effects into D-MIMO channel models? How does independent kinematics effect our ability to track and predict D-MIMO channels? Can local accelerometer measurements improve tracking performance?

These questions have lead to the results shown in this dissertation. The following chapters will answer these questions in the hope that it will prove useful to future researchers.

1.3 Dissertation Organization

The dissertation is organized as follows. After the introduction, we present a background for this work and show the parameter estimation problem in Chapter 2. We introduce the Allan variance measure, describe the experimental testbed for the results and compare the performance with covariance matrix estimation methods.

In Chapter 3 we present an analysis of different tracking methods for beamforming and nullforming. We compare the performance of using either a single large Kalman filter and multiple smaller ones to predict the channels. The results show a trade-off between performance and complexity in the implementation.

In Chapter 4 we introduce acceleration terms in the picture. We start with a one dimensional motion model and show that acceleration measurements, that could easily be obtained with an accelerometer can be integrated in the tracking problem and reduce the tracking errors. In addition, accelerometer bias is introduced and a system model that accounts for it is developed. A three-dimensional extension is then considered. Simulation results show how the motion of nodes could be mitigated.

Chapter 5 concludes the dissertation and identifies directions for future research in this field.

Chapter 2

Kalman Filter Parameter Estimation

This chapter presents a general method for computing oscillator process and measurement noise parameters from an Allan variance characterization of the carrier phase offset measurements. We propose a general experimental framework for performing stability analysis in addition to theoretical background describe the method for parameter estimation. We provide specific results for oscillators used in the N210 Universal Software Radio Peripheral (USRP) manufactured by Ettus research, as these devices are often used in experimental studies of D-MIMO systems [52]. We also provide numerical results showing precise tracking of clock phase and frequency offsets between two USRP devices with a Kalman filter. In a system with periodic channel phase measurements, our results with a 15 MHz carrier frequency show that the RMS phase prediction error is less than 25 degrees at a observation period of 2 seconds. At a 900 MHz carrier frequency, the RMS phase prediction error is less than 25 degrees at a observation period of 50 ms. In both cases, the actual tracking performance is close to the performance predicted by the Kalman filter error covariance matrices. In addition, we provide beamforming and nullforming performance results using the empirical phase prediction error statistics from the measured data using the method described in [43]. We demonstrate a scenario with beamforming power towards an intended receiver within 1 dB of ideal while nulls of -5 dB to -30 dB are also steered towards protected receivers.

2.1 Background

2.1.1 Two-state Oscillator Model

The transmit and receive nodes in the system are assumed to have independent local oscillators. These local oscillators have inherent frequency offsets and behave stochastically, causing phase offset variations in the effective channel from the transmit node to the receive node even when the propagation channels are otherwise time invariant. This section describes a discrete-time dynamic model to characterize the dynamics of the carrier phase and frequency variations between a transmitter and receiver in the D-MIMO system.

Based on the two-state models in [53, 54], we define the discrete-time state of the transmit node's carrier as $\boldsymbol{x}_t[k] = [\phi_t[k], \omega_t[k]]^\top$ where $\phi_t[k]$ and $\omega_t[k]$ correspond to the carrier phase and frequency offsets in radians and radians per second, respectively, at the transmit node with respect to an ideal carrier phase reference. The state update of the transmit node's carrier is then

$$\boldsymbol{x}_t[k+1] = \boldsymbol{F}(T)\boldsymbol{x}_t[k] + \boldsymbol{u}_t[k] \tag{2.1}$$

with

$$\boldsymbol{F}(T) = \begin{bmatrix} 1 & T \\ 0 & 1 \end{bmatrix} \tag{2.2}$$

where T is an arbitrary sampling period selected to be small enough to avoid phase aliasing at the largest expected frequency offsets.

The process noise vector $\boldsymbol{u}_t[k] \overset{\text{i.i.d.}}{\sim} \mathcal{N}(\boldsymbol{0}, \boldsymbol{Q}(T))$ causes the carrier derived from the local oscillator at the transmit node to deviate from an ideal linear phase trajectory. The covariance of the discrete-time process noise is derived from a continuous-time model in [53]:

$$\boldsymbol{Q}(T) = \omega_c^2 T \begin{bmatrix} q_1 + q_2 \frac{T^2}{3} & q_2 \frac{T}{2} \\ q_2 \frac{T}{2} & q_2 \end{bmatrix} \tag{2.3}$$

where ω_c is the nominal common carrier frequency in radians per second and q_1 (units of seconds) and q_2 (units of Hertz) are the process noise parameters corresponding to white frequency noise and random walk frequency noise, respectively.

The receive node in the system also has an independent local oscillator used to generate the carrier for down-mixing and is governed by the same dynamics as (3.2) with state $\boldsymbol{x}_r[k]$, process noise $\boldsymbol{u}_r[k] \overset{\text{i.i.d.}}{\sim} \mathcal{N}(\boldsymbol{0}, \boldsymbol{Q}(T))$, and process noise parameters q_1 and q_2 as in (3.3).

Since the receive node can only measure the relative phase and frequency of the transmit node after propagation, we define the *pairwise offset* after propagation as

$$\boldsymbol{\delta}[k] = \begin{bmatrix} \phi[k] \\ \omega[k] \end{bmatrix} = \boldsymbol{x}_t[k] + \begin{bmatrix} \psi \\ 0 \end{bmatrix} - \boldsymbol{x}_r[k].$$

Note that $\boldsymbol{\delta}[k]$ is governed by the state update

$$\boldsymbol{\delta}[k+1] = \boldsymbol{f}(T)\boldsymbol{\delta}[k] + \boldsymbol{u}_t[k] - \boldsymbol{u}_r[k]. \tag{2.4}$$

where $\boldsymbol{f}(T)$ is given in (2.2).

We assume observations are received with an observation period $T_0 = MT$ where M is a positive integer. We further assume that the observations are so short as to only provide useful phase estimates. The observations can be expressed as

$$y[k] = \boldsymbol{H}[k]\delta[k] + v[k] \tag{2.5}$$

where

$$\boldsymbol{H}[k] = \begin{cases} [1,0] & k = 0, M, 2M, \ldots \\ [0,0] & \text{otherwise} \end{cases} \tag{2.6}$$

and $v[k] \overset{\text{i.i.d.}}{\sim} \mathcal{N}(0, r)$ is the measurement noise which is assumed to be independent of the process noise. The problem then is to accurately estimate the parameters $\{q_1, q_2, r\}$ to facilitate tracking of the pairwise phase and frequency offsets in each channel. The following section introduces the concept of Allan variance, a method for characterizing oscillator stability that can be used to estimate the relevant parameters.

2.1.2 Allan Variance and Relation to the Two-state Model

The Allan variance, represented by σ_y^2, is an analysis tool used to evaluate clock stability, as well as the types of noise present in the clock [55, 56]. It is calculated using time averaging; the average of the mean squared error of the average frequencies from time τ to time t + τ is performed for all samples of the frequency signal.

The Allan variance is defined using the expectation formula:

$$\sigma_y^2(\tau) = \frac{1}{2} < (\omega_{avg}(t+\tau) - \omega_{avg}(t))^2 > \tag{2.7}$$

where

$$\omega_{avg} = \frac{1}{\tau}\int_{t-\tau}^{t} \omega(t')\, dt' = \frac{1}{\tau}[\phi(t) - \phi(t-\tau)] \tag{2.8}$$

with $\omega(t)$ as the instantaneous frequency offset and $\phi(t)$ as the phase offset. This represents a measure of the frequency stability of an oscillator over a given averaging interval τ. In [57], it is shown that the Allan variance as a function of the averaging time τ follows $\sigma_y^2(\tau) = \frac{q_1}{\tau} + \frac{q_2\tau}{3}$, where q_1 and q_2 are the respective short term and long term frequency stability parameters used in (3.3).

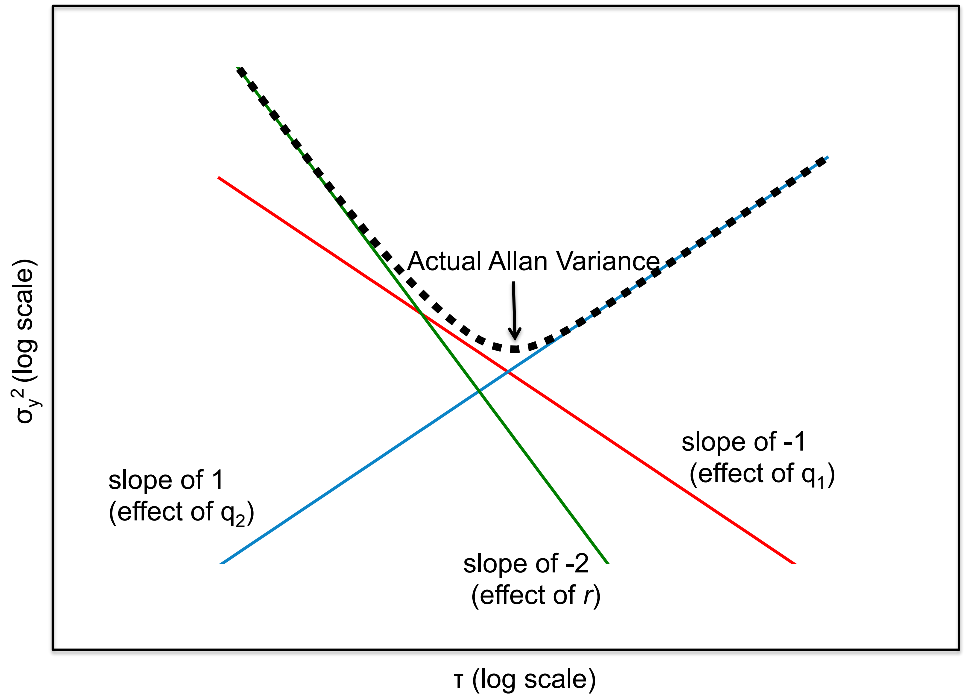

Figure 2.1: The effect of white phase noise on Allan variance.

In addition to these two parameters, the measurement noise variance r is also required for the two-state model. This can also be estimated from the Allan variance, as it has an effect on the short term measurements. Fig. 2.1 shows an example of the impact of measurement noise on the Allan deviation plot [58]. The measurement noise acts as white phase noise rather than white frequency noise and its effect scales proportionally to τ^{-2} in the Allan variance measurement [59].

Hence, to jointly estimate the process and measurement noise parameters (q_1, q_2, r), we can perform a least-squares fit the empirically-estimated Allan variance to the equation

$$\sigma_y^2(\tau) = \frac{3r}{\tau^2} + \frac{q_1}{\tau} + \frac{q_2 \tau}{3}. \tag{2.9}$$

As can be seen in Fig. 2.1, the measurement noise can have a significant impact on the Allan variance measurements, to the point where the short term stability parameter q_1 is completely obscured by the measurement noise. Nevertheless, a least squares fit can still provide an upper bound on the q_1 parameter.

2.1.3 Kalman Filter Tracking

The Kalman filter is an algorithm that computes the minimum mean squared error (MMSE) estimate of a set of states based on a given model and a set of observations [60–62]. Based on the 2-state model described in Section 3.2.1, we can implement a Kalman filter to track and predict the phase offset given periodic observations. Note that the Kalman filter specified below is updated at the sampling period T while observations are received with period $T_0 = MT$. The one-step state prediction $\hat{\delta}[k+1|k]$ is given as

$$\hat{\boldsymbol{\delta}}[k+1|k] = \boldsymbol{F}(T)\hat{\boldsymbol{\delta}}[k|k] \tag{2.10}$$

with state estimate

$$\hat{\boldsymbol{\delta}}[k|k] = \hat{\boldsymbol{\delta}}[k|k-1] + \boldsymbol{K}[k](y[k] - \boldsymbol{H}[k]\hat{\boldsymbol{\delta}}[k|k-M]). \tag{2.11}$$

The Kalman gain is given as

$$\boldsymbol{K}[k] = \boldsymbol{\Sigma}[k|k-1]\boldsymbol{H}^\top[k](\boldsymbol{H}[k]\boldsymbol{\Sigma}[k|k-1]\boldsymbol{H}^\top[k] + r)^{-1}.$$

The quantity $\boldsymbol{\Sigma}[k|k-1]$ denotes the one-step prediction error covariance matrix (ECM) which is used in the computation of the estimation error covariance matrix as

$$\boldsymbol{\Sigma}[\boldsymbol{k}|\boldsymbol{k}] = \boldsymbol{\Sigma}[k|k-1] - \boldsymbol{K}[k]\boldsymbol{H}[k]\boldsymbol{\Sigma}[k|k-1] \tag{2.12}$$

with the Kalman filter recursion

$$\boldsymbol{\Sigma}[k+1|k] = \boldsymbol{F}(T)\boldsymbol{\Sigma}[k|k]\boldsymbol{F}(T)^\top + \boldsymbol{Q}(T) \tag{2.13}$$

Note that the process noise covariance $\boldsymbol{Q}(T)$ accounts for the effect of the process noise at both the transmitter and at the receiver. Given measurements at sample instants $k = 0, M, 2M, \ldots$, we denote the Kalman filter's MMSE phase prediction at sample instant $\ell > k$ as $\hat{\phi}[\ell \mid k]$.

Finally, to evaluate the performance of our tracking mechanism, we compare the error between the actual phase measurements $y[\ell]$ and the predictions $\hat{\phi}[\ell \mid k]$ with the ECM result $\boldsymbol{\Sigma}[k+\ell|k]$. The squared phase measurement errors are averaged over multiple runs of the Kalman filter to obtain an empirical estimate of the steady-state behavior.

2.1.4 Covariance Estimation Methods for Kalman Filtering

We have shown in section 3.2.1 that the behavior of the two-state model can be fully characterized by the process noise covariance $\boldsymbol{Q}(T)$ and the measurement noise r. Hence, a Kalman filter algorithm that has knowledge of these elements can successfully track the states of the system, in our case the phase and frequency of an oscillator. However, in practice it is difficult to have exact parameters for the process and measurement noise, and a mismatch between the actual model and the Kalman filter parameters can lead to sub-optimal performance [49]. Fig. 2.2 shows a simulation of two scenarios: a run where a Kalman filter is used to track a two-state model sequence with correct parameters and with slightly off parameters. Although a difference of four orders of magnitude in the parameters may seem very large, in reality even larger errors may appear.

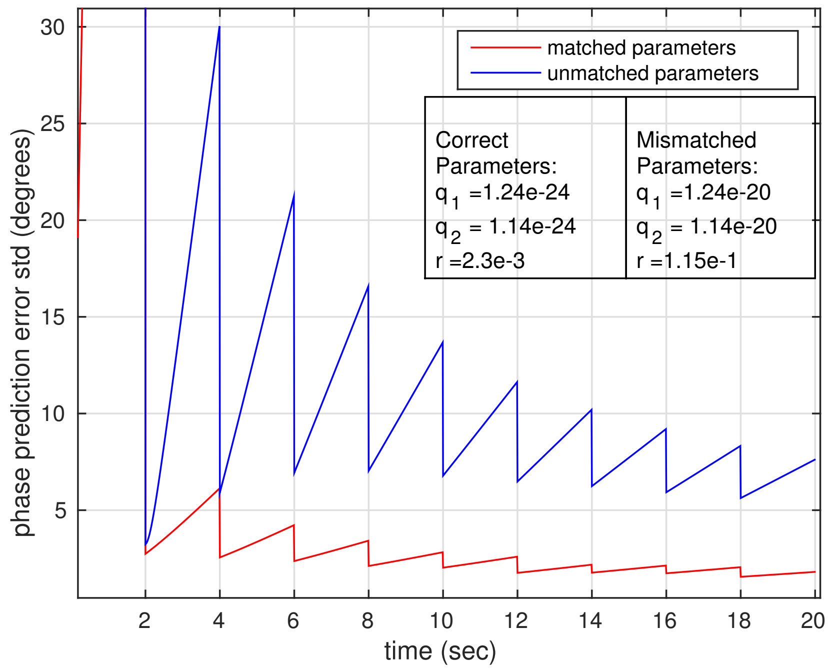

Figure 2.2: Kalam filter parameter mismatch problem: phase prediction standard deviation.

In section 2.1.2 we have shown how the Allan variance can be used to extract these parameters. In order to compare our method with other approaches, we have considered approaches based on innovation whitening and adaptive Kalman filtering as proposed in [63, 64]. These methods offer a general approach to the estimation of the process noise covariance matrix $\boldsymbol{Q}(T)$ and measurement noise matrix $\boldsymbol{R}$. Note that in the two-state model the measurement noise is scalar since we assume a scalar observation.

Mehra describes a procedure with the following steps [63]:

1. Guess at the unknown parameters and save the innovation sequence

$$\boldsymbol{\nu}[k] = \boldsymbol{y}[k] - H\hat{\boldsymbol{\delta}}[k|k-1] \tag{2.14}$$

where $\hat{\boldsymbol{\delta}}[k|k-1]$ is the MMSE Kalman filter prediction of the state $\boldsymbol{\delta}[k]$ given observations $\boldsymbol{y}[0], \ldots, \boldsymbol{y}[k-1]$.

2. Estimate the autocorrelation function of the innovations by computing the sample autocorrelations

$$\boldsymbol{C}_i = \frac{1}{N} \sum_{n=1}^{N} \boldsymbol{\nu}[k]\boldsymbol{\nu}[k-i] \tag{2.15}$$

for $i = \{0, 1, \ldots n\}$. The estimator specified above is biased but has minimum variance. Mehra mentions that an unbiased estimator can also be used at the cost of increased variance. In either case, perform a hypothesis test to determine if the innovation sequence is white.

3. The parameter estimation procedure has the following inputs:

   (a) Estimated steady-state innovation autocorrelations $\{\boldsymbol{C}_0, \boldsymbol{C}_1, \ldots, \boldsymbol{C}_8\}$ with $\boldsymbol{C}_i \approx \mathrm{E}[\boldsymbol{\nu}[k]\boldsymbol{\nu}[k-i]]$.

   (b) The steady-state Kalman gain K from the Kalman filter run in step 1.

   The parameter estimation procedure has three steps:

   (a) Compute the matrix

$$z = B^{-1} \begin{bmatrix} \boldsymbol{C}_1 + HFK\boldsymbol{C}_0 \\ \boldsymbol{C}_2 + HFK\boldsymbol{C}_1 + HF^2K\boldsymbol{C}_1 \\ \vdots \\ \boldsymbol{C}_n + HFK\boldsymbol{C}_{n-1} + \cdots + HF^nK\boldsymbol{C}_0 \end{bmatrix} \tag{2.16}$$

where

$$B = \begin{bmatrix} HF \\ HF^2 \\ \vdots \\ HF^{n-1} \end{bmatrix}. \tag{2.17}$$

(b) Estimate the measurement noise variance matrix as

$$\boldsymbol{R} = \boldsymbol{C}_0 - Hz \tag{2.18}$$

(c) Estimate the stability parameters:

$$\sum_{j=0}^{k-1} HF^j Q (F^{j-k})^\top H^\top = z^\top (F^(-k)^\top H^\top - HF^k z - \sum_{j=0}^{k-1} HF^j \hat{\Omega} (F^{j-k)})^\top H^\top \tag{2.19}$$

for $k = 1, \ldots, n$ and

$$\hat{\Omega} = F \left(-Kz^\top - zK^\top + \boldsymbol{C}_0 KK^\top \right) F^\top. \tag{2.20}$$

2.2 Mehra Method for the Two-state Model

Below, we provide specific details of the procedure described in 2.1.4 for the two-state dynamic model with unknown process and measurement noise parameters described in Section 3.2.1.

2.2.1 Overview of Mehra Procedure

Mehra describes a procedure with the following steps:

1. Guess at the unknown parameters $\{q_1^2, q_2^2, r\}$ and run a Kalman filter. Store the

innovation sequence

$$\nu[k] = y[k] - H\hat{x}[k|k-1] \tag{2.21}$$

where $\hat{x}[k|k-1]$ is the MMSE Kalman filter prediction of the state $x[k]$ given observations $y[0], \ldots, y[k-1]$.

2. Estimate the autocorrelation function of the innovations by computing the sample autocorrelations

$$c_i = \frac{1}{N}\sum_{n=1}^{N} \nu[k]\nu[k-i] \tag{2.22}$$

for $i = \{0, 1, 2\}$. The estimator specified above is biased but has minimum variance. Mehra mentions that an unbiased estimator can also be used at the cost of increased variance. In either case, perform a hypothesis test to determine if the innovation sequence is white. If the test indicates the innovation sequence is white, then the process and measurement noise parameters are optimal. If the test indicates the sequence is not white, then we can use the autocorrelation of the innovation sequence in the following parameter estimation procedure to generate better estimates for $\{q_1^2, q_2^2, r\}$.

3. The parameter estimation procedure has the following inputs:

   (a) Estimated steady-state innovation autocorrelations $\{c_0, c_1, c_2\}$ with $c_i \approx \mathrm{E}[v[k]v[k-i]]$.

   (b) The steady-state Kalman gain K from the Kalman filter run in step 1.

   The parameter estimation procedure has three steps:

(a) From Mehra equation (21), compute the 2×1 vector

$$z = B^{-1} \begin{bmatrix} c_1 + c_0 HFK \\ c_2 + c_1 HFK + c_0 HF^2 K \end{bmatrix} \tag{2.23}$$

with

$$B = \begin{bmatrix} HF \\ HF^2 \end{bmatrix}. \tag{2.24}$$

(b) Estimate the measurement noise variance as

$$r = c_0 - Hz \tag{2.25}$$

(c) Estimate the process noise parameters $\{q_1^2, q_2^2\}$ by computing

$$\begin{bmatrix} \omega_0^2 q_1^2 \\ \omega_0^2 q_2^2 \end{bmatrix} = \begin{bmatrix} \frac{4}{3T} & \frac{-1}{6T} \\ \frac{2}{T^3} & \frac{-1}{T^3} \end{bmatrix} \begin{bmatrix} b_1 \\ b_2 \end{bmatrix} \tag{2.26}$$

where

$$b_1 = z^\top F^{-\top} H^\top - HFz - H\hat{\Omega} F^{-\top} H^\top \tag{2.27}$$

$$b_2 = z^\top (F^{-2})^\top H^\top - HF^2 z - H\hat{\Omega}(F^{-2})^\top H^\top - HF\hat{\Omega}(F^{-1})^\top H^\top \tag{2.28}$$

with $F^{-\top} = (F^{-1})^\top$ and

$$\hat{\Omega} = F\left(-Kz^\top - zK^\top + c_0 KK^\top\right) F^\top. \tag{2.29}$$

The details of how we derived these equations from Mehra are provided in the following section.

4. Mehra says the process can be repeated (go back to step 1) but that good estimates are usually generated after one pass. Our numerical tests have shown this to be true. The Mehra estimates don't appear to significantly change after one iteration of the method.

2.2.2 Solving for the Process Noise Parameters

In this section, we provide the details of the analysis that resulted in the equations in step 3.c of the parameter estimation procedure. The analysis here is necessary to separate the unknown parameters from the known/estimated quantities and to form a set of linear equations by which we can estimate the unknown parameters. We denote $F^{-\top} = (F^{-1})^{\top}$. From Mehra's equation (28) with $k = 1$, we have

$$HQF^{-\top}H^{\top} = z^{\top}F^{-\top}H^{\top} - HFz - H\hat{\Omega}F^{-\top}H^{\top}. \tag{2.30}$$

From Mehra's equation (28) with $k = 2$, we have

$$\begin{aligned} &HQ(F^{-2})^{\top}H^{\top} + HFQF^{-\top}H^{\top} = \\ &\qquad z^{\top}(F^{-2})^{\top}H^{\top} - HF^{2}z - H\hat{\Omega}(F^{-2})^{\top}H^{\top} - HF\hat{\Omega}(F^{-1})^{\top}H^{\top} \end{aligned} \tag{2.31}$$

A few preliminary results will be useful:

$$F^{-\top} = \begin{bmatrix} 1 & 0 \\ -T & 1 \end{bmatrix} \tag{2.32}$$

$$F^2 = \begin{bmatrix} 1 & 2T \\ 0 & 1 \end{bmatrix} \tag{2.33}$$

$$(F^{-2})^\top = \begin{bmatrix} 1 & 0 \\ -2T & 1 \end{bmatrix} \tag{2.34}$$

- **Equation (2.30)**

  We can rewrite the lefthand side of (2.30) as

$$HQF^{-\top}H^\top = \begin{bmatrix} 1 & 0 \end{bmatrix} \left(\omega_0^2 q_1^2 \begin{bmatrix} T & 0 \\ 0 & 0 \end{bmatrix} + \omega_0^2 q_2^2 \begin{bmatrix} \frac{T^3}{3} & \frac{T^2}{2} \\ \frac{T^2}{2} & T \end{bmatrix} \right) \begin{bmatrix} 1 & 0 \\ -T & 1 \end{bmatrix} \begin{bmatrix} 1 \\ 0 \end{bmatrix} \tag{2.35}$$

$$= \begin{bmatrix} 1 & 0 \end{bmatrix} \left(\omega_0^2 q_1^2 \begin{bmatrix} T & 0 \\ 0 & 0 \end{bmatrix} + \omega_0^2 q_2^2 \begin{bmatrix} \frac{T^3}{3} & \frac{T^2}{2} \\ \frac{T^2}{2} & T \end{bmatrix} \right) \begin{bmatrix} 1 \\ -T \end{bmatrix} \tag{2.36}$$

$$= T\omega_0^2 q_1^2 - \frac{T^3}{6}\omega_0^2 q_2^2 \tag{2.37}$$

$$= \begin{bmatrix} T & -T^3/6 \end{bmatrix} \begin{bmatrix} \omega_0^2 q_1^2 \\ \omega_0^2 q_2^2 \end{bmatrix} \tag{2.38}$$

  There is no need to simplify the righthand side of (2.30) since this can just be computed directly in Matlab. We denote

$$b_1 = z^\top F^{-\top} H^\top - HFz - H\hat{\Omega} F^{-\top} H^\top \tag{2.39}$$

and our first linear equation is then

$$\begin{bmatrix} T & -T^3/6 \end{bmatrix} \begin{bmatrix} \omega_0^2 q_1^2 \\ \omega_0^2 q_2^2 \end{bmatrix} = b_1. \tag{2.40}$$

- **Equation (2.31)** We can rewrite the first term in the left-hand side of (2.31) as

$$HQ(F^{-2})^\top H^\top = \begin{bmatrix} 1 & 0 \end{bmatrix} \left(\omega_0^2 q_1^2 \begin{bmatrix} T & 0 \\ 0 & 0 \end{bmatrix} + \omega_0^2 q_2^2 \begin{bmatrix} \frac{T^3}{3} & \frac{T^2}{2} \\ \frac{T^2}{2} & T \end{bmatrix} \right) \begin{bmatrix} 1 & 0 \\ -2T & 1 \end{bmatrix} \begin{bmatrix} 1 \\ 0 \end{bmatrix} \tag{2.41}$$

$$= \begin{bmatrix} 1 & 0 \end{bmatrix} \left(\omega_0^2 q_1^2 \begin{bmatrix} T & 0 \\ 0 & 0 \end{bmatrix} + \omega_0^2 q_2^2 \begin{bmatrix} \frac{T^3}{3} & \frac{T^2}{2} \\ \frac{T^2}{2} & T \end{bmatrix} \right) \begin{bmatrix} 1 \\ -2T \end{bmatrix} \tag{2.42}$$

$$= T\omega_0^2 q_1^2 - \frac{2T^3}{3}\omega_0^2 q_2^2. \tag{2.43}$$

We can rewrite the second term in the left-hand side of (2.31) as

$$HFQF^{-\top} H^\top = \begin{bmatrix} 1 & 0 \end{bmatrix} \begin{bmatrix} 1 & T \\ 0 & 1 \end{bmatrix} \left(\omega_0^2 q_1^2 \begin{bmatrix} T & 0 \\ 0 & 0 \end{bmatrix} + \omega_0^2 q_2^2 \begin{bmatrix} \frac{T^3}{3} & \frac{T^2}{2} \\ \frac{T^2}{2} & T \end{bmatrix} \right) \begin{bmatrix} 1 & 0 \\ -T & 1 \end{bmatrix} \begin{bmatrix} 1 \\ 0 \end{bmatrix} \tag{2.44}$$

$$= \begin{bmatrix} 1 & T \end{bmatrix} \left(\omega_0^2 q_1^2 \begin{bmatrix} T & 0 \\ 0 & 0 \end{bmatrix} + \omega_0^2 q_2^2 \begin{bmatrix} \frac{T^3}{3} & \frac{T^2}{2} \\ \frac{T^2}{2} & T \end{bmatrix} \right) \begin{bmatrix} 1 \\ -T \end{bmatrix} \tag{2.45}$$

$$= T\omega_0^2 q_1^2 - \frac{2T^3}{3}\omega_0^2 q_2^2. \tag{2.46}$$

Hence, (2.31) can be written as

$$\begin{bmatrix} 2T & -4T^3/3 \end{bmatrix} \begin{bmatrix} \omega_0^2 q_1^2 \\ \omega_0^2 q_2^2 \end{bmatrix} = b_2 \tag{2.47}$$

with

$$b_2 = z^\top (F^{-2})^\top H^\top - HF^2 z - H\hat{\Omega}(F^{-2})^\top H^\top - HF\hat{\Omega}(F^{-1})^\top H^\top \tag{2.48}$$

from the right-hand side of (2.31).

- **Final Equations** The linear equations we must solve to estimate the process noise parameters are then

$$\underbrace{\begin{bmatrix} T & -T^3/6 \\ 2T & -4T^3/3 \end{bmatrix}}_{A} \begin{bmatrix} \omega_0^2 q_1^2 \\ \omega_0^2 q_2^2 \end{bmatrix} = \begin{bmatrix} b_1 \\ b_2 \end{bmatrix}. \tag{2.49}$$

If $T \neq 0$, the A matrix is invertible. We can write

$$A^{-1} = \begin{bmatrix} \frac{4}{3T} & \frac{-1}{6T} \\ \frac{2}{T^3} & \frac{-1}{T^3} \end{bmatrix}. \tag{2.50}$$

Hence, this procedure will result in a unique solution for the process noise parameters q_1^2 and q_2^2 and the measurement noise parameter r.

2.3 Methodology for Numerical Results

The results in this chapter are based on experimental data gathered with the USRP N210 software defined radio platform. These devices are designed for RF communications and are commonly used in research and academic settings as well as for rapid development in industrial and defense applications [65]. A more detailed description of the experiment testbed and data acquisition procedure can be seen in Appendix B. The platform contains an FPGA used to stream data between the device and a host computer and it has the ability to operate from DC to 6 GHz via interchangeable daughterboards. The intended use is for the host computer to handle the baseband processing and to configure the RF parameters, while the upconversion/downconversion and the filters required to bring the signals to RF frequencies are performed by the device.

2.3.1 Data Acquisition

The USRPs used in the final experiments had the FPGA configured to upconvert/downconvert I/Q data and to interface with the host computer. The interchangeable daughterboards that are used to reach different carrier frequency bands have a frequency range of $1\ \mathrm{MHz} - 250\ \mathrm{MHz}$. Fig. 2.3 shows the main components of the experimental setup. All the experiments were performed with the USRPs connected by a coaxial cable to eliminate any effects such as multipath and time-varying channel dynamics and to focus only on the carrier phase and frequency dynamics of the USRPs.

Rather than using a separate sampler to record the signals generated by the USRP hardware, our system uses two USRPs with separate but otherwise identical oscillators. By using identical oscillators, the combined effect of the two independent but otherwise identical oscillators is statistically twice the effect of just one oscillator, i.e., the effective process noise covariance is twice that of a single oscillator. This allows us to statistically characterize the process noise parameters of an individual USRP oscillator.

The ethernet port allows for gigabit ethernet data transfer between the USRP and the host computer. This connection allows for real time data gathering and analysis even at high sampling rates. The USRP internal clock is a single 10MHz oscillator that is converted to the desired carrier frequencies using PLLs.

The transmit power of the USRP was measured to be approximately $-2\ \mathrm{dBm}$ and an attenuator of $36\ \mathrm{dB}$ was placed on the wired communication link to achieve $-38\ \mathrm{dBm}$ of receive power. The main steps of the experiment are shown below, together with the

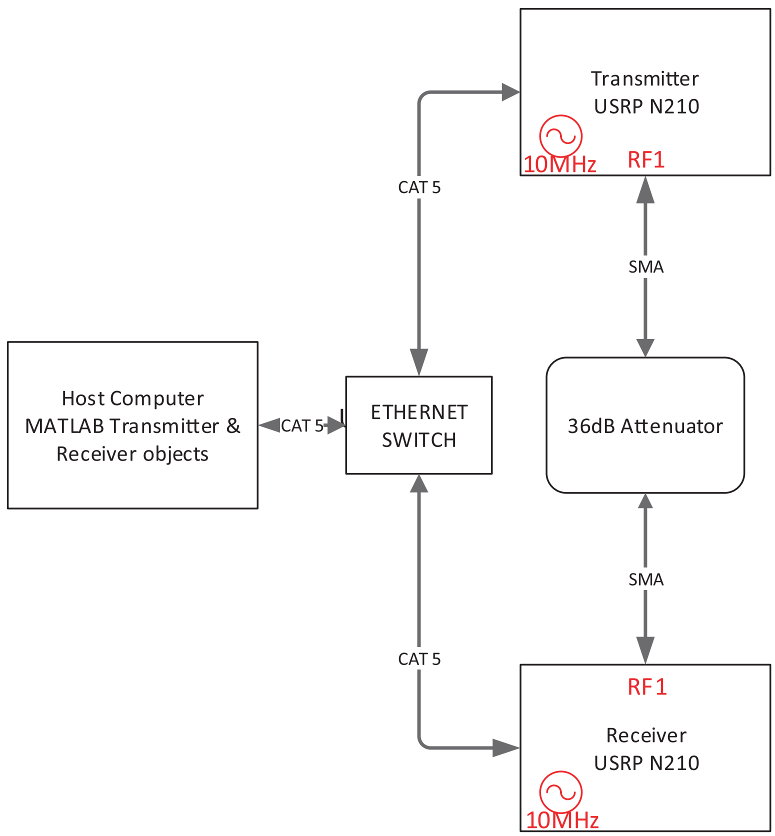

Figure 2.3: Experimental setup for data acquisition.

description of the waveforms at each of the steps.

1. Generate a complex tone at a baseband frequency f so that the baseband signal is

$$s_t[k] = A_t e^{j2\pi f k} \tag{2.51}$$

   where A_t is the transmitter gain.

2. The transmit USRP modulates the tone with the specified carrier frequency and transmits it over the wire. The transmitted signal is given as

$$w[k] = A_t \cos((2\pi(f + f_c)k + \phi_t[k])) \tag{2.52}$$

   where $\phi_t[k]$ represents the time-varying phase offset introduced by the transmitter.

3. The receive USRP demodulates the received tone, samples it and sends it to the host computer. The resulting baseband signal is given as

$$\begin{aligned} s_r[k] &= A_t g A_r e^{j(2\pi((f+f_c)-f_c)k+\phi_t[k]-\phi_r[k]+\psi)} \\ &= A e^{j(2\pi f k+\phi[k])} \end{aligned} \tag{2.53}$$

   where g is the channel gain, A_r is the receiver gain, and $\phi[k] = \phi_t[k] - \phi_r[k] + \psi$ represents the total transmitter-receiver phase offset, including the channel propagation phase ψ. In practice, this measurement will be corrupted by noise which is modeled as the observation in (2.5). Thus, our observation will be $y[k] = \phi[k] + v[k]$.

4. The received complex data is stored on the host computer in double precision floating point format for further analysis.

We performed experiments at two nominal carrier frequencies: 15 MHz and 900 MHz. In both cases, the baseband tone frequency was set to $f = 2000$ Hz and the baseband sampling frequency at the receiver was set to $f_s = 100 \times 10^6/512\,\mathrm{MHz} = 195,312.5\,\mathrm{Hz}$. In the 15 MHz experiments, the *Basic TX* and *Basic RX* USRP daughter boards were used and in the 900 MHz experiments, the *SBX* USRP daughter boards were used [66].

The baseband sampling frequency at the receiver was selected to avoid aliasing. Based on earlier experiments, the largest recorded frequency offset on the USRP N210s we observed was approximately 45 kHz at a 900 MHz carrier frequency, and less than 1 kHz for a carrier frequency of 15 MHz. The USRP hardware uses a 12-bit ADC with a nominal sampling frequency of 100 MHz that can be later decimated by any value between 4 and 512 leading to the minimum sampling frequency of $100\,\mathrm{MHz}/512 = 195,312.5\,\mathrm{Hz}$. This sampling frequency was used for all of our experiments.

All data processing is done on the host computer connected to the N210 USRPs via gigabit ethernet cables. Transmitter and receiver objects are instantiated in MATLAB on two separate USRPs. The transmit radio is configured to transmit the $2000\mathrm{Hz}$ complex tone and the receive radio is configured to demodulate the data and save it as a complex variable. The duration of each experiment was approximately ten minutes.

2.3.2 Data Analysis

Since we need to obtain the unwrapped phase of the signal as our observations, we will need to process the in-phase and quadrature components of the received data. The procedure is described in the steps below using MATLAB functions:

1. First we compute the angle of the complex data x. In this case, x is a complex data type of length L samples.

```
phi = angle(double(x));
```

   This generates a wrapped phase vector with values between $[-\pi, \pi]$.

2. We unwrap the phase:

```
phi_unwrapped = unwrap(phi);
```

At this point the phase vector contains the expression: $2\pi fk + \phi[k]$ from equation 2.53.

3. We need to remove the linear frequency component using the *detrend* function:

```
phi_detrended = detrend(phi_unwrapped);
```

This generates the phase vector $\phi[k]$ with the sampling frequency of 195,312.5 Hz. This frequency is too large for our calculations.

4. We decimate it by a factor of 125 using a custom function. Note that this also filters the high frequency components from the phase signal.

```
phi_decimated = decimate_variable(phi_detrended,fs,1562.5);
```

In this function, *fs* is the initial sampling frequency and 1562.5 is the final sampling frequency.

By taking the unwrapped phase from the complex baseband signal in equation2.53 and removing the linear frequency trend, we obtain the zero mean phase offset progression *phi_decimated*. This is the term that we use in our Allan variance characterization of the oscillators, and subsequent evaluation of the tracking performance.

2.4 Numerical Results

2.4.1 USRP Results

This section presents the numerical results outlining the process of obtaining accurate Kalman Filter parameters and the performance evaluation of our implementation. All the analysis is performed on real data obtained from the USRP N210 platform and prediction errors are computed with respect to the measurements. The empirically-estimated prediction variances are also compared to the variances provided by the Kalman filter's error covariance matrices.

Fig. 2.4 shows examples of unwrapped phase offset realizations for multiple experiments. This data was detrended and decimated by a factor of 125. As expected, these results show the significant phase variations caused by the stochastic behavior of the independent oscillators in the system.

The phase offset data is then used in the calculation of Allan deviation and subsequent parameter estimation. Fig. 2.5 illustrates the individual effect of measurement noise and short and long term stability parameters on the Allan deviation result. It can be seen that the measurement noise has a large impact on the short term measurements, making the q_1 parameter difficult to estimate.

Table 4.2 shows the range of parameters that were determined over five separate experiments. The q_1 and q_2 parameters in the table are divided by 2 in order to account for the effect of both the transmitter and receiver clocks. This is due to the combining of the noise process of the two nodes, as shown in (3.4).

15 MHz Phase Tracking and Prediction Experiments

Figure 2.6 shows the RMS phase prediction error of a Kalman filter tracker compared to the RMS prediction error from the Kalman filter's error covariance matrix. This re-

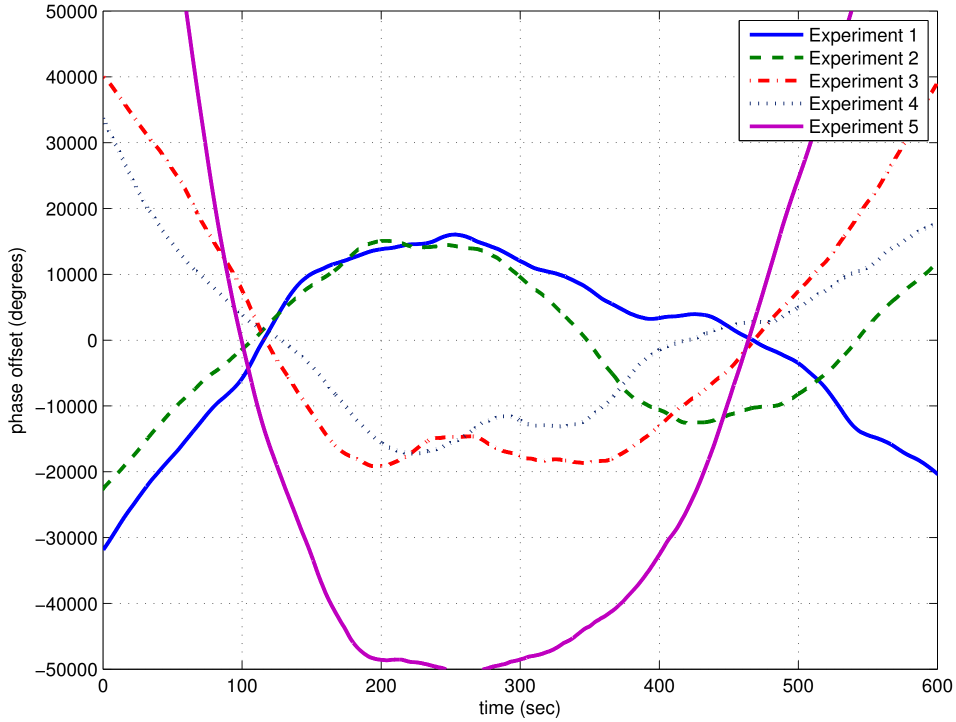

Figure 2.4: Experimental unwrapped phase offsets between two USRP N210 nodes at 15 MHz.

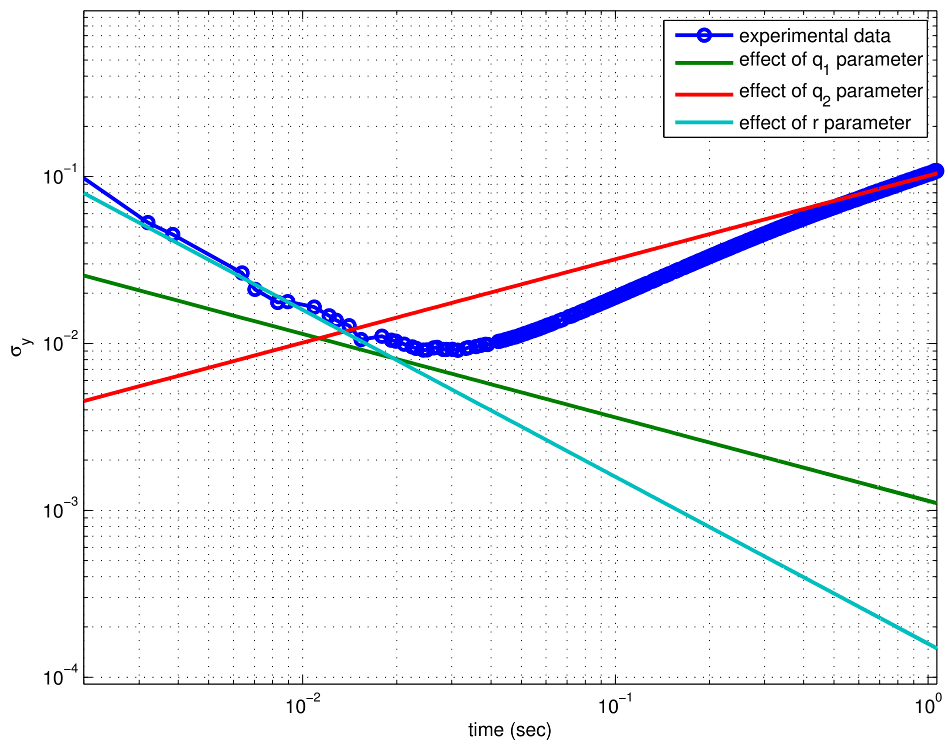

Figure 2.5: Least-squares parameter fit with experimental Allan deviation results.

Parameter	units	min value	max value
r	rad^2	1.6×10^{-8}	3.3×10^{-8}
q_1	sec	1.4×10^{-22}	3.02×10^{-21}
q_2	Hz	2.62×10^{-18}	6.31×10^{-18}

Table 2.1: USRP VCXO measurement noise, short-term stability and long-term stability parameter ranges estimated over five separate experiments.

sult shows that at a observation period of $T_0 = 2$ seconds, the maximum RMS phase prediction error is less than 25 degrees after the Kalman filter achieves steady-state. In addition, the plot shows that the phase prediction error is consistent with the performance predictions from the Kalman filter error covariance matrix.

By varying the observation period T_0, it is possible to get an idea of the expected phase offset error and to choose the value that meets the phase offset requirements of a given system. The Kalman filter phase prediction performance is plotted with respect to the observation period T_0 in Fig. 2.7. These results show that the RMS phase prediction

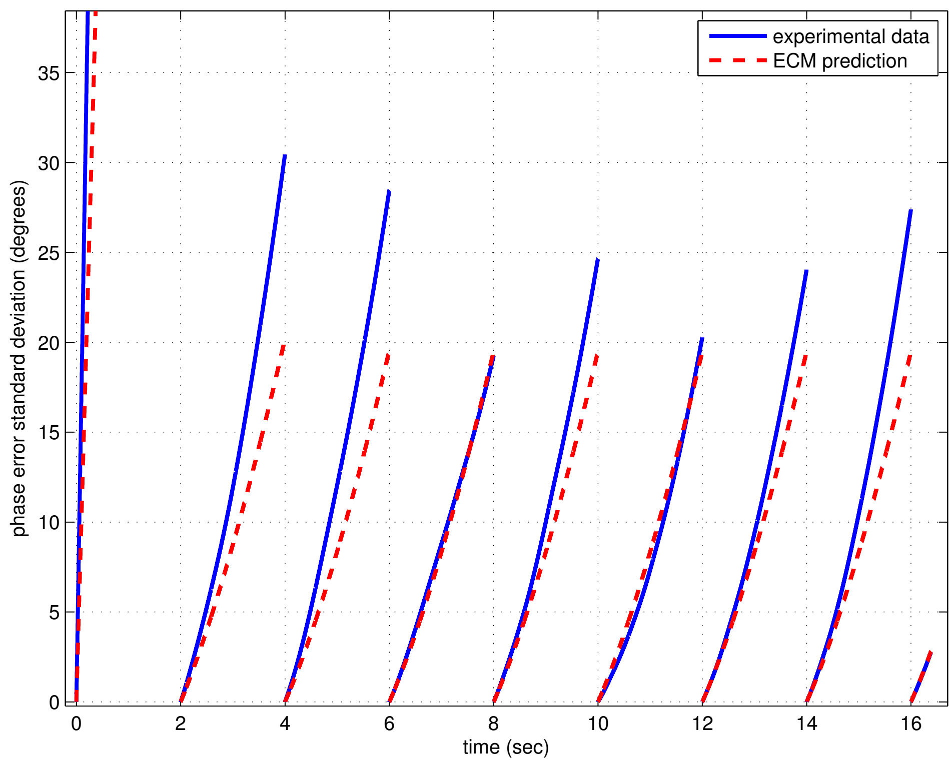

Figure 2.6: Kalman filter RMS phase error at 15 MHz with observation period $T_0 = 2$ seconds.

error with measured data is quite close to the error covariance matrix predictions.

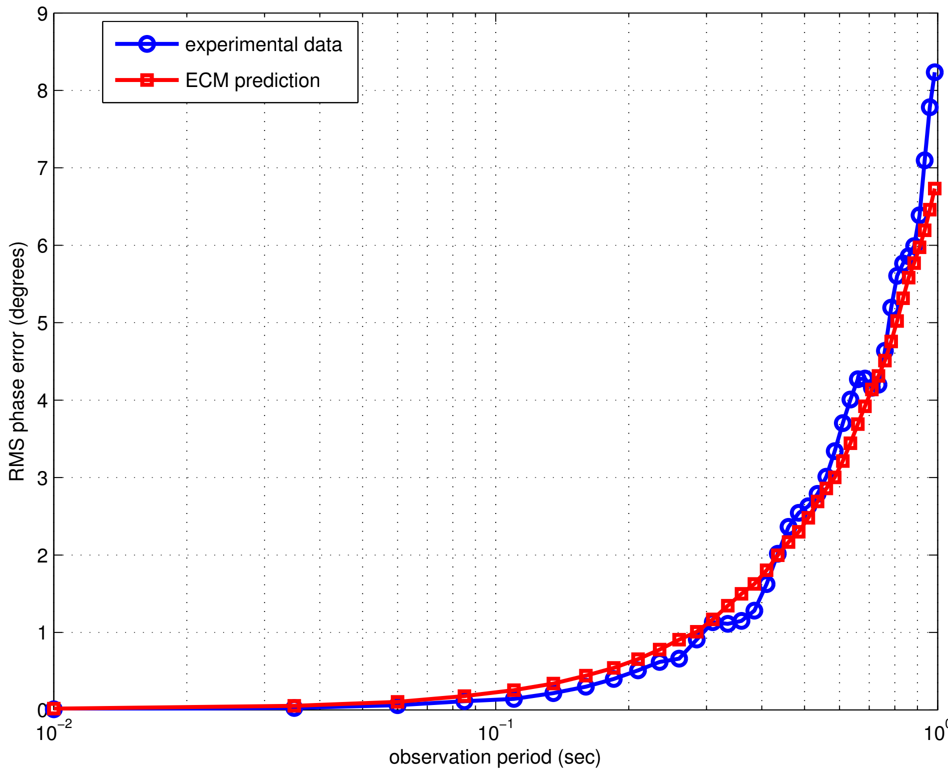

Figure 2.7: RMS phase error: experimental data and ECM predictions versus observation period T_0 at 15 MHz.

To better understand the meaning of these results in the context of distributed transmission systems, we show the performance of a hypothetical distributed transmission system with $N_t = 10$ transmitters and $N_r = 1$ receiver. In [43], theoretical beamforming and nullforming power gains are derived and shown to only depend on the phase variance.

Fig. 2.8 shows the expected beamforming power of the system given the phase error of the empirically estimated phase offset predictions. The figure shows a loss of less than 1 dB in beamforming power when $T_0 = 2$ seconds. In Fig. 2.9, it is shown that the nullforming power has a steeper drop as expected from the theoretical steady-state results. In practice, observation periods on the order of of milliseconds are feasible, leading to very good performance at a carrier frequency of 15 MHz, but also leading to increased feedback overhead.

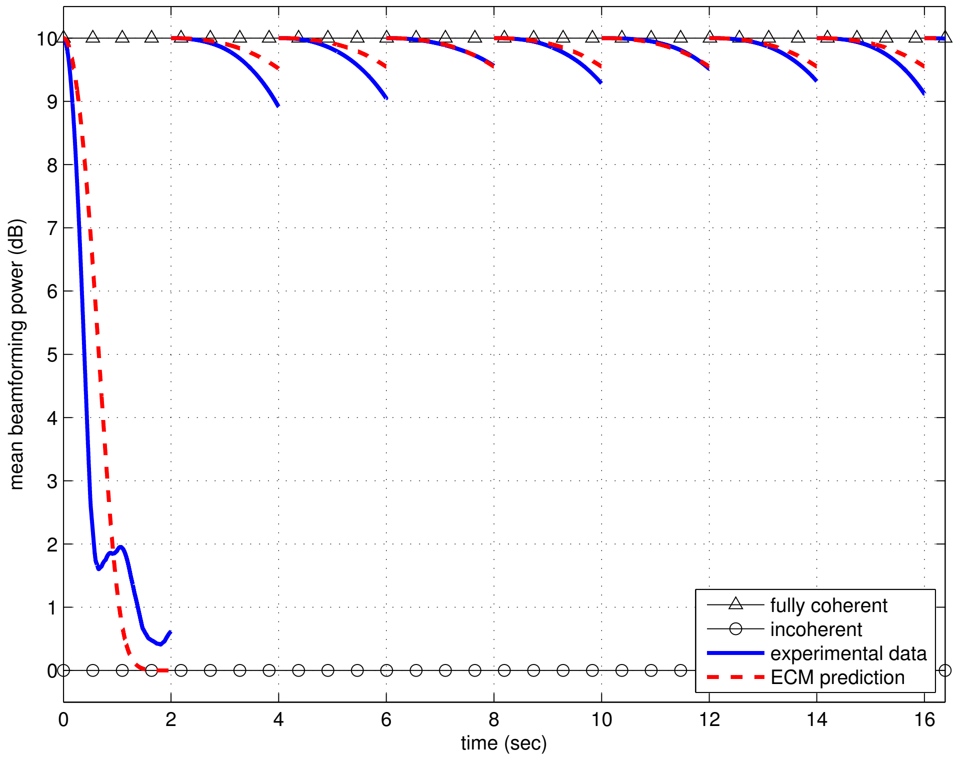

Figure 2.8: Expected beamforming power at 15 MHz with observation period $T_0 = 2$ seconds.

900 MHz Phase Tracking and Prediction Experiments

In this section, we provide experimental tracking results for phase tracking between two USRP N210s at a 900 MHz carrier frequency. The increase in carrier frequency from 15 MHz to 900 MHz leads to a much larger process noise covariance matrix and, consequently, requires a smaller observation period T_0 to provide satisfactory performance. The Kalman filter phase tracking and prediction performance assuming an observation period of $T_0 = 50$ ms is shown in Fig. 2.10 below. The corresponding beamforming and nullforming expected power is shown in Figs. 2.11 and 2.12.

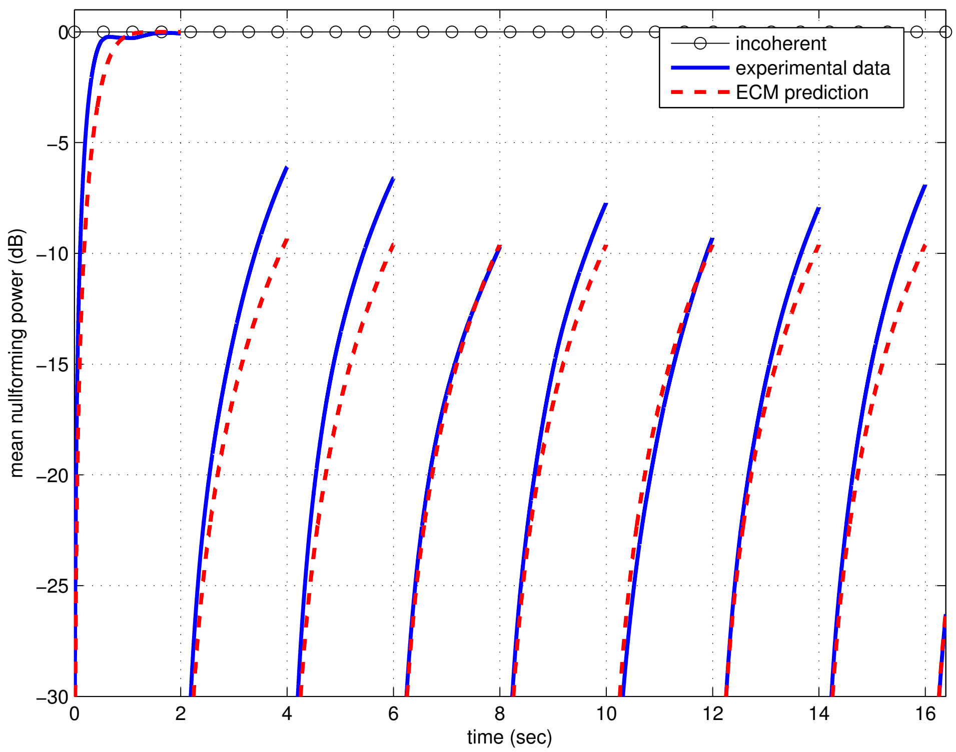

Figure 2.9: Expected nullforming power at 15 MHz with observation period $T_0 = 2$ seconds.

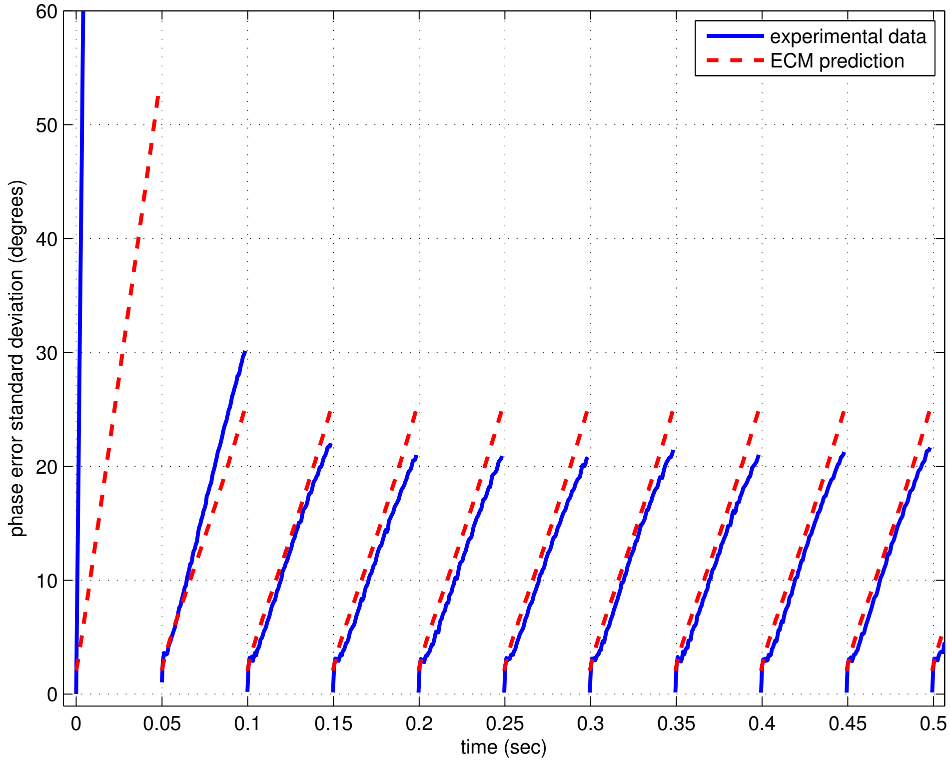

Figure 2.10: Kalman filter RMS phase error at 900 MHz with observation period $T_0 = 50$ ms.

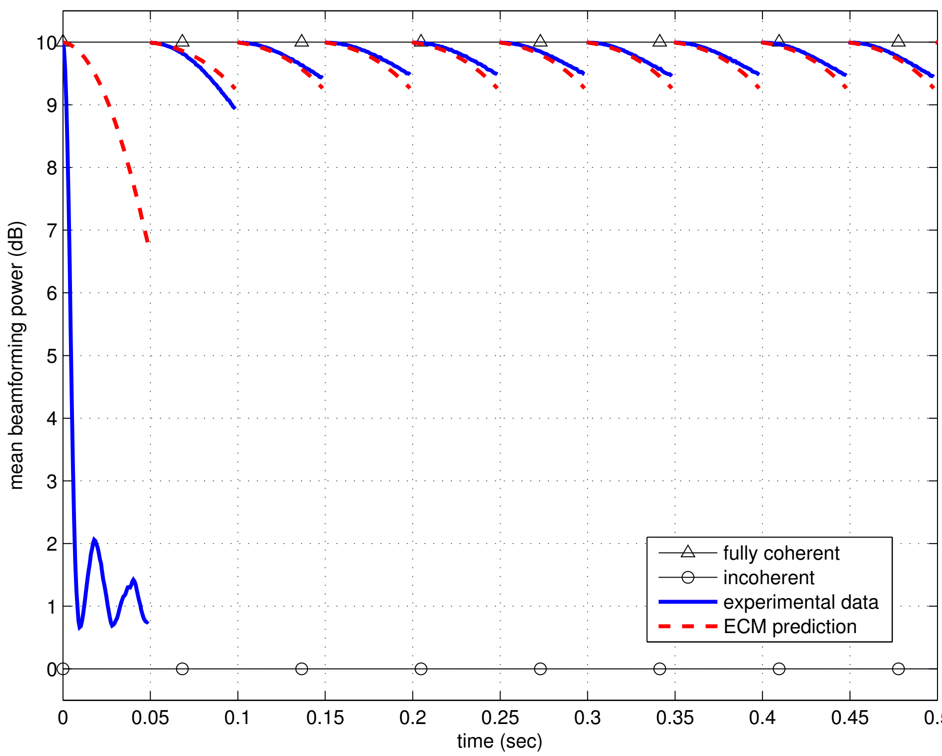

Figure 2.11: Expected beamforming power at 900MHz with observation period $T_0 = 50$ ms.

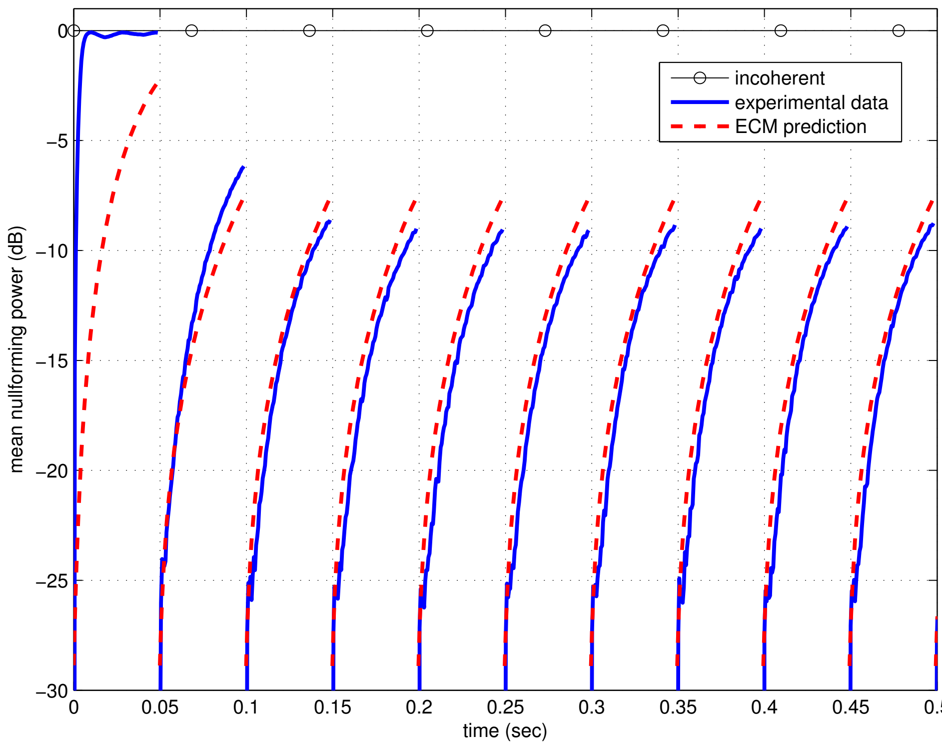

Figure 2.12: Expected nullforming power at 900MHz with observation period $T_0 = 50$ ms.

Mehra Method and Allan Deviation Comparisons

Using the 15 MHz carrier frequency data, we implement the Mehra method to compare the tracking performance with the previous Allan Deviation results. We first look at the parameter estimation results of the two methods. Table 2.2 shows the results of one experiment computed both using the Mehra method and the Allan deviation method. It can be seen that the results are similar, with the biggest variation in the q_2 long term stability parameter. This makes sense since the long stability parameter poses the highest difficulty in estimating.

Parameter	units	Mehra	Allan Deviation
r	rad^2	8.95×10^{-9}	1.74×10^{-8}
q_1	sec	4.18×10^{-21}	1.17×10^{-22}
q_2	Hz	8.08×10^{-16}	7.06×10^{-18}

Table 2.2: USRP VCXO parameter comparison between the Mehra method and Allan deviation method.

Fig. 2.13 shows the correlation of the innovation process when running a Kalman filter with each parameter. It can be seen that the Allan deviation parameters give both a smaller zero-lag value and a whiter sequence, compared to the Mehra method.

Finally, in Fig. 2.14 the average Kalman filter tracking performance of the two methods is shown. It is interesting to observe that, while the Allan deviation parameters make the phase reach steady state quicker, when reaching steady state, the Kalman filter behaves similarly. This shows an intrinsic resilience of the Kalman filter.

2.4.2 OCXO Experiments

The same analysis discussed in the previous sections was further applied to additional experimental data obtain with a more stable Rakon oven controlled oscillator(OCXO) [67].

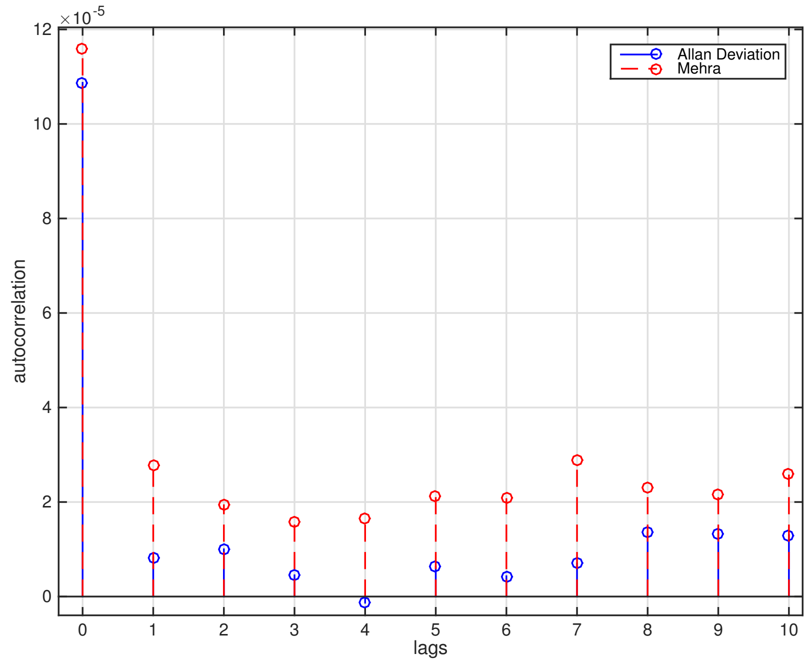

Figure 2.13: Innovation process correlation comparison

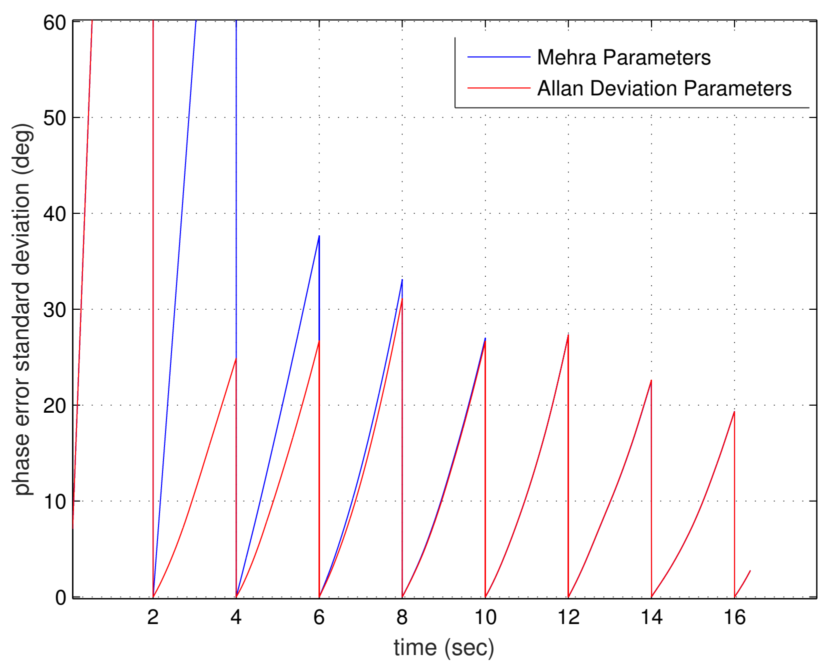

Figure 2.14: Kalman filter phase error comparison: Mehra vs. Allan deviation.

Over-the-Wire Experiments

An initial experiment was done in an almost exact fashion with the experiments described in Section 2.3. For these experiments, a carrier frequency of 8 GHz was used, since the equipment allowed for higher frequencies than the USRP radios. The data was sampled at 100 MHz and downsampled by a factor of 1000 before processing. Around 10 minutes of data were recorded in the experiment.

Fig. 2.15 shows the Allan deviation results for this case. The values for the stability and measurement noise parameters were found to be: $q_1 = 2.7855 \times 10^{-23}$; $q_2 = 3.6436 \times 10^{-25}$; $r = 5.0716 \times 10^{-4}$. It should be noted the Mehra method was not applied to this wire experiment. To evaluate the tracking performance on this data, the parameters were used in the Kalman filter and the data was split into blocks of 4 seconds and averaged.

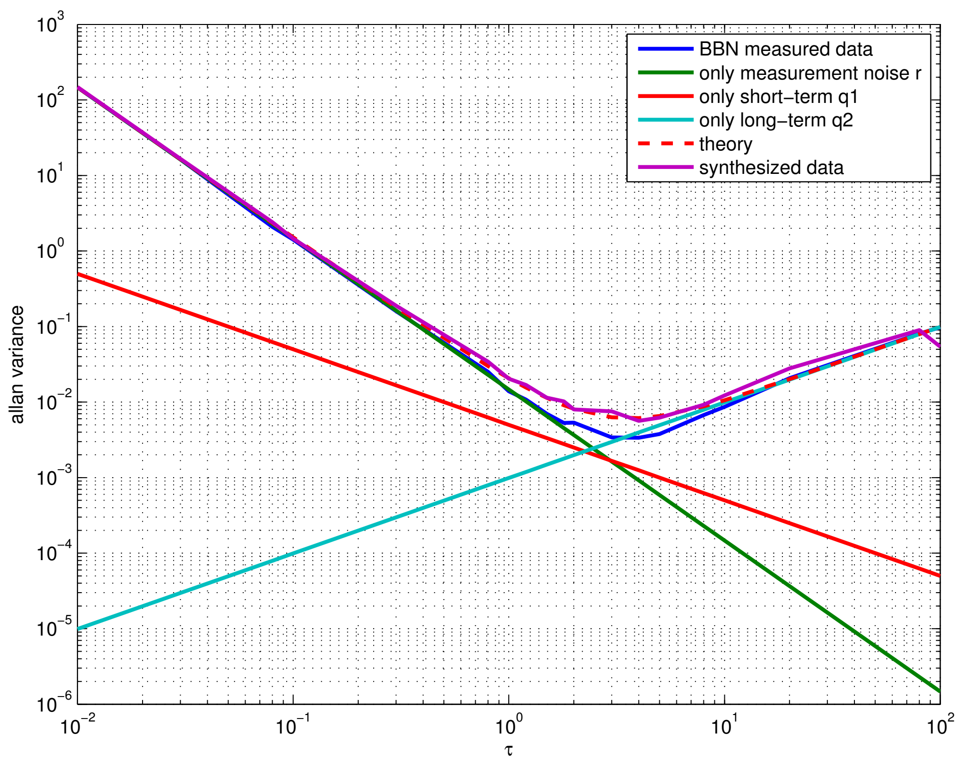

Figure 2.15: Allan variance plot with corresponding parameter fitting lines and theoretical curve.

Fig. 2.16 shows the comparison between the phase error of real data and the theoretical expected results. To make sure that the system works correctly, 2-state model data with the same parameters was synthesized and plugged into the Kalman filter. We can see that the real data is doing slightly worse than ideal given the noise, but the results are withing a couple of degrees.

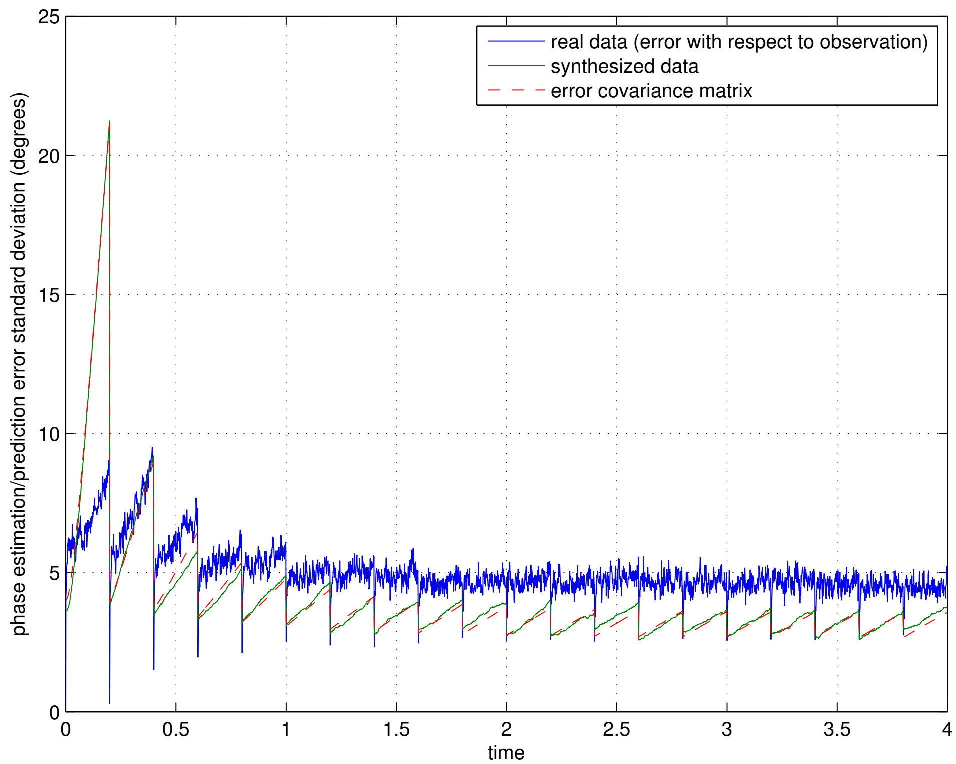

Figure 2.16: Kalman filter performance compared to theoretical expectaions.

Over-the-Air Experiments

The final and most interesting results obtained with these methods were done using wireless transmission over a 1 kilometer link. This experiment was used as a tuning stage for a beamforming experiment and our contribution was to extract the stability parameters. The experiment was done at 2.625 GHz in this case and additional preprocessing was performed to obtain phase estimates at a rate of 50 Hz. In addition, data from two transmitters was obtained in parallel. Fig. 2.17 shows the unwrapped and detrended phases obtained from the two transmitters. It might look curious that the two phases have such a similar shape, but this can be easily explained. Since the same receive antenna is used for both transmitter, the bulk of the frequency drift is due to the receive chain, while the smaller and more random drifts show that the two channels are indeed different.

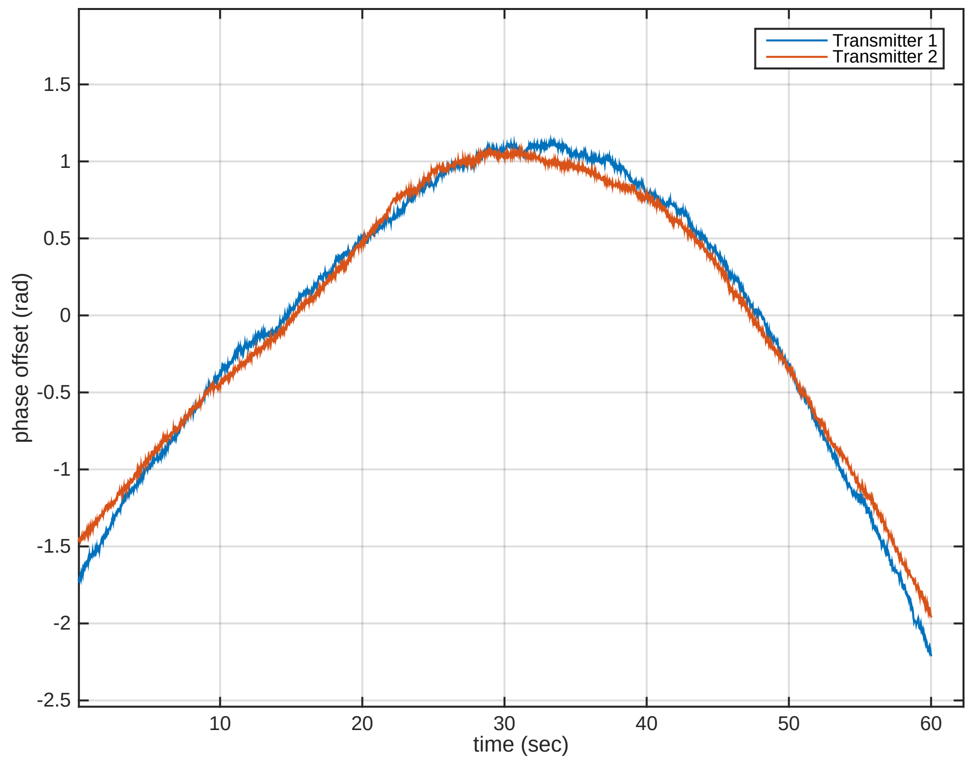

Figure 2.17: Phase offset of two transmitters.

For these data sets, both Mehra and Allan deviation methods were used to extract the parameters.

Tables 2.3 and 2.4 show the results of the two transmitters. In this case the q_1 parameter has a bigger variation between the two methods, but it is important to note that these values are much smaller than the values in Table 2.2 due to the higher stability of the local oscillators.

The corresponding Kalman filter phase error plots are shown in Figs. 2.18 and 2.19.

Parameter	units	Mehra	Allan Deviation
r	rad^2	4.29×10^{-5}	3.18×10^{-4}
q_1	sec	6.09×10^{-24}	2.37×10^{-22}
q_2	Hz	1.03×10^{-24}	9.59×10^{-24}

Table 2.3: Transmitter 1: OCXO measurement noise, short-term and long-term stability parameters obtained using Mehra and Allan deviation methods.

Parameter	units	Mehra	Allan Deviation
r	rad^2	6.15×10^{-5}	8.31×10^{-5}
q_1	sec	2.05×10^{-24}	3.64×10^{-23}
q_2	Hz	1.03×10^{-24}	5.56×10^{-24}

Table 2.4: Transmitter 1: OCXO measurement noise, short-term and long-term stability parameters obtained using Mehra and Allan deviation methods.

One important aspect here is the 2-seconds update period used which leads to a less than 5 degrees phase error for the 2.625 GHz transmission.

2.5 Conclusions

In this chapter we showed a method for extracting measurement and process noise parameters to facilitate oscillator tracking in a Kalman filtering framework. We tested our method on experimental data obtained from phase offset measurements between two USRP N210 devices. By closely matching the Kalman Filter parameters to the experimental data, we show that we can achieve very good tracking performance. Our results show that parameter estimation is not straightforward since the Allan deviation results are influenced by measurement noise. Nevertheless, the results show that the phase error of the Kalman filter output translates into very good beamforming and nullforming performance, even for practical observation periods. Moreover, the experimental results agree closely with the Kalman filter error covariance matrices.

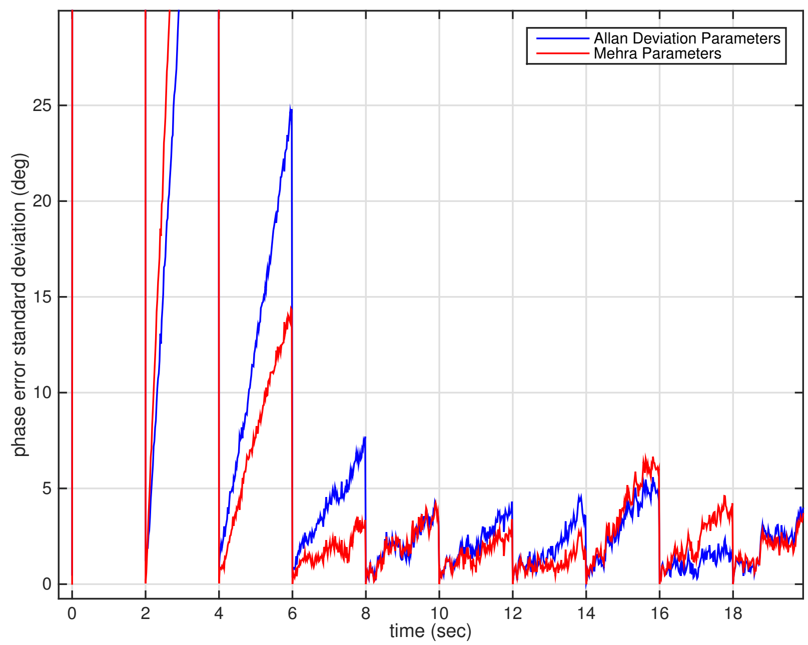

Figure 2.18: Kalman filter performance comparison for Transmitter 1 OTA experiment.

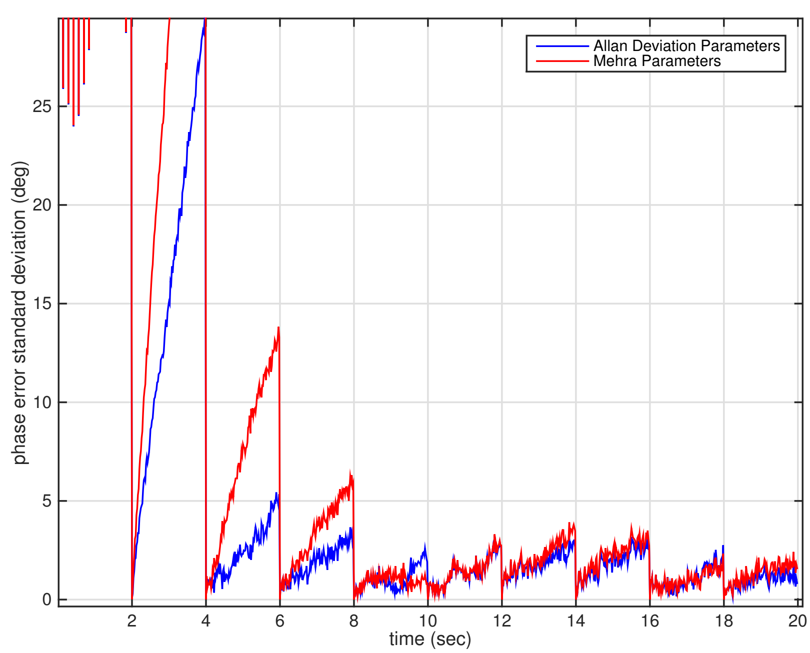

Figure 2.19: Kalman filter performance for transmitter 2 OTA experiment.

Chapter 3

Local and Unified Tracking

This chapter addresses the problem of channel tracking in large distributed systems. We look at systems that have a large number of independent transmit and receive nodes and we identify two methods of tracking the channels: local and unified.

3.1 Introduction

We consider the scenario in Fig. 3.1 where a distributed transmission cluster with N_t transmitters cooperate to form a virtual antenna array. The goal is to simultaneously steer a beam toward one intended receiver while also steering nulls toward $N_r - 1$ protected receivers. The receivers coordinate the transmissions by estimating the forward link channels and providing feedback to the transmit cluster to facilitate the calculation of appropriate linear precoding vectors.

The idea of distributed transmit beamforming has been well-studied in the last decade, e.g., [12, 14–17], but the idea of distributed transmit nullforming has only recently been considered [32, 35, 37]. In particular, in [37], the approach was for each receiver to track a time-varying state of "effective" channel phase and frequency offsets which included the

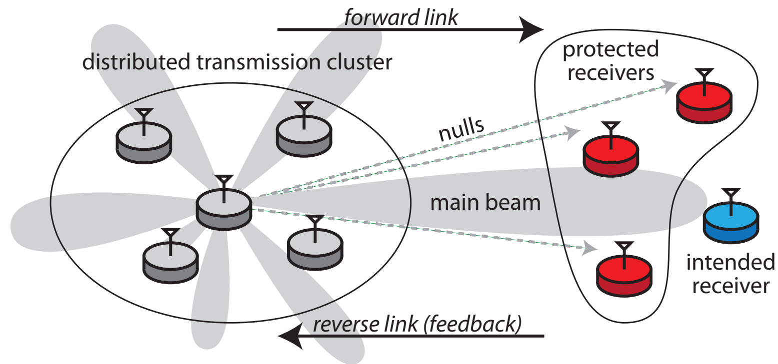

Figure 3.1: Distributed transmission scenario.

effect of stochastic clock drifts. Explicit state feedback from the N_r receivers was then used by the transmit cluster to predict the $N_t \times N_r$ channel matrix and compute a zero-forcing precoding vector for distributed transmission. A simplifying assumption in [37] was that each receiver *individually tracked* its N_t effective channel phase and frequency offsets. This approach is suboptimal since it does not exploit the statistical coupling of the pairwise phase and frequency offsets across all of the receive nodes.

In this chapter, we study the performance of a distributed nullforming system with optimal, i.e., "unified", phase and frequency tracking at the receivers to determine the potential gains with respect to suboptimal local tracking. In practice, unified tracking could be achieved by having the receive nodes forward their observations to a master receive node and having this master receive node apply the overall observation vector to a unified Kalman filter. Alternatively, the receive nodes could provide their observations to the transmit cluster via the feedback link and one or more transmit nodes could implement a unified Kalman filter. In either case, rather than using N_r separate small Kalman filters to track the effective channel phase and frequency offsets as in [37], a system with unified tracking uses one large Kalman filter and achieves optimal performance by exploiting the correlations in the offset states across receive nodes.

This chapter develops a model for unified tracking and compares the performance of this approach with respect to local tracking. Our results show that, while beamforming performance is effectively unchanged, nullforming performance can be significantly improved with unified tracking. In particular, unified tracking tends to provide the largest nullforming gains over short prediction intervals and for larger networks, e.g., distributed implementations of massive MIMO [10, 68]. The results also show that local tracking tends to provide near-optimal performance in systems with high feedback latency. We provide numerical results that confirm the analysis and compare the performance of local and unified tracking with varying prediction intervals and network sizes.

3.2 System Model

Each node in the system shown in Fig. 3.1 is assumed to possess a single antenna. The nominal transmit frequency in the forward link from the distributed transmit cluster to the receivers is at ω_c. All forward link channels are modeled as narrowband, linear, and time invariant (LTI). Enumerating the transmitters as $n = 1, \dots, N_t$ the receivers as $m = 1, \dots, N_r$ and adopting the convention that the intended receiver is node 1, we denote the channel from transmit node n to receive node m at carrier frequency ω_c as $g^{(n,m)} \in \mathbb{C}$ for $n = 1, \dots, N_t$ and $m = 1, \dots, N_r$.

As in [37], all of the receivers in the system measure and track the channels from the transmit cluster and to provide feedback to the transmit cluster to facilitate distributed transmission. Fig. 3.2 shows the *effective* narrowband channel model from transmit node n to receive node m which includes the effects of propagation and carrier offset. Transmissions $n \to m$ are conveyed on a carrier nominally at ω_c generated at transmit node n, incur a phase shift of $\psi^{(n,m)} = \angle g^{(n,m)}$ over the wireless channel, and are then downmixed by receive node m using its local carrier nominally at ω_c. At time t, the effective narrowband channel from transmit node n to receive node m is modeled as

$$h^{(n,m)}(\tau) = g^{(n,m)} e^{j\left(\phi_t^{(n)}(\tau) - \phi_r^{(m)}(\tau)\right)} = |g^{(n,m)}| e^{j\phi^{(n,m)}(\tau)} \tag{3.1}$$

where $\phi_t^{(n)}(\tau)$ and $\phi_r^{(m)}(\tau)$ are the local carrier phase offsets at transmit node n and receive node m, respectively, at time τ with respect to an ideal carrier reference, and $\phi^{(n,m)}(\tau) = \phi_t^{(n)}(\tau) - \phi_t^{(m)}(\tau) + \psi^{(n,m)}$ is the pairwise phase offset after propagation between transmit node n and receive node m at time τ.

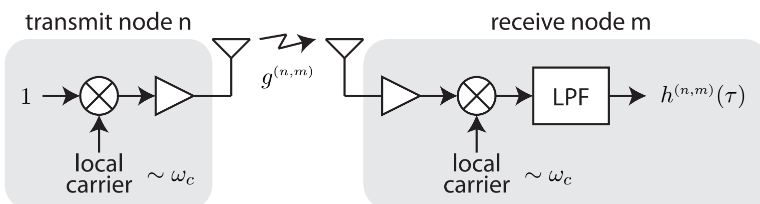

Figure 3.2: Effective narrowband channel model including the effects of propagation, transmit and receive gains, and carrier offset.

3.2.1 Oscillator Dynamics

Each transmit and receive node in the system is assumed to have an independent local oscillator. These local oscillators have inherent frequency offsets and behave stochastically, causing phase offset variations in each effective channel from transmit node n to receive node m even when the propagation channels $g^{(n,m)}$ are otherwise time invariant. This section describes a discrete-time dynamic model to characterize the dynamics of the phase variations in $h^{(n,m)}(\tau)$.

Based on the two-state models in [53, 54], we define the discrete-time state of the n^{th} transmit node's carrier as $\boldsymbol{x}_t^{(n)}[k] = [\phi_t^{(n)}[k], \omega_t^{(n)}[k]]^\top$ where $\phi_t^{(n)}[k]$ corresponds to the carrier phase offset in radians at transmit node n with respect to an ideal carrier phase reference. The state update of the n^{th} transmit node's carrier is then

$$\boldsymbol{x}_t^{(n)}[k+1] = \boldsymbol{f}(T)\boldsymbol{x}_t^{(n)}[k] + \boldsymbol{u}_t^{(n)}[k] \text{ with } \boldsymbol{f}(T) = \begin{bmatrix} 1 & T \\ 0 & 1 \end{bmatrix} \tag{3.2}$$

where T is an arbitrary sampling period selected to be small enough to avoid phase aliasing at the largest expected frequency offsets. The process noise vector $\boldsymbol{u}_t^{(n)}[k] \overset{\text{i.i.d.}}{\sim} \mathcal{N}\left(\boldsymbol{0}, \boldsymbol{Q}_t^{(n)}(T)\right)$ causes the carrier derived from the local oscillator at transmit node n to deviate from an ideal linear phase trajectory. The covariance of the discrete-time process noise is derived from a continuous-time model in [53] and is

$$\boldsymbol{Q}_t^{(n)}(T) = \omega_c^2 T \begin{bmatrix} p_t^{(n)} + q_t^{(n)}\frac{T^2}{3} & q_t^{(n)}\frac{T}{2} \\ q_t^{(n)}\frac{T}{2} & q_t^{(n)} \end{bmatrix} \tag{3.3}$$

where ω_c is the nominal common carrier frequency in radians per second and $p_t^{(n)}$ (units of seconds) and $q_t^{(n)}$ (units of Hertz) are the process noise parameters corresponding to white frequency noise and random walk frequency noise, respectively. We make the general change of notation $p = q_1$ and $q = q_2$ to differentiate between different transmitters and receivers.

The receive nodes in the system also have independent local oscillators used to generate carriers for downmixing that are governed by the same dynamics as (3.2) with state $\boldsymbol{x}_r^{(m)}[k]$, process noise $\boldsymbol{u}_r^{(m)}[k] \overset{\text{i.i.d.}}{\sim} \mathcal{N}(0, \boldsymbol{Q}_r^{(m)}(T))$, and process noise parameters $p_r^{(m)}$ and $q_r^{(m)}$ as in (3.3) for $m = 1, \ldots, N_r$.

Since receive nodes can only measure the relative phase and frequency of the transmit nodes after propagation, we define the *pairwise offset* after propagation as

$$\boldsymbol{\delta}^{(n,m)}[k] = \begin{bmatrix} \phi^{(n,m)}[k] \\ \dot{\phi}^{(n,m)}[k] \end{bmatrix} = \boldsymbol{x}_t^{(n)}[k] + \begin{bmatrix} \psi^{(n,m)} \\ 0 \end{bmatrix} - \boldsymbol{x}_r^{(m)}[k].$$

Note that $\boldsymbol{\delta}^{(n,m)}[k]$ is governed by the state update

$$\boldsymbol{\delta}^{(n,m)}[k+1] = \boldsymbol{f}(T)\boldsymbol{\delta}^{(n,m)}[k] + \boldsymbol{u}_t^{(n)}[k] - \boldsymbol{u}_r^{(m)}[k]. \tag{3.4}$$

We assume that observations are so short as to only provide useful phase estimates. An observation of the $n \to m$ channel is then

$$y^{(n,m)}[k] = \boldsymbol{h}\delta^{(n,m)}[k] + v^{(n,m)}[k]$$

where $\boldsymbol{h} = [1, 0]$ and $v^{(n,m)}[k] \overset{\text{i.i.d.}}{\sim} \mathcal{N}(0, R)$ is the measurement noise which is assumed to be spatially and temporally i.i.d.

3.2.2 Local Tracking Model

In the case of local tracking, each receiver uses only its local observations to track the pairwise offset states with respect to the receiver's local oscillator. At receiver m, the $2N_t$-dimensional vector state of pairwise offsets is defined as $\boldsymbol{\delta}^{(m)}[k] = [(\boldsymbol{\delta}^{(1,m)}[k])^\top, \ldots, (\boldsymbol{\delta}^{(N_t,m)}[k])^\top]^\top$ and has the state update

$$\begin{aligned} \boldsymbol{\delta}^{(m)}[k+1] &= \begin{bmatrix} \boldsymbol{f}(T) & & \\ & \ddots & \\ & & \boldsymbol{f}(T) \end{bmatrix} \boldsymbol{\delta}^{(m)}[k] + \begin{bmatrix} \boldsymbol{u}_t^{(1)}[k] - \boldsymbol{u}_r^{(m)}[k] \\ \vdots \\ \boldsymbol{u}_t^{(N_t)}[k] - \boldsymbol{u}_r^{(m)}[k] \end{bmatrix} \\ &= \boldsymbol{F}_{\text{loc}}(T)\boldsymbol{\delta}^{(m)}[k] + \boldsymbol{G}_{\text{loc}}\boldsymbol{u}^{(m)}[k]. \end{aligned} \tag{3.5}$$

where

$$\boldsymbol{G}_{\mathrm{loc}} = \begin{bmatrix} \boldsymbol{I}_2 & & & -\boldsymbol{I}_2 \\ & \ddots & & \vdots \\ & & \boldsymbol{I}_2 & -\boldsymbol{I}_2 \end{bmatrix} \text{ and } \boldsymbol{u}^{(m)}[k] = \begin{bmatrix} \boldsymbol{u}_t^{(1)}[k] \\ \vdots \\ \boldsymbol{u}_t^{(N_t)}[k] \\ \boldsymbol{u}_r^{(m)}[k] \end{bmatrix} \tag{3.6}$$

and where $\boldsymbol{I}_2$ is the 2×2 identity matrix. We assume

$$\begin{aligned} \operatorname{cov}\{\boldsymbol{u}^{(m)}[k]\} &= \mathsf{blockdiag}\left\{\boldsymbol{Q}_t^{(1)}(T), \ldots, \boldsymbol{Q}_t^{(N_t)}(T), \boldsymbol{Q}_r^{(m)}(T)\right\} \\ &= \boldsymbol{Q}^{(m)}(T) \end{aligned}$$

hence $\boldsymbol{G}_{\mathrm{loc}}\boldsymbol{u}^{(m)}[k] \sim \mathcal{N}\left(\boldsymbol{0}, \boldsymbol{G}_{\mathrm{loc}}\boldsymbol{Q}^{(m)}(T)\boldsymbol{G}_{\mathrm{loc}}^{\top}\right)$. The vector observation for the local Kalman filter is then $\boldsymbol{y}^{(m)}[k] = [y^{(1,m)}[k], \ldots, y^{(N_t,m)}[k]]^{\top}$ and related to the local state as

$$\boldsymbol{y}^{(m)}[k] = \boldsymbol{h}_{\mathrm{loc}}\boldsymbol{\delta}^{(m)}[k] + \boldsymbol{v}^{(m)}[k]$$

where $\boldsymbol{h}_{\mathrm{loc}} = \mathsf{blockdiag}(\boldsymbol{h}, \ldots, \boldsymbol{h}) \in \mathbb{R}^{N_t \times 2N_t}$ and $\boldsymbol{v}^{(m)}[k] = [v^{(1,m)}[k], \ldots, v^{(N_t,m)}[k]]^{\top} \in \mathbb{R}^{N_t}$ is the measurement noise.

3.2.3 Unified Tracking Model

In the case of unified tracking, there is a master receiver or transmitter that aggregates all of the observations and tracks all of the pairwise offset states in the system. The $2N_tN_r$-dimensional vector state of pairwise offsets is defined as $\boldsymbol{\delta}[k] = [(\boldsymbol{\delta}^{(1)}[k])^{\top}, \ldots, (\boldsymbol{\delta}^{(N_r)}[k])^{\top}]^{\top}$

and has the state update

$$\begin{aligned}
\boldsymbol{\delta}[k+1] &= \begin{bmatrix} \boldsymbol{f}(T) & & \\ & \ddots & \\ & & \boldsymbol{f}(T) \end{bmatrix} \boldsymbol{\delta}[k] + \begin{bmatrix} \boldsymbol{u}_t^{(1)}[k] - \boldsymbol{u}_r^{(1)}[k] \\ \vdots \\ \boldsymbol{u}_t^{(N_t)}[k] - \boldsymbol{u}_r^{(N_r)}[k] \end{bmatrix} \\
&= \boldsymbol{F}_{\text{uni}}(T)\boldsymbol{\delta}[k] + \boldsymbol{G}_{\text{uni}}\boldsymbol{u}[k] \qquad (3.7)
\end{aligned}$$

where the process noise vector $\boldsymbol{u}[k] = [(\boldsymbol{u}_t^{(1)}[k])^\top, \ldots, (\boldsymbol{u}_t^{(N_t)}[k])^\top, (\boldsymbol{u}_r^{(1)}[k])^\top, \ldots, (\boldsymbol{u}_r^{(N_r)}[k])^\top]^\top \in \mathbb{R}^{2(N_t+N_r)}$ and

$$\boldsymbol{G}_{\text{uni}} = \begin{bmatrix} \boldsymbol{I}_{2N_t} & \boldsymbol{J}_{2N_t} & & \\ \vdots & & \ddots & \\ \boldsymbol{I}_{2N_t} & & & \boldsymbol{J}_{2N_t} \end{bmatrix} \in \mathbb{R}^{2N_tN_r \times 2(N_t+N_r)} \qquad (3.8)$$

with $\boldsymbol{J}_{2N_t} = -[\boldsymbol{I}_2, \ldots, \boldsymbol{I}_2]^\top \in \mathbb{R}^{2N_t \times 2}$. The N_tN_r-dimensional vector observation for the unified Kalman filter is then

$$\boldsymbol{y}[k] = \boldsymbol{h}_{\text{uni}}\boldsymbol{\delta}[k] + \boldsymbol{v}[k]$$

where $\boldsymbol{h}_{\text{uni}} = \mathsf{blockdiag}(\boldsymbol{h}, \ldots, \boldsymbol{h}) \in \mathbb{R}^{N_tN_r \times 2N_tN_r}$ and $\boldsymbol{v}[k] = [v^{(1,1)}[k], \ldots, v^{(N_t,N_r)}[k]]^\top \in \mathbb{R}^{N_tN_r}$ is the measurement noise.

3.2.4 Discussion

Note that the state update equations (3.5) and (3.7) specify dynamic systems where the states are coupled only through the correlated process noise. In the local tracking model, the process noise is correlated only through receive node m's oscillator as shown in (3.6). In the unified tracking model, the process noise is correlated through *all* of the receive oscillators as shown in (3.8). While the number of states grows according to the product $N_t N_r$, the number of independent oscillators grows according to the sum $N_t + N_r$. Hence, since the unified tracker exploits all of the process noise correlations in the system, we can expect the unified tracker to provide the most significant performance gains with respect to local tracking in large networks.

3.3 Receiver-Coordinated Protocol

We assume the receiver-coordinated protocol described in [35, 37]. Forward link transmissions are divided into measurement and distributed transmission epochs, repeating periodically with period T_m. Reverse link transmissions provide feedback from the receive nodes to the transmit nodes to facilitate linear precoding vector calculation.

Given a measurement at time k and denoting the Kalman filter's MMSE phase prediction at time $\ell > k$ as $\hat{\phi}^{(n,m)}[\ell \,|\, k]$, we can write the effective channel prediction for $h^{(n,m)}(\tau)$ at time $\tau = \ell T$ as

$$\hat{h}^{(n,m)}[\ell \,|\, k] = |g^{(n,m)}| e^{j\hat{\phi}^{(n,m)}[\ell \,|\, k]} \tag{3.9}$$

since the channel amplitudes $|g^{(n,m)}|$ are assumed to be known. We denote the vector of channel predictions from all transmit nodes to receive node m as $\hat{\boldsymbol{h}}^{(m)}[\ell \,|\, k] \in \mathbb{C}^{N_t}$ and the protected receiver predicted channel matrix as $\hat{\boldsymbol{H}}[\ell|k] = \left[\hat{\boldsymbol{h}}^{(2)}[\ell|k], \ldots, \hat{\boldsymbol{h}}^{(N_r)}[\ell|k]\right] \in \mathbb{C}^{N_t \times N_r}$ for $\ell > k$.

The MMSE channel predictions are used to calculate the precoding vector $\boldsymbol{w}[\ell] \in \mathbb{C}^{N_t}$ for all ℓ in the distributed transmission epoch. Under our assumption that the number of protected receivers is less than N_t, we can select the transmit vector $\boldsymbol{w}[\ell] \in \mathbb{C}^{N_t}$ to be orthogonal to $\hat{\boldsymbol{h}}^{(m)}[\ell \,|\, k]$ for all $m = 2, \ldots, N_r$ and then use the remaining degrees of freedom in the transmit vector to maximize the received power at the intended receiver.

Defining $\hat{\boldsymbol{D}}[\ell|k] = \boldsymbol{I} - \hat{\boldsymbol{H}}[\ell|k]\left(\hat{\boldsymbol{H}}^{H}[\ell|k]\hat{\boldsymbol{H}}[\ell|k]\right)^{-1}\hat{\boldsymbol{H}}^{H}[\ell|k]$, the zero-forcing transmit vector can then be computed as

$$\boldsymbol{w}[\ell] = \alpha[\ell]\hat{\boldsymbol{D}}[\ell|k]\hat{\boldsymbol{h}}^{(1)}[\ell|k] \tag{3.10}$$

where $\alpha[\ell]$ is selected to satisfy a per-node or total power constraint.

3.4 Performance Analysis

This section analyzes the steady-state performance of local and unified tracking. Our analysis assumes unit channel magnitudes such that $|g^{(n,m)}| = 1$, i.i.d. measurement noise with $\boldsymbol{v}[k] \sim \mathcal{N}(0, \boldsymbol{R})$ and $\boldsymbol{R} = \sigma_v^2\boldsymbol{I}$, and identical process noise statistics at each node.

To compute the steady-state prediction covariance of the Kalman filter with measurement period T_m, it can be straightforwardly verified that both the local and unified tracking systems satisfy the controllability and observability conditions so that the steady-state prediction covariance is a unique positive definite matrix specified as the solution to the discrete-time algebraic Riccati equation [69]. Denoting the prediction covariance as $\boldsymbol{P}$ (corresponding to either local or unified tracking), the steady-state estimation covariance (immediately after an observation) is then $\boldsymbol{S} = \boldsymbol{P} - \boldsymbol{P}\boldsymbol{h}^\top(\boldsymbol{h}\boldsymbol{P}\boldsymbol{h}^\top + \boldsymbol{R})^{-1}\boldsymbol{h}\boldsymbol{P}$. The prediction covariance at a prediction time t_p after the most recent measurement (during a distributed transmission epoch) is then $\boldsymbol{P}(t_p) = \boldsymbol{F}(t_p)\boldsymbol{S}\boldsymbol{F}^\top(t_p) + \boldsymbol{Q}(t_p)$. The (1,1) element of $\boldsymbol{P}(t_p)$ is the variance of the phase prediction, which we denote as $\sigma_\phi^2(t_p)$. The (1,3) element of $\boldsymbol{P}(t_p)$ is the covariance of the phase predictions between two transmitters as observed at one receiver, which we denote as $\rho^2\sigma_\phi^2(t_p)$.

To quantify the performance of distributed *beamforming* in terms of the prediction covariance, suppose that the signal received from the i^{th} transmitter at the intended receiver is given by $r_i = \alpha e^{j(\phi+\tilde{\phi}_i)}$ where $\alpha^2 = N_t^{-1}$ is the individual transmit power selected to satisfy a unit total power constraint, ϕ is the nominal beamforming phase, and $\tilde{\phi}_i$ is the phase error at transmitter i. The mean beamforming power is then

$$J = \mathrm{E}\left\{\left|\sum_{i=1}^{N_t} r_i\right|^2\right\} = \frac{1}{N_t}\sum_{i=1}^{N_t}\mathrm{E}\left\{c_i^2 + s_i^2\right\} + \frac{1}{N_t}\sum_{i=1}^{N_t}\sum_{j\neq i}\mathrm{E}\left\{c_i c_j + s_i s_j\right\}$$

where $c_i = \cos(\tilde{\phi}_i)$ and $s_i = \sin(\tilde{\phi}_i)$. Since $c_i^2 + s_i^2 = 1$ and $c_i c_j + s_i s_j = \cos(\tilde{\phi}_i - \tilde{\phi}_j)$, we have

$$J = 1 + \frac{1}{N_t}\sum_{i=1}^{N_t}\sum_{j\neq i}\mathrm{E}\left\{\cos\left(\tilde{\phi}_i - \tilde{\phi}_j\right)\right\}$$

Under our assumptions, $\tilde{\phi}_i$ are identically distributed (but not independent) zero-mean Gaussian random variables with variance is $\sigma_\phi^2(t_p)$ and covariance $\mathrm{E}\left\{\tilde{\phi}_i\tilde{\phi}_j\right\} = \rho^2\sigma_\phi^2(t_p)$ at prediction time t_p. It can then be shown via straightforward integration that $\mathrm{E}\left\{\cos\left(\tilde{\phi}_i - \tilde{\phi}_j\right)\right\} = e^{-(1-\rho^2)\sigma_\phi^2(t_p)}$, hence

$$J = N_t e^{-(1-\rho^2)\sigma_\phi^2(t_p)} + \left(1 - e^{-(1-\rho^2)\sigma_\phi^2(t_p)}\right). \tag{3.11}$$

Note that (4.33) is the mean beamforming power for a system with a single intended receiver and no nulls. If the system also steers nulls toward $N_r - 1$ receivers and the channel phases are random and independent, we can estimate the beamforming loss due to nulling as $1 - \frac{N_r - 1}{N_t}$ [37]. Hence, it follows that

$$J \approx \left[1 - \frac{N_r - 1}{N_t}\right] N_t e^{-(1-\rho^2)\sigma_\phi^2(t_p)} + 1 - e^{-(1-\rho^2)\sigma_\phi^2(t_p)}. \tag{3.12}$$

To quantify the performance of distributed *nullforming* at the protected receivers in terms of the prediction covariance, the signal from the i^{th} transmitter at a protected receiver is assumed to be given by $r_i = \alpha e^{j(\phi_i + \tilde{\phi}_i)}$ where ϕ_i is the nominal received phase from the i^{th} transmitter chosen so that $\sum_{i=1}^{N_t} e^{j\phi_i} = 0$, and $\tilde{\phi}_i$ is the phase error at transmitter i. The mean received power in a null is then

$$K = \mathrm{E}\left\{\left|\sum_{i=1}^{N_t} r_i\right|^2\right\} = \frac{1}{N_t}\sum_{i=1}^{N_t} \mathrm{E}\left\{p_i^2 + q_i^2\right\} + \frac{1}{N_t}\sum_{i=1}^{N_t}\sum_{j\neq i} \mathrm{E}\left\{p_i p_j + q_i q_j\right\}$$

where $p_i = \cos(\phi_i)\cos(\tilde{\phi}_i) - \sin(\phi_i)\sin(\tilde{\phi}_i)$ and $q_i = \cos(\phi_i)\sin(\tilde{\phi}_i) + \sin(\phi_i)\cos(\tilde{\phi}_i)$. Since $p_i^2 + q_i^2 = 1$ and $p_i p_j + q_i q_j = \cos(\phi_i - \phi_j)\cos(\tilde{\phi}_i - \tilde{\phi}_j) + \sin(\phi_i - \phi_j)\sin(\tilde{\phi}_i - \tilde{\phi}_j)$, we can write

$$\begin{aligned} K = 1 &+ \frac{1}{N_t}\sum_{i=1}^{N_t}\sum_{j\neq i} \cos(\phi_i - \phi_j)\mathrm{E}\left\{\cos(\tilde{\phi}_i - \tilde{\phi}_j)\right\} \\ &+ \frac{1}{N_t}\sum_{i=1}^{N_t}\sum_{j\neq i} \sin(\phi_i - \phi_j)\mathrm{E}\left\{\sin(\tilde{\phi}_i - \tilde{\phi}_j)\right\}. \end{aligned}$$

Straightforward integration yields $\mathrm{E}\left\{\cos(\tilde{\phi}_i - \tilde{\phi}_j)\right\} = e^{-(1-\rho^2)\sigma_\phi^2(t_p)}$ and $\mathrm{E}\left\{\sin(\tilde{\phi}_i - \tilde{\phi}_j)\right\} = 0$, hence

$$K = 1 + \frac{1}{N_t} e^{-(1-\rho^2)\sigma_\phi^2(t_p)} \sum_{i=1}^{N_t}\sum_{j\neq i} \cos(\phi_i - \phi_j)$$

It can be shown that, since ϕ_i satisfy $\sum_{i=1}^{N_t} e^{j\phi_i} = 0$, the sum $\sum_{i=1}^{N_t}\sum_{j\neq i}\cos(\phi_i - \phi_j) = -N_t$. Hence, the mean received power in a null is

$$K = 1 - e^{-(1-\rho^2)\sigma_\phi^2(t_p)}. \tag{3.13}$$

3.5 Numerical Results

This section presents numerical performance comparisons of distributed beamforming and nullforming with local and unified tracking. All of the results assume a forward link carrier frequency of 900 MHz and a measurement period of $T_m = 500$ ms. Based on the Allan variance specifications of the Rakon RFPO45 oscillator [67], the process noise parameters were set to $p_t^{(n)} = p_r^{(m)} = 2.31 \cdot 10^{-21}$ and $q_t^{(n)} = q_r^{(m)} = 6.80 \cdot 10^{-23}$ for all $n = 1, \ldots, N_t$ and all $m = 1, \ldots, N_r$. The standard deviation of the phase measurement error at the receive nodes was set to 10 degrees. All channels were assumed to have unit magnitude and the transmitter was assumed to have a unit total transmit power constraint.

Fig. 3.3 shows a full simulation of a "small" system with $N_t = 10$ transmitters and $N_r = 5$ receivers. Since the nullforming performance is identical at all of the protected receivers, the performance of only one null is shown here. The results were averaged over 3000 realizations of the random initial frequency offsets, clock process noises, and measurement noises. Measurements occur at $t = kT_m$ for $k = 0, 1, \ldots$. After the initial incoherent period where the Kalman filter has poor estimates with both local and unified tracking, the effect of the oscillator dynamics and periodic measurements can be seen in the beamforming and nullforming performance where the performance is relatively good immediately after a measurement but then degrades as the prediction time becomes longer. These results show that unified tracking provides a negligible advantage in beamforming gain but a potentially significant advantage in nullforming gain, especially as the Kalman filter converges to steady-state.

Figure 3.4 shows the steady-state performance of distributed beamforming and nullforming with local and unified tracking for the small system in Fig. 3.3 and a "massive MIMO" system with $N_t = 100$ transmitters and $N_r = 50$ receivers. These results were generated following the approach in Section 3.4. The small system results are consistent with Fig. 3.3. The massive MIMO system exhibits increased beamforming gain, as is expected, but also shows that beamforming performance is essentially the same with local or unified tracking. The nullforming performance of the massive MIMO system benefits more from unified tracking, especially over short prediction intervals. The nullforming

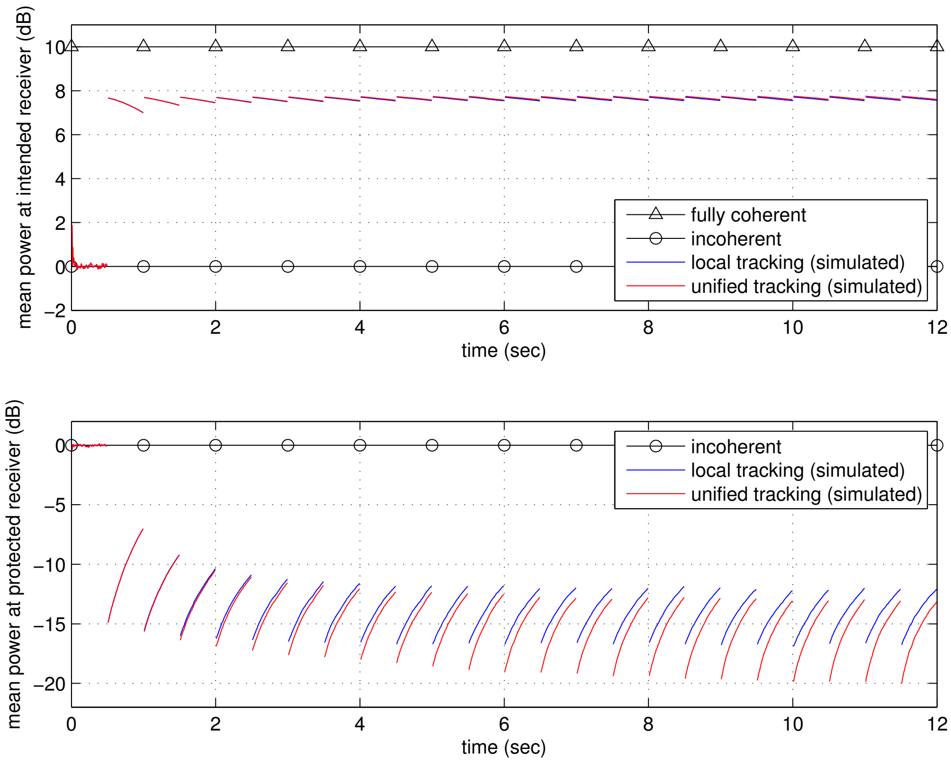

Figure 3.3: Full Kalman filter simulation of a “small” system.

performance of both systems becomes similar over longer prediction intervals.

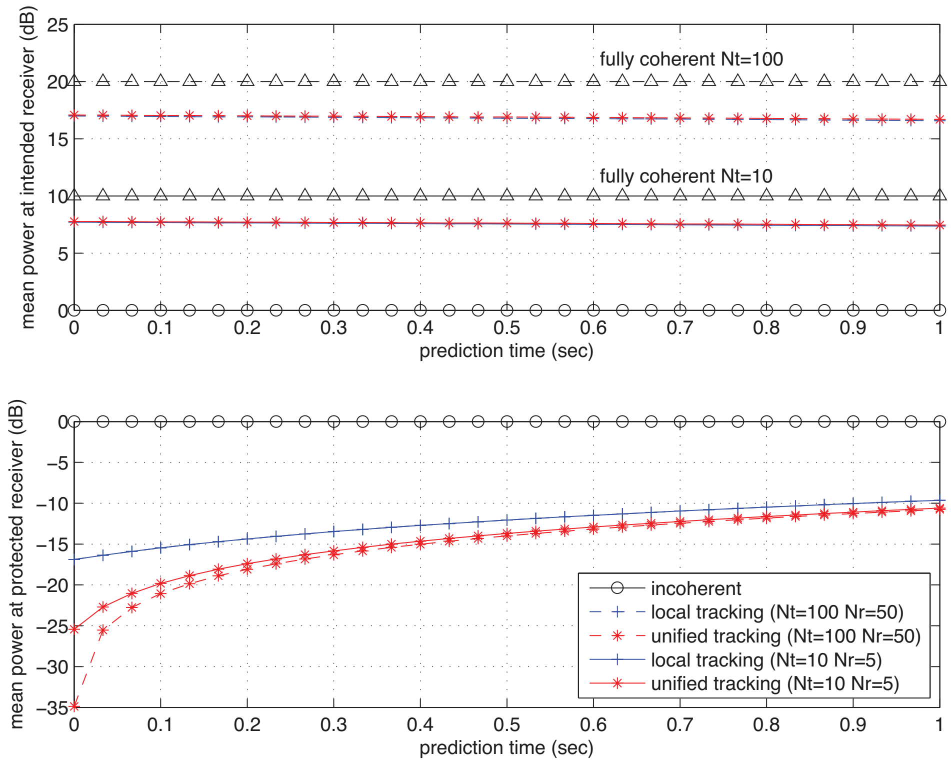

Figure 3.4: Steady-state beamforming and nullforming performance results with “small” and “massive MIMO” systems.

3.6 Conclusions

This chapter compares the performance of distributed transmission with local and unified tracking and shows that, while beamforming performance is effectively unchanged between local and unified tracking, nullforming performance can be significantly improved with unified tracking, especially over short prediction intervals and with larger networks. The results also show that local tracking tends to provide near-optimal performance in systems with high feedback latency. While unified tracking provides optimal performance, the additional complexity of unified tracking may cause local tracking to be more appealing in systems with high feedback latency.

Chapter 4

Accelerometer Compensation of Kinematic Effects

In this chapter we look at the impact of motion on oscillator stability. By considering a beamforming systems with many transmitters, we show that acceleration measurements can be integrated in the state space system to significantly decrease the estimation error.

4.1 Introduction

We consider the distributed multi-input single-output (MISO) communication scenario in Fig. 4.1 where a transmission cluster with N transmit nodes communicates with a single receive node. The transmit cluster transmits as a virtual antenna array and uses coherent transmission techniques, e.g., distributed transmit beamforming [12, 14–17] or distributed transmit nullforming [32, 35, 37]. We assume each node in the system has an independent local oscillator and that no exogenous synchronization signals are present. The receiver facilitates coherent transmission by estimating the combined time offsets and propagation delays and by providing periodic feedback to the transmit nodes.

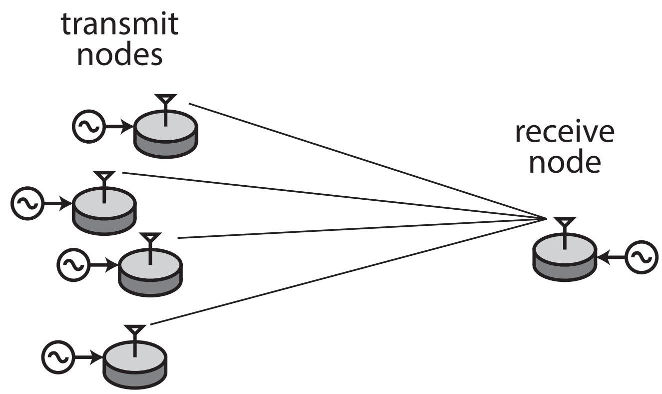

Figure 4.1: Distributed MISO system model with N transmit nodes and one receive node. Each node possesses a single antenna and an independent oscillator.

Since each node in the distributed transmission system has an independent local oscillator and may experience independent kinematic effects, the time offset and propagation delay between each transmit node and the receive node is time-varying and must be tracked and predicted to facilitate passband signal alignment and coherent transmission. Several recent papers have analyzed the performance of distributed beamforming and distributed nullforming subject to independent oscillator dynamics [17, 37, 43, 70]. Other than [17], this prior work has primarily focused on the case when the propagation channels are time-invariant or slowly-varying with respect to the oscillator dynamics. Although kinematic effects were studied in [17], the model did not account for the effect of acceleration on the frequency of crystal oscillators as described in [71]. All of this prior work assumed a conventional receiver-coordinated scenario in which the effective channels are tracked using only periodic feedback from the receive node.

The problem of inertial tracking using Kalman filters has been studied extensively [50, 72–74]. However, a heterogeneous system in which both motion and carrier information are being considered at the same time has not been considered previously in the literature.

This chapter analyzes the performance of coherent distributed transmission in a MISO system with independent clock dynamics and time-varying propagation channels. Each propagation channel is assumed to be single-path and its time variations are assumed to be caused by independent kinematics at each transmit node. The receive node is assumed to be stationary. Our analysis accounts for:

1. The effect of independent oscillators at each node in the system.

2. The effect of acceleration at transmit node i on the frequency of the oscillator at node i [71].

3. The effect of displacement at transmit node i on the propagation delay of signals from transmit node i to the receive node

We develop a continuous-time three-state model describing the combined time offset and propagation delay, normalized rate/frequency offset, and acceleration dynamics between transmit node i and the receive node. This model is characterized by three parameters corresponding to the short-term oscillator stability, long-term oscillator stability, and kinematic stability. The continuous-time model is then discretized to facilitate tracking with a Kalman filter.

Numerical methods are used to compare the performance of the MISO system in two scenarios: (i) the conventional receiver-coordinated scenario where the combined time offsets and propagation delays are tracked only through periodic feedback of estimates from the receive node and (ii) a scenario where, in addition to the periodic time offset feedback, each receive node also observes measurements from a local accelerometer. This could be achieved, for example, by equipping each transmit node with an inertial measurement unit (IMU). Both time offset feedback and local accelerometer measurements are assumed to be periodic, but the local accelerometer measurements are assumed to be available much more frequently than feedback from the receive node. Numerical results show that local accelerometer measurements can significantly improve the performance of time offset tracking, consequently improving coherence for distributed transmit beamforming and distributed transmit nullforming and also potentially allowing for reduced feedback rates with respect to the conventional receiver-coordinated feedback-only approach.

4.2 System Model

Each node in the system shown in Fig. 4.1 is assumed to possess a single antenna. All forward link channels are modeled as single-path with identical gain and the time-varying propagation delay of the channel from transmit node i to the receive node is denoted as $\psi_i(t)$ with units of seconds for $i = 1, \ldots, N$.

We assume a protocol in which each transmit node periodically sends a sounding signal at known time (in the transmit node's local timebase) and the time-of-arrival of this signal is estimated at the receive node (in the receive node's local timebase). The receive node estimates the combined time offset and propagation delay of each of the transmit nodes and provides feedback to the transmit nodes to facilitate channel tracking, passband signal alignment, and distributed coherent transmission. As discussed in [17, 37, 43, 70], the transmit nodes can use Kalman filters to optimally combine this feedback with previously received feedback to generate minimum mean squared error (MMSE) predictions and facilitate coherent transmission between feedback updates.

The time-varying time offset and normalized rate/frequency offset between transmit node i and the receive node (as observed at the receive node) can be written as

$$\delta_{i,1}(t) = x_{i,1}(t) + \psi_i(t) - x_{0,1}(t) \qquad \text{(time offset)} \tag{4.1}$$

$$\delta_{i,2}(t) = x_{i,2}(t) + \dot{\psi}_i(t) - x_{0,2}(t) \qquad \text{(frequency offset)} \tag{4.2}$$

where $x_{i,1}(t)$ and $x_{i,2}(t)$ denote the clock offset and normalized clock rate offsets at node i, respectively, both with respect to some reference, and where we have adopted the convention that the receiver is node 0. To be clear, the "time offset" $\delta_{i,1}(t)$ includes both the relative clock offset $x_{i,1}(t) - x_{0,1}(t)$ and the propagation delay $\psi_i(t)$. Similarly, the "frequency offset" $\delta_{i,2}(t)$ includes both the relative clock rate offset $x_{i,2}(t) - x_{0,2}(t)$ and propagation effects in $\dot{\psi}_i(t)$. The following sections develop dynamic models for each of the constituent components in these expressions.

4.2.1 Clock Dynamics

The independent local oscillator at each node in the system behaves stochastically, causing time variations the each effective channel from transmit node i to the receive node. Based on the two-state models in [53,54], we can define the state of the oscillator at node i as

$$\boldsymbol{x}_i(t) = \begin{bmatrix} x_{i,1}(t) \\ x_{i,2}(t) \end{bmatrix} \tag{4.3}$$

where $x_{i,1}(t)$ is a time offset with units of seconds and $x_{i,2}(t)$ is a rate or frequency offset with units of sec/sec (dimensionless), both with respect to some nominal reference. The continuous-time state update equation is given as

$$\dot{\boldsymbol{x}}_i(t) = \begin{bmatrix} 0 & 1 \\ 0 & 0 \end{bmatrix} \boldsymbol{x}_i(t) + \boldsymbol{\xi}_i(t) \tag{4.4}$$

where $\boldsymbol{\xi}_i(t) = [\xi_{i,1}(t), \xi_{i,2}(t)]^\top$ and where $\xi_{i,1}(t)$ has units of sec/sec (dimensionless) and $\xi_{i,2}(t)$ has units of 1/sec. The white process noise $\boldsymbol{\xi}_i(t)$ is distributed as

$$\boldsymbol{\xi}_i(t) \sim \mathcal{N}(0, \boldsymbol{Q}) \tag{4.5}$$

with $\boldsymbol{Q} = \mathrm{diag}(q_1, q_2)$ and with q_1 a parameter with units of seconds corresponding to the short-term stability of the oscillator and q_2 a parameter with units of 1/sec corresponding to the long-term stability of the oscillator. We assume all oscillators in the system to have the same q_1 and q_2 parameters. Typical values for short-term and long-term stability parameters for different classes of oscillators can be found in [75].

4.2.2 Effect of Acceleration on Oscillator Frequency

It is well-known that, due to the mechanical nature of crystal oscillators, acceleration applied to a crystal oscillator causes a shift in the oscillator frequency [71]. We assume this effect to be additive with the frequency offsets caused by the non-kinematic clock dynamics as described in the previous section.

To facilitate exposition, we assume the one-dimensional kinematic model illustrated in Fig. **??**. The displacement from node i to the receiver is denoted as $d_i(t)$ with units of meters. Denoting the acceleration on node i is $a_i(t) = \ddot{d}_i(t)$, the results in [71] imply that the frequency offset caused by acceleration at node i can be expressed as

$$x_{i,2}(t) = \gamma \ddot{d}_i(t) = \gamma a_i(t) \tag{4.6}$$

where γ is the oscillator acceleration sensitivity parameter with units of $\mathrm{sec}^2/\mathrm{m}$. Typical values for the oscillator acceleration sensitivity parameter are described in [71] and are usually on the order of $10^{-10}\ \mathrm{sec}^2/\mathrm{m}$. We assume γ is known although this parameter may need to be estimated and/or calibrated in practice. Taking another derivative, we can write

$$\dot{x}_{i,2}(t) = \gamma \dot{a}_i(t) = \gamma j_i(t) \tag{4.7}$$

where $j_i(t)$ is the derivative of the acceleration at node i sometimes called the “jerk” [69].

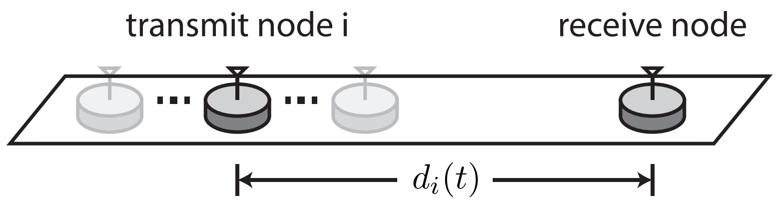

Figure 4.2: One dimensional kinematics model with time-varying displacement $d_i(t)$.

4.2.3 Effect of Displacement on Propagation Delay

Referring to Fig. 4.2 and assuming a single-path channel from transmit node i to the receive node, the propagation delay from node i to the receiver is given as

$$\psi_i(t) = \frac{d_i(t)}{c} \tag{4.8}$$

where c is the speed of light. We can take two derivatives to write

$$\ddot{\psi}_i(t) = \frac{a_i(t)}{c}. \tag{4.9}$$

This equation is consistent with the usual results for non-relativistic Doppler shifts. We can further define the propagation state

$$\boldsymbol{z}_i(t) = \begin{bmatrix} \psi_i(t) \\ \dot{\psi}_i(t) \end{bmatrix}. \tag{4.10}$$

It follows that

$$\dot{\boldsymbol{z}}_i(t) = \begin{bmatrix} 0 & 1 \\ 0 & 0 \end{bmatrix} \boldsymbol{z}_i(t) + \begin{bmatrix} 0 \\ \frac{1}{c} \end{bmatrix} a_i(t). \tag{4.11}$$

4.2.4 Complete Continuous-Time Model

We define the state

$$\boldsymbol{\delta}_i(t) = \begin{bmatrix} x_{i,1}(t) + \psi_i(t) - x_{0,1}(t) \\ x_{i,2}(t) + \dot{\psi}_i(t) - x_{0,2}(t) \\ a_i(t) \end{bmatrix}. \tag{4.12}$$

Note that the first and second terms of this state vector are the time offset (seconds) and normalized rate/frequency offset (dimensionless), respectively, of node i as observed at the receive node through the time-varying propagation delay $\psi_i(t)$. Unlike the time and frequency offsets with respect to an unknown reference clock, these offsets are observable.

Using the results from the previous sections, we can write

$$\begin{aligned} \dot{\boldsymbol{\delta}}_i(t) &= \begin{bmatrix} 0 & 1 & 0 \\ 0 & 0 & \frac{1}{c} \\ 0 & 0 & 0 \end{bmatrix} \boldsymbol{\delta}_i(t) + \begin{bmatrix} 1 & 0 & -1 & 0 & 0 \\ 0 & 1 & 0 & -1 & \gamma \\ 0 & 0 & 0 & 0 & 1 \end{bmatrix} \begin{bmatrix} \boldsymbol{\xi}_i(t) \\ \boldsymbol{\xi}_0(t) \\ j_i(t) \end{bmatrix} && (4.13) \\ &= \boldsymbol{A}\boldsymbol{\delta}_i(t) + \boldsymbol{B}\boldsymbol{\eta}_i(t) && (4.14) \end{aligned}$$

If we assume the kinematics follow a white-noise jerk model with $\mathrm{E}[j_i(t)j_i(t+\tau)] = q_3\delta(\tau)$ where q_3 has units of $\mathrm{m}^2/\mathrm{sec}^5$, then the white process noise $\boldsymbol{\eta}_i(t)$ is distributed as

$$\boldsymbol{\eta}_i(t) \sim \mathcal{N}(0, \bar{\boldsymbol{Q}}) \tag{4.15}$$

with $\bar{\boldsymbol{Q}} = \mathrm{E}[\boldsymbol{\eta}_i(t)\boldsymbol{\eta}_i^\top(t)] = \mathrm{diag}(q_1, q_2, q_1, q_2, q_3)$.

4.2.5 Complete Discrete-Time Model

To facilitate tracking with a Kalman filter, this section derives a discrete-time model from the continuous-time model developed in the previous section. The continuous-time transition matrix can be computed as

$$\boldsymbol{\Phi}(t) = e^{\boldsymbol{A}t} = \begin{bmatrix} 1 & t & \frac{t^2}{2c} \\ 0 & 1 & \frac{t}{c} \\ 0 & 0 & 1 \end{bmatrix}. \tag{4.16}$$

Let T denote the sampling period. Using standard methods to convert a continuous-time system to a discrete-time system, e.g., [76], we have a discrete-time state update given as

$$\boldsymbol{\delta}_i[k+1] = \boldsymbol{\Phi}(T)\boldsymbol{\delta}_i[k] + \boldsymbol{u}_i[k] \tag{4.17}$$

with

$$\boldsymbol{u}_i[k] = \int_{kT}^{(k+1)T} \boldsymbol{\Phi}((k+1)T - \tau)\boldsymbol{B}\boldsymbol{\eta}_i(\tau)\, d\tau. \tag{4.18}$$

Note that $\boldsymbol{u}_i[k]$ is Gaussian distributed with zero mean since it is a linear function of $\boldsymbol{\eta}_i(\tau)$ which is Gaussian and zero mean. The discrete-time process noise covariance matrix requires computing

$$\boldsymbol{C}(T) = \int_0^T \boldsymbol{\Phi}(T-\tau)\boldsymbol{B}\bar{\boldsymbol{Q}}\boldsymbol{B}^\top\boldsymbol{\Phi}^\top(T-\tau)\, d\tau. \tag{4.19}$$

Since

$$\boldsymbol{B}\bar{\boldsymbol{Q}}\boldsymbol{B}^\top = \begin{bmatrix} 2q_1 & 0 & 0 \\ 0 & 2q_2 + \gamma^2 q_3 & \gamma q_3 \\ 0 & \gamma q_3 & q_3 \end{bmatrix} \tag{4.20}$$

and

$$\mathbf{\Phi}(T-\tau) = \begin{bmatrix} 1 & T-\tau & \frac{(T-\tau)^2}{2c} \\ 0 & 1 & \frac{T-\tau}{c} \\ 0 & 0 & 1 \end{bmatrix} \tag{4.21}$$

it can be shown that

$$\boldsymbol{C}(T) = \int_0^T \sum_{\ell=0}^{4} \boldsymbol{X}_\ell (T-\tau)^\ell \, d\tau \tag{4.22}$$

$$= \boldsymbol{X}_0 T + \boldsymbol{X}_1 \frac{T^2}{2} + \boldsymbol{X}_2 \frac{T^3}{3} + \boldsymbol{X}_3 \frac{T^4}{4} + \boldsymbol{X}_4 \frac{T^5}{5} \tag{4.23}$$

where each $\boldsymbol{X}_\ell$ is a symmetric 3×3 matrix that is only a function of c, γ, q_1, q_2, and q_3 (not a function of T or τ). Some linear algebra results in

$$\boldsymbol{X}_0 = \begin{bmatrix} 2q_1 & 0 & 0 \\ 0 & 2q_2 + \gamma^2 q_3 & \gamma q_3 \\ 0 & \gamma q_3 & q_3 \end{bmatrix}, \tag{4.24}$$

$$\boldsymbol{X}_1 = \begin{bmatrix} 0 & 2q_2 + \gamma^2 q_3 & \gamma q_3 \\ 2q_2 + \gamma^2 q_3 & \frac{2\gamma q_3}{c} & \frac{q_3}{c} \\ \gamma q_3 & \frac{q_3}{c} & 0 \end{bmatrix}, \tag{4.25}$$

$$\boldsymbol{X}_2 = \begin{bmatrix} 2q_2 + \gamma^2 q_3 & \frac{3\gamma q_3}{2c} & \frac{q_3}{2c} \\ \frac{3\gamma q_3}{2c} & \frac{q_3}{c^2} & 0 \\ \frac{q_3}{2c} & 0 & 0 \end{bmatrix}, \tag{4.26}$$

$$\boldsymbol{X}_3 = \begin{bmatrix} \frac{\gamma q_3}{c} & \frac{q_3}{2c^2} & 0 \\ \frac{q_3}{2c^2} & 0 & 0 \\ 0 & 0 & 0 \end{bmatrix}, \text{ and} \tag{4.27}$$

$$\boldsymbol{X}_4 = \begin{bmatrix} \frac{q_3}{4c^2} & 0 & 0 \\ 0 & 0 & 0 \\ 0 & 0 & 0 \end{bmatrix}. \tag{4.28}$$

Hence, the discrete-time dynamics are fully characterized by the initial state $\boldsymbol{\delta}_i[0]$, the time-invariant state update matrix $\boldsymbol{F} = \boldsymbol{\Phi}(T)$, and the discrete-time process noise $\boldsymbol{u}_i(t) \sim \mathcal{N}(0, \boldsymbol{C}(T))$ with covariance $\boldsymbol{C}(T)$ from (4.22)–(4.28).

4.2.6 Observation Model

At each sampling instant $t = kT$, transmit node i receives a noisy observation of the acceleration state from its local accelerometer. At less frequent sampling instances $t = kT_f$

with $T_f = MT$ and M an integer greater than one, transmit node i receives feedback from the receive node corresponding to a noisy estimate of the time offset state. We assume no estimates are made of the normalized rate/frequency state. The feedback period is denoted as T_f. Assuming zero latency in the feedback from the receive node, the observation model at node i can be written as

$$\boldsymbol{y}_i[k] = \boldsymbol{H}[k]\boldsymbol{\delta}_i[k] + \boldsymbol{w}_i[k] \tag{4.29}$$

where

$$\boldsymbol{H}[k] = \begin{cases} \begin{bmatrix} 0 & 0 & 0 \\ 0 & 0 & 1 \end{bmatrix} & \frac{kT}{T_f} \text{ is not an integer} \\ \begin{bmatrix} 1 & 0 & 0 \\ 0 & 0 & 1 \end{bmatrix} & \frac{kT}{T_f} \text{ is an integer} \end{cases} \tag{4.30}$$

and where $\boldsymbol{w}_i[k]$ corresponds to measurement noise. It is reasonable to assume the noise in the accelerometer measurements is independent of the noise in the time offset estimates at the receive node. Hence

$$\boldsymbol{w}_i[k] \sim \mathcal{N}(0, \boldsymbol{R}) \tag{4.31}$$

with $\boldsymbol{R} = \mathrm{diag}(r_1, r_2)$. We assume these measurement noise parameters are identical for all nodes in the system.

Note that the r_1 measurement noise parameter specifies the variance of the time offset measurements at the receive node (which are subsequently fed back over an error-free link to the transmit nodes to facilitate tracking). It is well-known, e.g. [77, p.55], that the Cramer-Rao lower bound (CRLB) for delay estimation of signals observed in additive white Gaussian noise (AWGN) is inversely proportional to the signal-to-noise ratio (SNR) and the mean squared bandwidth of the signal. The analysis leading to this bound, however, assumes a baseband signal is processed to estimate the time offset. Weiss and Weinstein [78] showed that *passband* signal delay estimation performance also improves with carrier frequency when the SNR exceeds a certain threshold. Intuitively, above this SNR threshold, the presence of the carrier in the passband signal provides additional detail in the correlator output that can be used to refine delay estimates to a fraction of a carrier period.

As an example, in the case of a pre-integration SNR of 10 dB, bandwidth $B = 50$ MHz, waveform duration $T = 10$ μs, and carrier frequency $\omega_0 = 2\pi \cdot 1$ GHz, the passband CRLB implies that RMS delay estimation errors can be as small as approximately 4 ps. Experimental results reported in [79] with similar signaling parameters in an outdoor environment and with off-the-shelf hardware yielded RMS delay estimation errors of less than 10 ps.

The r_2 measurement noise parameter specifies the variance of the noise in the accelerometer measurements. We have assumed here a simplified model for the accelerometer that ignores any amplitude nonlinearities and/or bias effects. The value of r_2 depends on accelerometer noise specifications and the measurement bandwidth. As an example, the Analog Devices ADXL103/ADXL203 accelerometer datasheet [80] has a noise density specification of $110\mu g/\sqrt{\mathrm{Hz}}$. If a single-pole anti-aliasing filter with bandwidth BW Hz is used to limit the noise prior to sampling, the RMS accelerometer noise can be calculated as [80]

$$\mathrm{RMSnoise} \approx \left(110 \frac{\mu g}{\sqrt{\mathrm{Hz}}}\right)\left(\sqrt{\mathsf{BW} \cdot 1.6}\right)\left(9.8 \cdot 10^{-6} \frac{\mathrm{m/s^2}}{\mu g}\right) \tag{4.32}$$

with units of $\mathrm{m/s^2}$ and where the factor of 1.6 is due to the rolloff of the single-pole anti-aliasing filter. For example, with an accelerometer sampling period of $T = 0.01$, we can set $\mathsf{BW} = 50$ Hz and compute $\mathrm{RMSnoise} \approx 9.64 \times 10^{-3}$ $\mathrm{m/s^2}$. The r_2 parameter then follows as $r_2 = (\mathrm{RMSnoise})^2$. In this example, we have $r_2 \approx 9.3 \times 10^{-5} \approx 1 \times 10^{-4}\ \mathrm{m}^2/\mathrm{s}^4$.

4.3 Numerical Results

In this section, we demonstrate the performance advantages of using local accelerometer measurements to improve the effective tracking performance and, consequently, improve the coherence of the distributed transmission system. Table 4.2 lists the parameters for all of the numerical results in this section.

The oscillator stability parameters were chosen to be similar to the "good" XO parameters described in [75]. The white noise jerk process noise intensity was chosen so that the changes in the acceleration over the sampling period T were on the order of $\sqrt{Tq_3} = 0.02\ \mathrm{m/sec}^2$. The oscillator sensitivity parameter was chosen according to typical values described in [71]. The measurement noise parameters depend on various factors such as the integrated SNR and the quality of the accelerometer. We have assumed here sufficient SNR so that the time offset estimation performance follows the Weiss-Weinstein bounds for passband signals [78] and are on the order of picoseconds as has been experimentally demonstrated in [51]. The accelerometer measurement variance r_2 was set according to the example calculation based on the ADXL103/ADXL203 accelerometer [80] in the previous section.

Fig. 4.3 shows the tracking performance of a Kalman filter channel tracker with and without local accelerometer observations using the parameters in Table 4.2 at the 900 MHz nominal carrier frequency averaged over 1000 independent realizations of the clock and kinematic processes. These results are shown in RMS phase prediction error (degrees) versus time. At times $t = 0, 0.5, 1.0, \ldots$, the transmit node receives feedback from the receive node and we see the RMS phase prediction error is small when this feed-

Table 4.1: Parameters used in numerical simulation.

Parameter	Value	Units	Meaning
q_1	10^{-22}	sec	oscillator short-term stability
q_2	10^{-23}	1/sec	oscillator long-term stability
q_3	$4 \cdot 10^{-2}$	$\mathrm{m}^2/\mathrm{sec}^5$	white noise jerk process noise intensity
γ	10^{-10}	$\mathrm{sec}^2/\mathrm{m}$	oscillator sensitivity to acceleration
r_1	$4 \cdot 10^{-24}$	sec^2	time offset measurement noise variance
r_2	10^{-4}	$\mathrm{m}^2/\mathrm{sec}^4$	accelerometer measurement variance
T	0.01	sec	sampling period for accelerometer measurements
T_f	0.50	sec	sampling period for time offset measurements (feedback)
ω_0	$2\pi \cdot 900 \cdot 10^6$	rad/sec	nominal carrier frequency

back is received. In the case without local accelerometer observations, the kinematics and clock dynamics cause the phase predictions to quickly become inaccurate. For the case with local accelerometer observations, the transmitters use these observations (received at times $t = 0, 0.01, 0.02, \dots$) to better predict the combined time offset and propagation delay and reduce the RMS phase prediction error between feedback periods. While the local accelerometer measurements don't account for the clock dynamics, they do provide useful information about the kinematic effects on the local clock frequency and changes in the propagation delay.

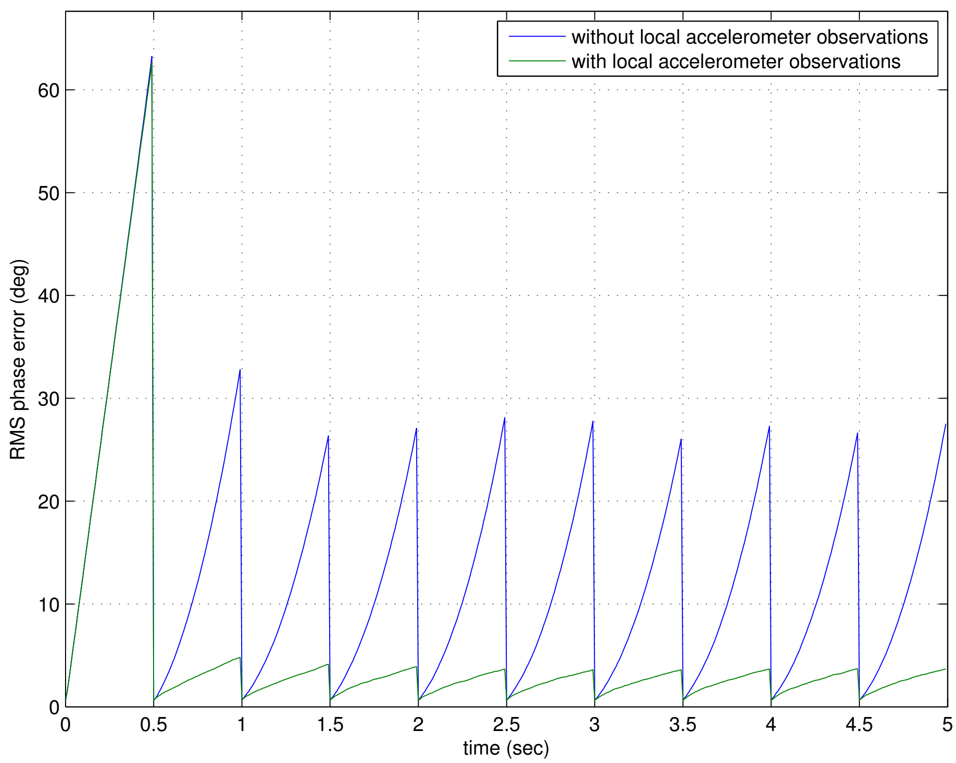

Figure 4.3: RMS phase prediction error in degrees versus time with and without local accelerometer observations.

Fig. 4.4 shows the beamforming gain of an $N = 10$ node distributed beamformer with each transmit node in the system using a Kalman filter to track and predict the effective channel dynamics. The performance is compared with and without local accelerometer observations using the parameters in Table 4.2 at the 900 MHz nominal carrier frequency averaged over 1000 independent realizations of the clock and kinematic processes and assume identical channel magnitudes from each transmit node to the receive node. Under this assumption, it has been shown [43] that the average beamforming gain with respect to incoherent transmission is related to the variance of the phase prediction errors according to

$$\mathrm{E}[\text{beamforming gain}] = Ne^{-\sigma_\phi^2(t_p)} + \left(1 - e^{-\sigma_\phi^2(t_p)}\right) \tag{4.33}$$

where $\sigma_\phi^2(t_p)$ denotes the phase prediction variance at prediction time t_p from the last feedback update. In this case, since the ideal beamforming gain of an $N = 10$ node array is 10 dB, these results show that local accelerometer observations allow the distributed transmit array to maintain performance almost indistinguishable from an ideal beamformer for $t > 0.5$. If local accelerometer observations are not available, the kinematic effects are poorly tracked and the distributed array loses approximately 1 dB of beamforming gain just prior to receiving a feedback update from the receiver.

Fig. 4.5 shows the *nullforming* gain of an $N = 10$ node distributed beamformer with each transmit node in the system using a Kalman filter to track and predict the effective channel dynamics under the same assumptions as the previous results. The goal in this case is to minimize the power at the receiver. Nullforming is used, for example, in cognitive radio underlay networks to avoid interfering with primary users [81]. In [43], it was shown that the average nullforming gain with respect to incoherent transmission is related to the variance of the phase prediction errors according to

$$\mathrm{E}[\text{nullforming gain}] = 1 - e^{-\sigma_\phi^2(t_p)}. \tag{4.34}$$

where $\sigma_\phi^2(t_p)$ denotes the phase prediction variance at prediction time t_p from the last

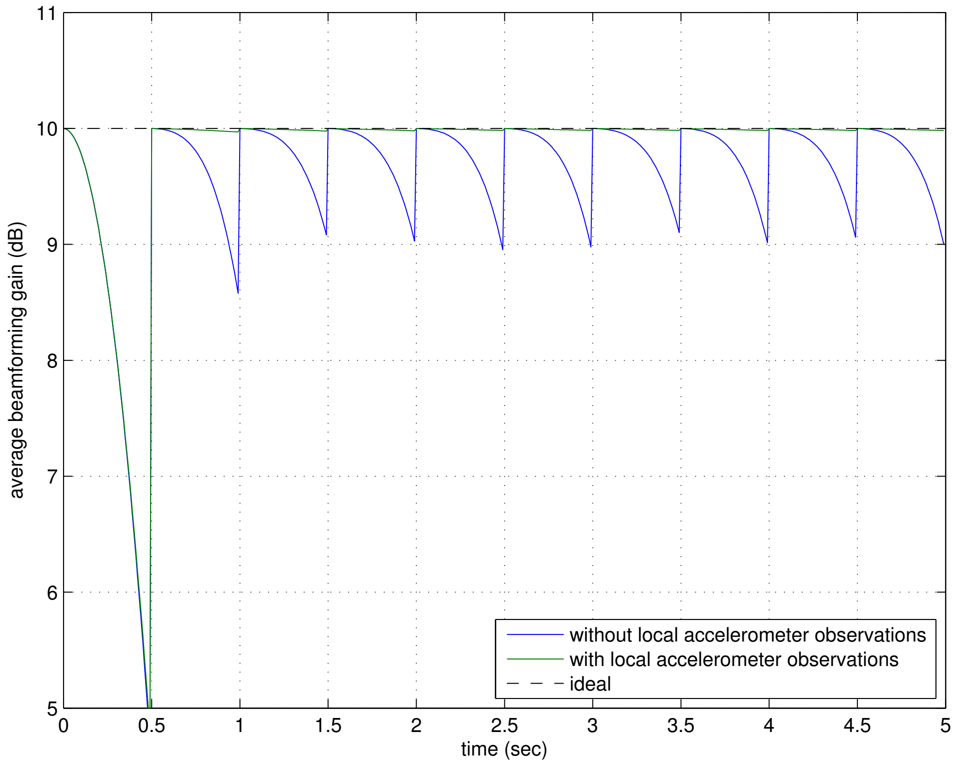

Figure 4.4: Average beamforming gain with respect to incoherent transmission in dB for an $N = 10$ node transmit cluster versus time with and without local accelerometer observations.

feedback update. These results show that accelerometer observations allow for nulls better than 20 dB below incoherent transmission whereas a system without accelerometer observations has nulls that are often less than 10 dB below incoherent transmission. Intuitively, the large performance advantage of the system with accelerometer observations in this example is due to the fact that nulls tend to be more sensitive to phase prediction errors than beams. By using local accelerometer measurements, the variance of the phase prediction errors is significantly reduced and the nullforming performance is significantly improved.

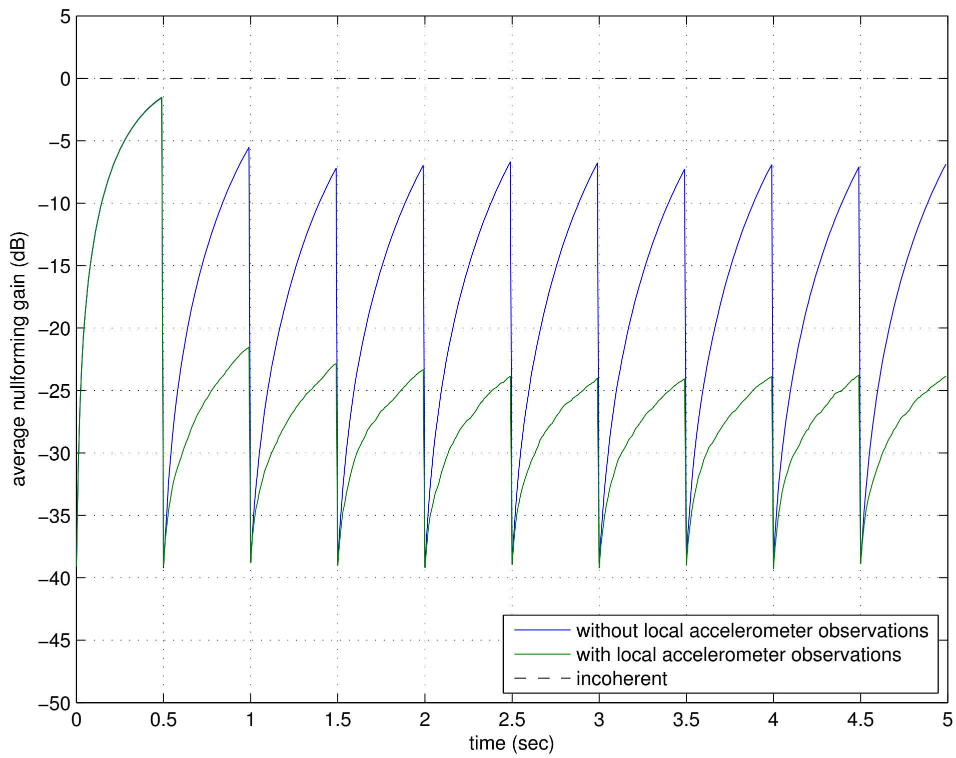

Figure 4.5: Average nullforming gain with respect to incoherent transmission in dB for an $N = 10$ node transmit cluster versus time with and without local accelerometer observations.

It is also of interest to understand how accelerometer measurements can be used to reduce feedback overhead in distributed transmission systems. Fig. 4.6 shows the achievable reduction in the feedback update rate $\frac{1}{T_f}$ of a system *with* accelerometer measurements achieving equivalent performance of a conventional receiver-coordinated system *without* accelerometer measurements. To be specific, we denote the feedback rate with and without accelerometer measurements as $\frac{1}{T_f^{(\mathrm{wam})}}$ and $\frac{1}{T_f^{(\mathrm{woam})}}$, respectively. For a fixed value of $T_f^{(\mathrm{woam})}$, we compute the performance of the conventional receiver-coordinated system without accelerometer measurements by temporally averaging the Kalman filter RMS phase prediction errors after the 20^{th} observation and before the 21^{st} observation (similar results are obtained by considering beamforming or nullforming gain as the performance metric). Setting $T_f^{(\mathrm{wam})} = T_f^{(\mathrm{woam})}$ and running the same experiment on the system with accelerometer measurements results in improved performance (reduced temporally-averaged RMS phase prediction errors). Keeping the accelerometer measurement period $T = 0.01$ fixed, we then decrease the feedback update rate $\frac{1}{T_f^{(\mathrm{wam})}}$ until the system with accelerometer measurements achieves identical performance to the conventional receiver-coordinated system without accelerometer measurements with feedback update rate $\frac{1}{T_f^{(\mathrm{woam})}}$.

The results in Fig. 4.6 plot the reduction in the feedback rate $\frac{1/T_f^{(\mathrm{woam})}}{1/T_f^{(\mathrm{wam})}}$ versus the feedback rate without accelerometer compensation $\frac{1}{T_f^{(\mathrm{woam})}}$. For example, a value of two corresponds to the case where the system with accelerometer compensation can achieve the same performance as a system without accelerometer compensation by reducing the feedback rate by a factor of two. These results show how a system with accelerometer measurements can achieve the same performance as a system without accelerometer measurements with significantly less feedback overhead. Larger feedback rate reductions occur in this example when the feedback rate in the conventional receiver-coordinated system is low.

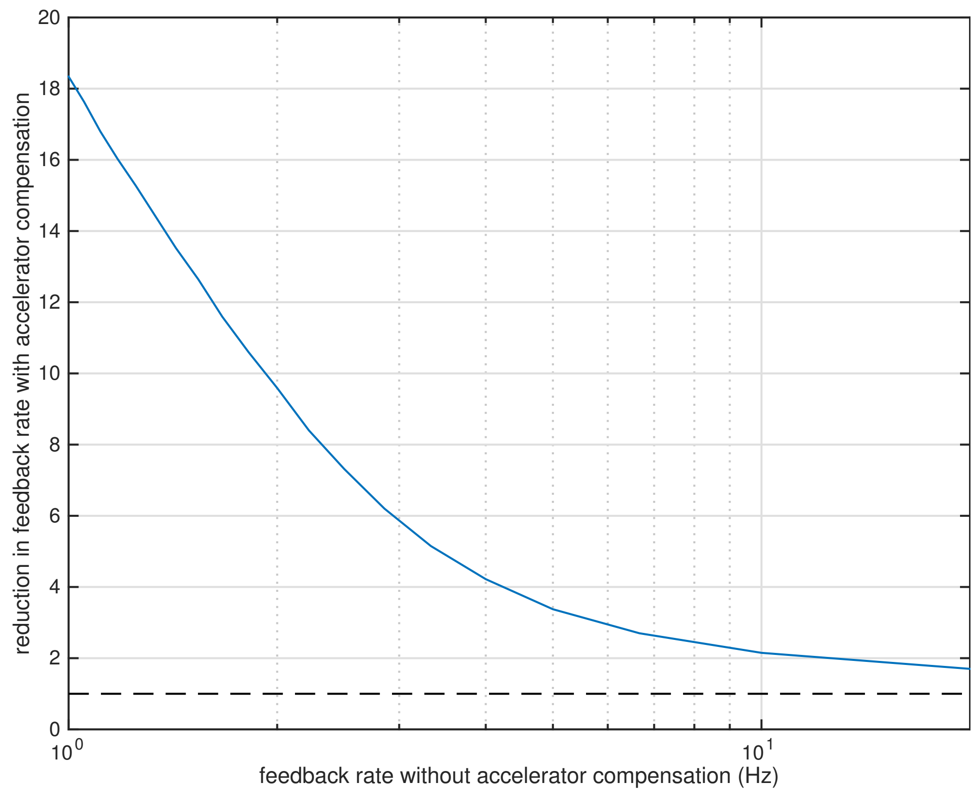

Figure 4.6: Reduction in feedback rate for a system with accelerometer measurements achieving equivalent tracking performance of a conventional receiver-coordinated system without accelerometer measurements. The accelerometer measurement period was fixed at $T = 0.01$ seconds.

4.4 Acceleration Bias

The previous results assumed an ideal accelerometer that measures the acceleration of the transmit node with just some white noise. In reality however, accelerometers suffer from a consistent bias, that varies from one device to another. In this section we take a quick look at the 1-D motion effects on oscillator stability and the tracking performance when an unknown bias is introduced in the observation model.

4.4.1 Effect of Acceleration Bias

The initial state space model is:

$$\boldsymbol{\delta}_i[k+1] = \boldsymbol{\Phi}(T)\boldsymbol{\delta}_i[k] + \boldsymbol{u}_i[k]$$

with the states:

$$\boldsymbol{\delta}_i[k] = \begin{bmatrix} x_{i,1}[k] + \psi_i[k] - x_{0,1}[k] \\ x_{i,2}[k] + \dot{\psi}_i[k] - x_{0,2}[k] \\ a_i[k] \end{bmatrix}.$$

The states are time (sec), rate (sec/sec) and acceleration (m/sec^2). The only difference is the addition of an unknown bias $\boldsymbol{b[k]}$ in the observations:

$$\boldsymbol{y}_i[k] = \boldsymbol{H}[k]\boldsymbol{\delta}_i[k] + \boldsymbol{b}[k] + \boldsymbol{w}_i[k] \tag{4.35}$$

Note that we are observing phase and acceleration, so the vector is $\boldsymbol{b[k]} = [0, b[k]]$. To analyze this effect we performed Monte Carlo simulations. For each set of observations, the bias $b[k]$ was a random number from the distribution $\mathcal{N}(0, \sigma_b^2)$, with $\sigma_b = 0.05$

$\mathrm{m/s^2}$. This simulates the effect of multiple transmitters with different biases on the phase error. The accelerometer has a sampling frequency of 100Hz, the phase observations are at 2Hz, and we run 20 seconds long simulations. For quick results we only averaged over 100 runs.

The prediction errors for this case are shown in Fig. 4.7. It is clear that an unknown and unaccounted for bias has a huge effect on the phase prediction error.

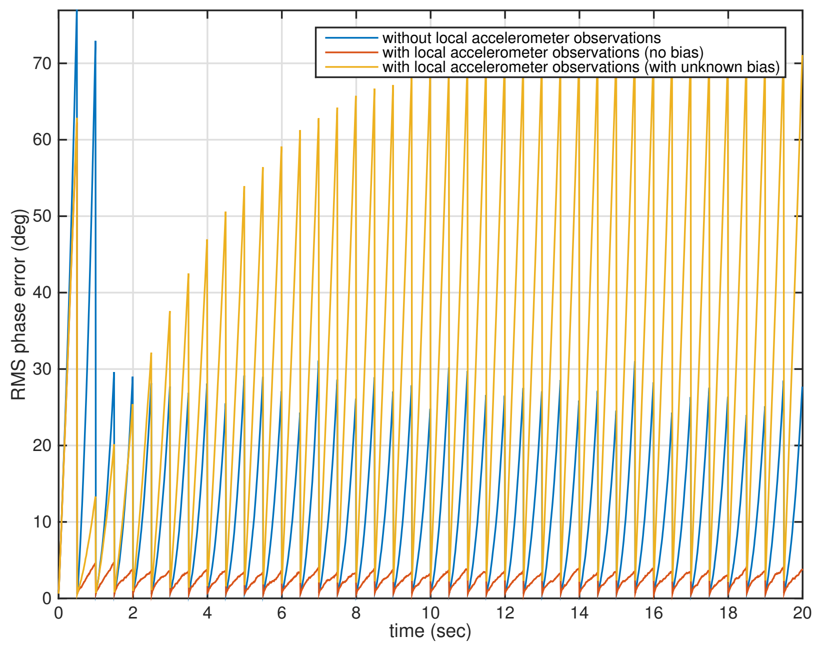

Figure 4.7: KF prediction error comparison.

4.4.2 Acceleration Bias State-space Model

We add a new state to our original system to minimize the effect of the bias on the tracking performance. We have previously showed that if the observations have a bias term that is not accounted for, the KF tracking performance is very poor. We will now develop a model in which the bias is accounted for in the state space system. The observation model will be changed accordingly, to observe the sum of the acceleration term and the bias term.

4.4.3 Continuous Time Model

Recall that the three state model contained the time offset (*sec*), normalized rate or frequency offset (*sec/sec*) and the acceleration of the transmit node:

$$\boldsymbol{\delta}_i(t) = \begin{bmatrix} x_{i,1}(t) + \psi_i(t) - x_{0,1}(t) \\ x_{i,2}(t) + \dot{\psi}_i(t) - x_{0,2}(t) \\ a_i(t) \end{bmatrix}.$$

.

We add a new state $b_i(t)$ that represents the unknown bias of an accelerometer to form a 4-state vector:

$$\boldsymbol{\delta}_i(t) = \begin{bmatrix} x_{i,1}(t) + \psi_i(t) - x_{0,1}(t) \\ x_{i,2}(t) + \dot{\psi}_i(t) - x_{0,2}(t) \\ a_i(t) \\ b_i(t) \end{bmatrix}. \tag{4.36}$$

.

The state space evolution of the system is:

$$\dot{\boldsymbol{\delta}}_i(t) = \boldsymbol{A}\boldsymbol{\delta}_i(t) + \boldsymbol{B}\boldsymbol{\eta}_i(t) \tag{4.37}$$

with

$$\boldsymbol{A} = \begin{bmatrix} 0 & 1 & 0 & 0 \\ 0 & 0 & \frac{1}{c} & 0 \\ 0 & 0 & 0 & 0 \\ 0 & 0 & 0 & 0 \end{bmatrix}, \boldsymbol{B} = \begin{bmatrix} 1 & 0 & -1 & 0 & 0 & 0 \\ 0 & 1 & 0 & -1 & \gamma & 0 \\ 0 & 0 & 0 & 0 & 1 & 0 \\ 0 & 0 & 0 & 0 & 0 & 1 \end{bmatrix} \tag{4.38}$$

and $\boldsymbol{\eta}_i(t)$ is distributed as

$$\boldsymbol{\eta}_i(t) \sim \mathcal{N}(0, \bar{\boldsymbol{Q}}) \tag{4.39}$$

with $\bar{\boldsymbol{Q}} = \mathrm{E}[\boldsymbol{\eta}_i(t)\boldsymbol{\eta}_i^\top(t)] = \mathrm{diag}(q_1, q_2, q_1, q_2, q_3, q_4)$.

Terms q_1 and q_2 are the oscillator stability parameters with units of seconds and 1/sec respectively, q_3 is the parameter of the white noise jerk model for the accelerometer, with units of $\mathrm{m}^2/\mathrm{sec}^5$ and q_4 is a very small white noise process parameter for the bias state, with units of $\mathrm{m}^2/\mathrm{sec}^5$.

4.4.4 Discrete Time Model

The discrete time model can be derived after the computation of the continuous time transition matrix:

$$\boldsymbol{\Phi}(t) = e^{\boldsymbol{A}t} = \begin{bmatrix} 1 & t & \frac{t^2}{2c} & 0 \\ 0 & 1 & \frac{t}{c} & 0 \\ 0 & 0 & 1 & 0 \\ 0 & 0 & 0 & 1 \end{bmatrix}. \tag{4.40}$$

The discrete-time state update equation becomes:

$$\boldsymbol{\delta}_i[k+1] = \boldsymbol{\Phi}(T)\boldsymbol{\delta}_i[k] + \boldsymbol{u}_i[k] \tag{4.41}$$

where T is the sampling period. The discrete time noise process $\boldsymbol{u}_i[k]$ has a covariance matrix which can be computed from the equation:

$$\boldsymbol{C}(T) = \int_0^T \boldsymbol{\Phi}(T-\tau)\boldsymbol{B}\bar{\boldsymbol{Q}}\boldsymbol{B}^\top\boldsymbol{\Phi}^\top(T-\tau)\,d\tau. \tag{4.42}$$

4.4.5 Observation Model

We assume we observe the sum of the acceleration and the bias at a higher rate than the phase measurements. The observation model is:

$$\boldsymbol{y}_i[k] = \boldsymbol{H}[k]\boldsymbol{\delta}_i[k] + \boldsymbol{w}_i[k] \tag{4.43}$$

where

$$\boldsymbol{H}[k] = \begin{cases} \begin{bmatrix} 0 & 0 & 0 & 0 \\ 0 & 0 & 1 & 1 \end{bmatrix} & \frac{kT}{T_f} \text{ is not an integer} \\ \begin{bmatrix} 1 & 0 & 0 & 0 \\ 0 & 0 & 1 & 1 \end{bmatrix} & \frac{kT}{T_f} \text{ is an integer} \end{cases} \tag{4.44}$$

and measurement noise

$$\boldsymbol{w}_i[k] \sim \mathcal{N}(0, \boldsymbol{R}) \tag{4.45}$$

with $\boldsymbol{R} = \mathrm{diag}(r_1, r_2)$.

4.4.6 4-State Simulation Results

The bias term was given an initial state variance of $(0.05\mathrm{m/sec})^2$. We simulated 1000 separate runs to obtain an average behavior.

An example of the state evolution is shown in Fig. 4.8. It can be seen that the bias has a constant offset.

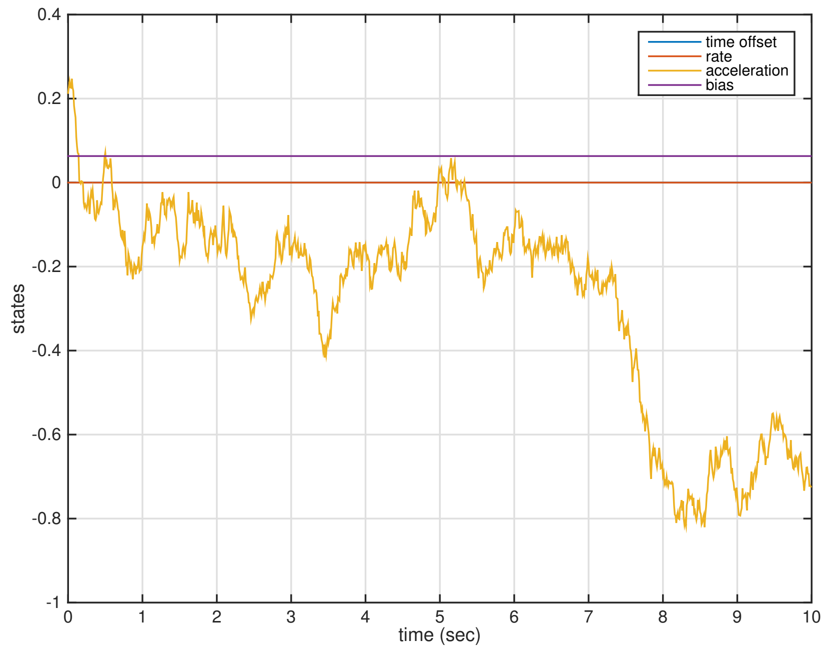

Figure 4.8: Example of state evolution.

Fig. 4.9 shows the RMS phase errors in three scenarios: when there is no acceleration information, when the acceleration has zero bias and when the acceleration has a bias term. It can be seen that the Kalman filter takes a couple of intervals to adapt to the bias term, but that in steady state the performance is very similar to the zero bias case.

A closer look in Fig. 4.10 shows that there is a slight performance loss due to the unknown bias, but less than a half of a degree.

The results show that the bias can cause problems to the channel tracking if it is

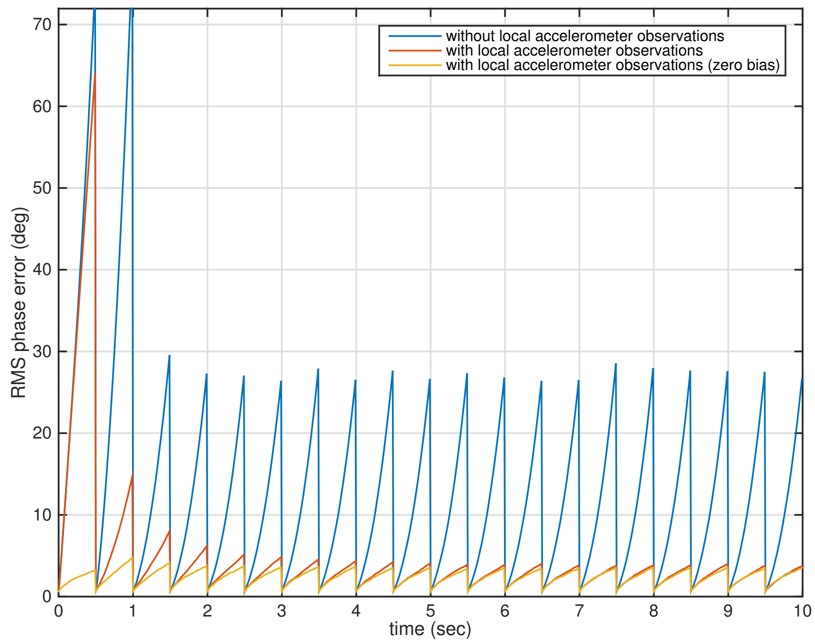

Figure 4.9: Phase error of the Kalman filter state phase predictions compared to the actual state.

unaccounted for, but by extending the state space description to include it we are able to minimize the performance loss.

4.4.7 Expansion to Three Dimensions

This section expands the previous 1-D model to a 3-D kinematic model. We develop an 8-state system model in which acceleration measurements from three axes are obtained and used together with the acceleration sensitivity vector to improve the tracking performance of a Kalman filter. We will show the derivation of the state space system and simulation results.

Compared to the one dimensional motion described in the previous sections, the three dimensional motion has a nonlinear effect on the propagation delay. In addition, the sensitivity of the oscillator to acceleration effects also has a three dimensional behavior.

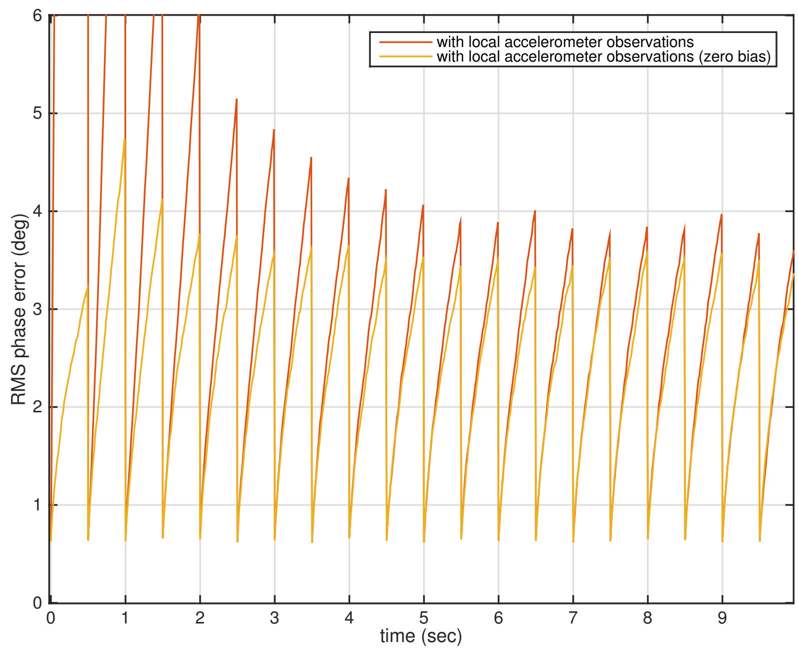

Figure 4.10: Phase error of the Kalman filter state phase predictions compared to the actual state (a closer look).

To simplify the model, we make the following assumptions:

- The distance between the two nodes is much larger than the distance traveled by the transmitter during the simulation.
- The axes are chosen such that the x-axis is in the direction of the receiver.
- The sensitivity vector showing the direction in which acceleration affects the oscillator rate (frequency) is known.

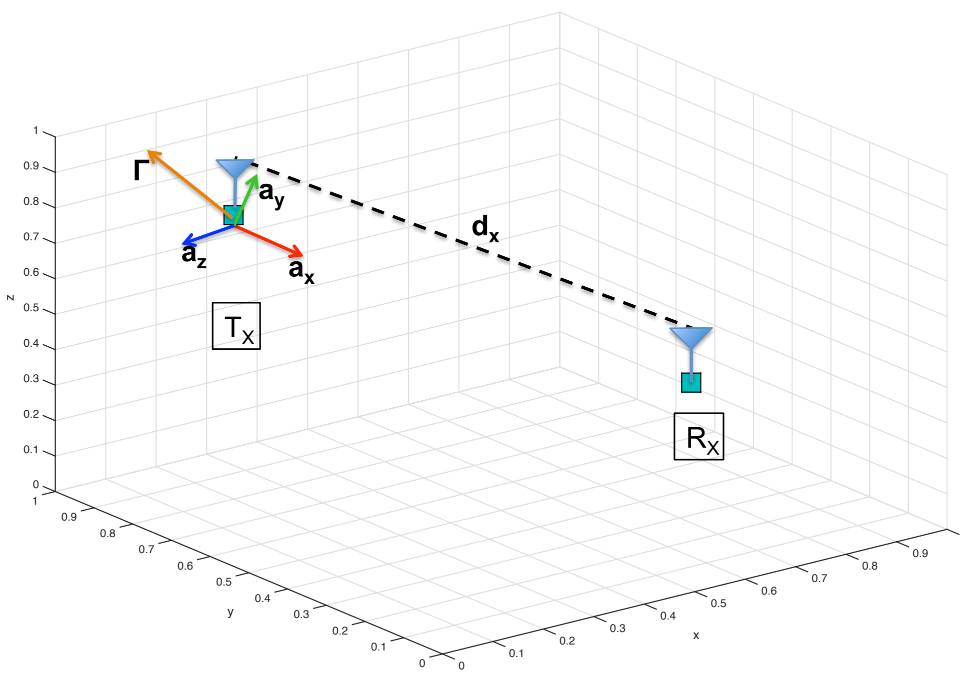

Figure 4.11: Diagram showing one fixed receiver and one moving transmitter.

Fig. 4.11 shows a diagram of two nodes, one fixed receiver and one moving transmitter. In the three dimensional case, the acceleration and bias terms become vectors. Denoting $\boldsymbol{a}_i(t) = \begin{bmatrix} a_{xi}(t) & a_{yi}(t) & a_{zi}(t) \end{bmatrix}^\top$ as the acceleration vector, and $\boldsymbol{b}_i(t) = \begin{bmatrix} b_{xi}(t) & b_{yi}(t) & b_{zi}(t) \end{bmatrix}^\top$ as the bias vector, we can write the new state vector as:

$$\boldsymbol{\delta}_i(t) = \begin{bmatrix} x_{i,1}(t) + \psi_i(t) - x_{0,1}(t) \\ x_{i,2}(t) + \dot{\psi}_i(t) - x_{0,2}(t) \\ \boldsymbol{a}_i(t) \\ \boldsymbol{b}_i(t) \end{bmatrix}. \tag{4.46}$$

.

We assume that only the motion on the x-axis is affecting the propagation delay between Tx and Rx. Thus we can write the propagation delay term as:

$$\psi_i(t) = \frac{d_{xi}(t)}{c} \tag{4.47}$$

By taking the double derivative we obtain:

$$\ddot{\psi}_i(t) = \frac{a_{xi}(t)}{c}. \tag{4.48}$$

For the effect of acceleration on the oscillator frequency, we use all three acceleration directions together with the sensitivity vector Γ. This leads to a similar "jerk" model as the 1D case. By taking the dot product of the derivative of the acceleration vector (jerk) and the sensitivity vector, we can obtain the effect on the frequency (rate) terms as:

$$x_{i,2}(t) = \boldsymbol{\Gamma} \cdot \dot{\boldsymbol{a}}_i(t) = \gamma_x j_{xi}(t) + \gamma_y j_{yi}(t) + \gamma_z j_{zi}(t) \tag{4.49}$$

Note that here the bold assumption is that Γ is constant (implying no rotation of the node) and known.

4.4.8 3D Continuous Time Model

The state space evolution of the system has the same form as in the 1D case. However, note that there are 8 states now. Hence, $\boldsymbol{A}$ is an 8x8 matrix and $\boldsymbol{B}$ is an 8x10 matrix to account for all the noise terms. The state space model is:

$$\dot{\boldsymbol{\delta}}_i(t) = \boldsymbol{A}\boldsymbol{\delta}_i(t) + \boldsymbol{B}\boldsymbol{\eta}_i(t) \tag{4.50}$$

with:

$$\boldsymbol{A} = \begin{bmatrix} 0 & 1 & 0 & \dots & 0 \\ 0 & 0 & \frac{1}{c} & \dots & 0 \\ 0 & 0 & 0 & \dots & 0 \\ \vdots & \vdots & \vdots & \ddots & \vdots \\ 0 & 0 & 0 & \dots & 0 \end{bmatrix}, \boldsymbol{B} = \begin{bmatrix} 1 & 0 & -1 & 0 & 0 & 0 & 0 & 0 & 0 & 0 \\ 0 & 1 & 0 & -1 & \gamma_x & \gamma_y & \gamma_z & 0 & 0 & 0 \\ 0 & 0 & 0 & 0 & 1 & 0 & 0 & 0 & 0 & 0 \\ 0 & 0 & 0 & 0 & 0 & 1 & 0 & 0 & 0 & 0 \\ 0 & 0 & 0 & 0 & 0 & 0 & 1 & 0 & 0 & 0 \\ 0 & 0 & 0 & 0 & 0 & 0 & 0 & 1 & 0 & 0 \\ 0 & 0 & 0 & 0 & 0 & 0 & 0 & 0 & 1 & 0 \\ 0 & 0 & 0 & 0 & 0 & 0 & 0 & 0 & 0 & 1 \end{bmatrix}, \boldsymbol{\eta_i(t)} = \begin{bmatrix} \boldsymbol{\xi}_i(t) \\ \boldsymbol{\xi}_i(t) \\ \boldsymbol{j}_i(t) \\ \boldsymbol{\beta}_i(t) \end{bmatrix} \tag{4.51}$$

and $\boldsymbol{\eta}_i(t)$ is distributed as

$$\boldsymbol{\eta}_i(t) \sim \mathcal{N}(0, \bar{\boldsymbol{Q}}) \tag{4.52}$$

with $\bar{\boldsymbol{Q}} = \mathrm{E}[\boldsymbol{\eta}_i(t)\boldsymbol{\eta}_i^\top(t)] = \mathrm{diag}(q_1, q_2, q_1, q_2, q_3, q_3, q_3, q_4, q_4, q_4)$.

Terms q_1 and q_2 are the oscillator stability parameters with units of seconds and 1/sec respectively, q_3 is the parameter of the white noise jerk model for the accelerometer, with units of $\mathrm{m}^2/\mathrm{sec}^5$ and q_4 is a very small white noise process parameter for the bias states, with units of $\mathrm{m}^2/\mathrm{sec}^5$.

4.4.9 3D Discrete Time Model

The discrete time model can be derived after the computation of the continuous time transition matrix:

$$\mathbf{\Phi}(t) = e^{\boldsymbol{A}t} = \begin{bmatrix} 1 & t & \frac{t^2}{2c} & \dots & 0 \\ 0 & 1 & \frac{t}{c} & \dots & 0 \\ 0 & 0 & 1 & \dots & 0 \\ \vdots & \vdots & \vdots & \ddots & \vdots \\ 0 & 0 & 0 & \dots & 1 \end{bmatrix}. \tag{4.53}$$

The discrete-time state update equation becomes:

$$\boldsymbol{\delta}_i[k+1] = \mathbf{\Phi}(T)\boldsymbol{\delta}_i[k] + \boldsymbol{u}_i[k] \tag{4.54}$$

where T is the sampling period. The discrete time noise process $\boldsymbol{u}_i[k]$ has a covariance matrix which can be computed from the equation:

$$\boldsymbol{C}(T) = \int_0^T \mathbf{\Phi}(T-\tau)\boldsymbol{B}\bar{\boldsymbol{Q}}\boldsymbol{B}^\top\mathbf{\Phi}^\top(T-\tau)\, d\tau. \tag{4.55}$$

4.4.10 3D Observation Model

We assume we observe the sum of the acceleration and the bias at a higher rate than the phase measurements. The observation model is:

$$\boldsymbol{y}_i[k] = \boldsymbol{H}[k]\boldsymbol{\delta}_i[k] + \boldsymbol{w}_i[k] \tag{4.56}$$

where

$$\boldsymbol{H}[k] = \begin{cases} \begin{bmatrix} 0 & 0 & 0 & 0 & 0 & 0 & 0 & 0 \\ 0 & 0 & 1 & 0 & 0 & 1 & 0 & 0 \\ 0 & 0 & 0 & 1 & 0 & 0 & 1 & 0 \\ 0 & 0 & 0 & 0 & 1 & 0 & 0 & 1 \end{bmatrix} & \frac{kT}{T_f} \text{ is not an integer} \\ \begin{bmatrix} 1 & 0 & 0 & 0 & 0 & 0 & 0 & 0 \\ 0 & 0 & 1 & 0 & 0 & 1 & 0 & 0 \\ 0 & 0 & 0 & 1 & 0 & 0 & 1 & 0 \\ 0 & 0 & 0 & 0 & 1 & 0 & 0 & 1 \end{bmatrix} & \frac{kT}{T_f} \text{ is an integer} \end{cases} \tag{4.57}$$

and measurement noise

$$\boldsymbol{w}_i[k] \sim \mathcal{N}(0, \boldsymbol{R}) \tag{4.58}$$

with $\boldsymbol{R} = \mathrm{diag}(r_1, r_2, r_2, r_2)$.

The values for the simulation parameters are shown in the table below:

The bias terms were given an initial state variance of $(0.05\mathrm{m/sec})^2$. We simulated 1000 separate runs to obtain an average behavior.

Fig. 4.12 shows the RMS phase errors in three scenarios: when there is no acceleration information, when the acceleration has zero bias and when the acceleration has a bias term. It can be seen that the Kalman filter takes a couple of intervals to adapt to the bias term, but that in steady state the performance is very similar to the zero bias case.

The results are similar to the 1D case, showing that in this scenario and with our assumptions, the model states can be tracked.

One test we performed was to look at a mismatched sensitivity vector and analyze how this affects the performance. For this, we modified the Γ vector by flipping the axes

Table 4.2: Parameters used in 3D simulation.

Parameter	Value	Units	Meaning
q_1	10^{-22}	sec	oscillator short-term stability
q_2	10^{-23}	1/sec	oscillator long-term stability
q_3	$4 \cdot 10^{-2}$	$\mathrm{m}^2/\mathrm{sec}^5$	white noise jerk process noise intensity
q_4	$1 \cdot 10^{-25}$	$\mathrm{m}^2/\mathrm{sec}^5$	white noise bias process noise intensity
γ_x	10^{-10}	$\mathrm{sec}^2/\mathrm{m}$	oscillator sensitivity to acceleration
γ_y	10^{-12}	$\mathrm{sec}^2/\mathrm{m}$	oscillator sensitivity to acceleration
γ_z	$2 \cdot 10^{-12}$	$\mathrm{sec}^2/\mathrm{m}$	oscillator sensitivity to acceleration
r_1	$4 \cdot 10^{-24}$	sec^2	time offset measurement noise variance
r_2	10^{-4}	$\mathrm{m}^2/\mathrm{sec}^4$	accelerometer measurement variance
T	0.01	sec	sampling period for accelerometer measurements
T_f	0.50	sec	sampling period for time offset measurements (feedback)
ω_0	$2\pi \cdot 900 \cdot 10^6$	rad/sec	nominal carrier frequency

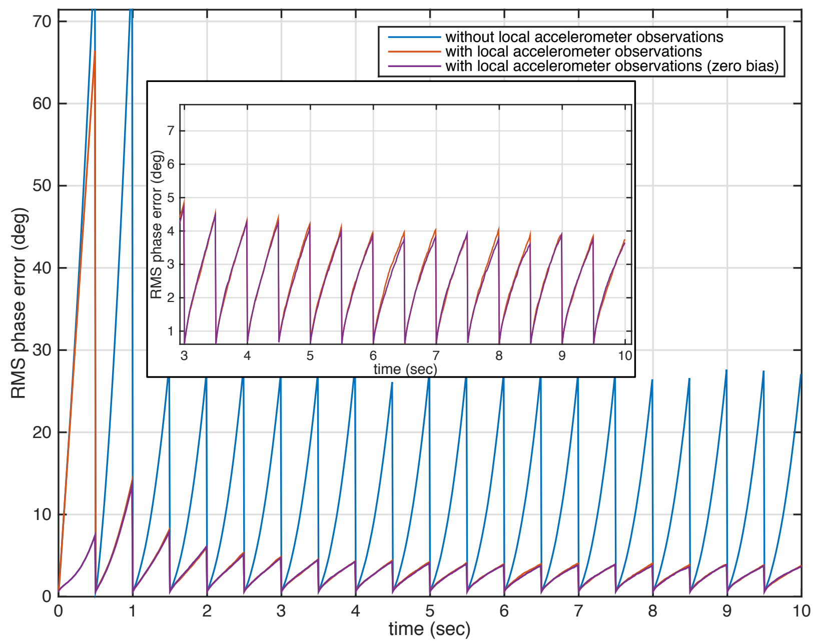

Figure 4.12: Phase error of the Kalman filter state phase predictions compared to the actual state.

(e.g. $\gamma_x = 10^{-12}$,$\gamma_y = 10^{-12}$ and $\gamma_z = 10^{-10}$). This in turn would change the discrete time noise covariance matrix computed in 4.55. By using the original covariance matrix in the Kalman filter, we compared the Kalman filter performance.

Fig. 4.13 shows that the mismatch in Γ has a significant effect on the offset error.

4.5 Conclusion

In this chapter we developed a model and analyzed the performance of distributed coherent transmission in a MISO communication system with time-varying propagation channels. The analysis accounted for the effects of independent clock dynamics as well as the effects of independent kinematics on the frequency of each transmit node and the delay of each propagation channel. Two scenarios were considered: (i) the conventional receiver-

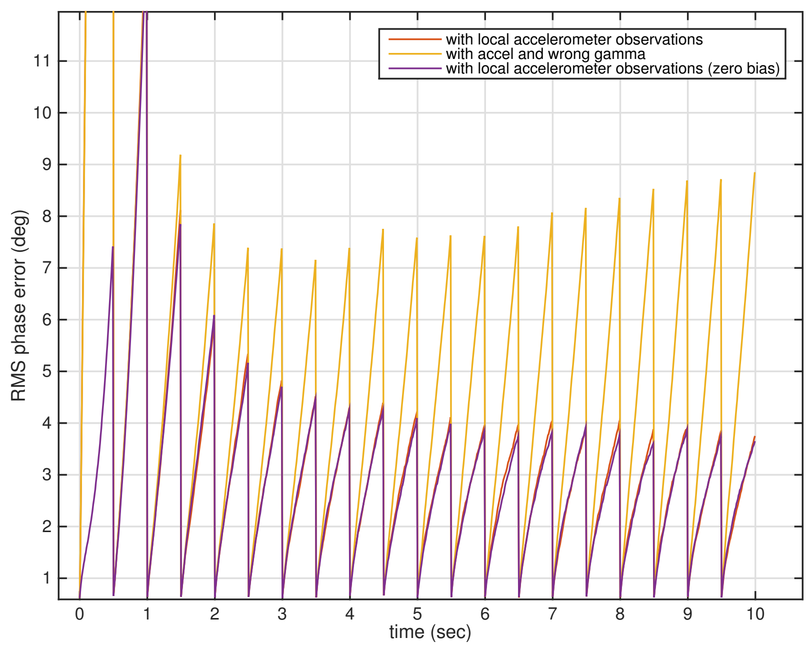

Figure 4.13: Phase error of the Kalman filter state phase prediction when the KF has a wrong sensitivity vector.

coordinated scenario where the time offsets are tracked only through periodic feedback from the receive node and (ii) an accelerometer-assisted scenario where, in addition to the periodic time offset feedback, each receive node also observes measurements from a local accelerometer. Numerical results demonstrated that local accelerometer measurements can improve the ability of each node to track its time offset with respect to the receive node, consequently improving coherence for distributed transmit beamforming and distributed transmit nullforming and also allowing for reduced feedback rates with respect to the conventional feedback-only approach.

The analysis in this chapter was first simplified by the one-dimensional kinematics assumption as depicted in Fig. **??**. In general, with two-dimensional or three-dimensional kinematics, the orientation of the accelerometer with respect to the sensitivity axis of the oscillator [71] and the direction of the propagation channel may be unknown and possibly time-varying. Since the orientation affects elements of the state update matrix $\boldsymbol{F}$ and the process noise covariance $\boldsymbol{C}(T)$, it is critical to generate accurate estimates of these parameters to facilitate optimal tracking and coherent transmission. Methods for accelerator compensation with two-dimensional and three-dimensional kinematics would be an interesting extension to this work.

The three dimensional results are showing that the model we have can be tracked with 3D motion. The assumption that in short intervals only the acceleration in the direction of the receiver affects the propagation path is realistic since the distance to the receiver is much bigger. However, the assumption that the sensitivity vector is known and constant should be modified. As previously discussed, an online way of determining the sensitivity vector should be explored. The error in Fig. 4.13 is again due to Kalman filter parameter mismatch. We have already implemented covariance matrix estimation based on the whitening of the innovation process, using adaptive Kalman filtering.

Chapter 5

Summary and Future Work

In this final chapter the main ideas of this dissertation are summarized and future research directions are identified.

5.1 Conclusions

The synchronization problem is very important in D-MIMO applications. Unlike antenna systems or MIMO applications where frequency compensation can be performed once the signal has been received, the coherency requirement leads to a need for space-time synchronization. By exchanging channel state information, such as phase and frequency offsets, transmit vectors can be computed at transmit nodes to create beams or nulls in a desired direction. In this dissertation we show both why synchronization is important and how it can be used in very large clusters and also how real world applications could reach very strict synchronization goals. The results can be broken into three main sections:

- Chapter2 introduce experimental data and the problem of parameter mismatch for the Kalman filter. We first show the experimental setup, give an idea of what the phase and frequency noises look like and develop methods of determining the noise parameters to match our theoretical 2-state model approximation. The Allan deviation is introduced as a good candidate for characterizing the frequency drift and we show that the theoretical Kalman filter performance matches the experimental results. Then we introduce a covariance whitening method that uses adaptive Kalman filtering to find the parameters that whiten the innovation process. A myriad of results from many experiments are shown. We use both low precision clocks in software defined radios and more expensive oven controlled oscillators to show different performance levels.

- In Chapter 3, theoretical bounds on the beamforming and nullforming performance of very large transmit and receive clusters are derived and tested against intensive simulations. We compared the performance of two scenarios, local and unified tracking in terms of nullforming and beamforming power. Sharper nulls could be steered in a large centralized Kalman filter, while the beamforming performance was similar with either one big Kalman filter or many local ones. For a large system with 100 transmitters and 50 receivers, the benefits were even higher.

- In Chapter 4 the problem of motion is tackled. A moving transmit node is shown to have two effects on a wireless channel. The motion changes the propagation delay between transmitter and receiver and also affects the frequency of the oscillator. We first showed that in one dimensional motion, these effects can be canceled almost entirely by simply using accelerometer measurements. Then, we show that in the three-dimensional case, certain assumption need to be made to have a relatively small state space system that can track and compensate for the motion effects.

A takeaway from this research is that synchronization between nodes can only be achieved over small time intervals and that the more precise an oscillator is, the longer that time interval can be.We show how those intervals can be estimated. The results in Fig. 2.7

show an example of these time intervals can be estimated on the USRP platform.

5.2 Future Work

There are many directions that this research can point to. The Kalman filter is an integral part of this research, and many different implementations can be explored. The use of extended Kalman Filters can provide better estimates. In addition, Kalman filters that have uncertain covariance parameters can be used to mitigate the parameter mismatch problem [82].

Another question that should be answered is if the oscillator stability parameters change with the carrier frequency. The assumptions we made were that the parameters are independent of the carrier frequency, which only serves as a scaling factor.

The 2-state model showed good performance, but in the literature higher clock models are used, which could improve on the model, especially for low cost less stable oscillators [47, 57].

The problem of accelerometer compensation can also be extended to more general cases. Determining the sensitivity vector for an accelerometer could be done in real time using the gyroscopes that exist in inertial measurement units and the orientation could be used to adjust the acceleration vector.

Appendix A

Example of Two Transmitters to One Receiver Beamforming

This experiment is an early testbed for beamforming/nulforming tests using the USRP N210 hardware. In this setup, two USRPs are set to transmit a tone at the same frequency, are hooked up to a passive splitter/combiner and the output is connected to a third receive USRP. Figure A.1 shows the block diagram of the setup. The setup for this experiment uses two function generators. One of the function generators is used as a reference for one transmitter and the receive USRP while the second function generator provides the 10MHz reference for the second transmitter.

In this experiment, two USRPs were setup as follows:

- Carrier Frequency $f_c = 15$ MHz
- CW tone $f = 2000$ Hz
- Duty cycle of 60%

The hardware setup is similar to Figure A.1, but the two transmitters are using the same reference while the receiver is using the second function generator as a reference.

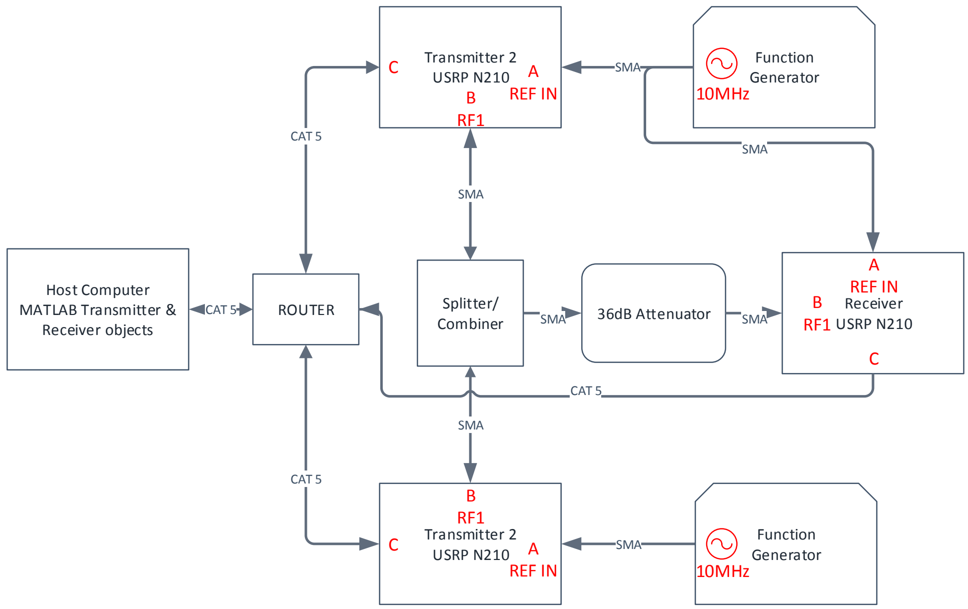

Figure A.1: Block diagram of a 2 to 1 setup

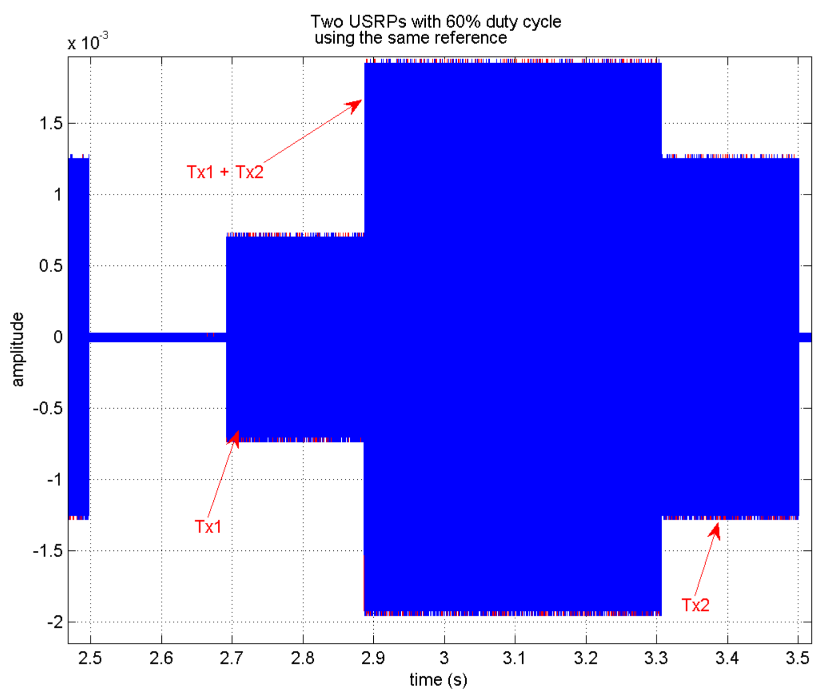

Figure A.2: Demodulated result showing the overlapping of the two transmitters

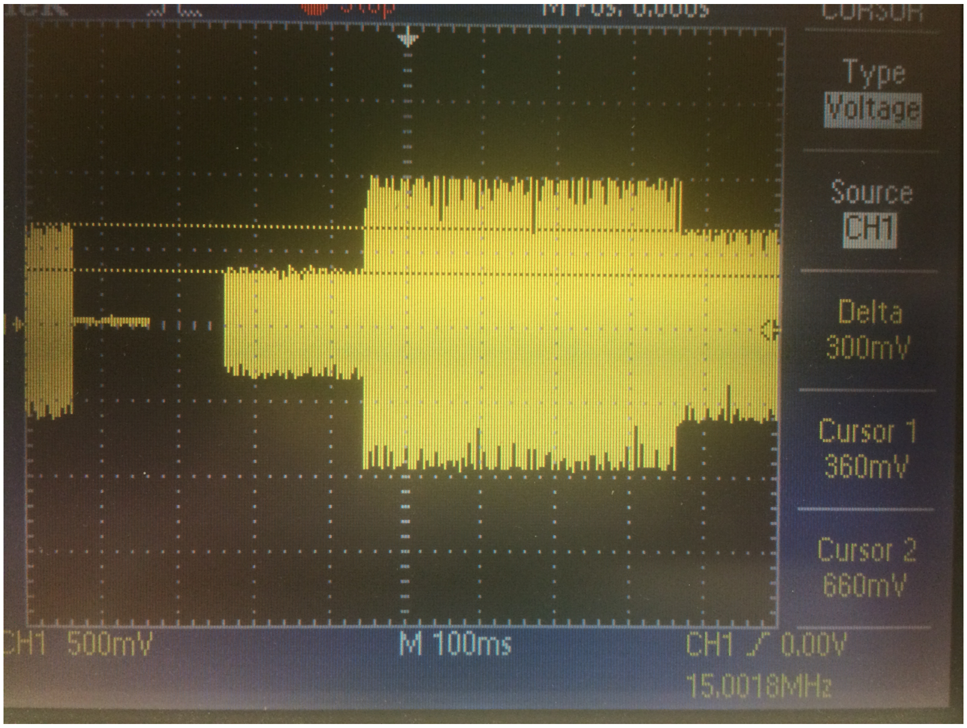

Figure A.3: Oscilloscope capture

In Figure A.2, it can be clearly observed how the two separate USRPs are combining. It is important to observe that because the two transmitters are running off the same clock reference, the frequency stays the same and only the amplitude varies due to the phase offsets. Using trigonometric analysis and by measuring the amplitudes of the respective regions ($Tx1, Tx2, Tx1+Tx2$), it was determined that the phase angle in this experiment was $\phi = 0.5131$ radians.

An oscilloscope capture of the carrier band signal also confirms these results.

We show a testbed for a synchronized transmission setup. We see in this preliminary work that the two signals can be combined constructively if the same clock reference is used. However, the challenge of independent clock source synchronization is still present and it will be tackled in the next chapters.

Appendix B

USRP Detailed Experiment Description

This appendix describes the hardware setup and experimental framework for obtaining very accurate phase and frequency measurements.

B.1 Hardware Setup

Distributed transmission systems require precise estimation and prediction of the channel characterstics. Even in systems with time-invariant channels, the independent oscillators at each node in the distributed transmission system cause the effective channels between each transmitter and receiver to become time-varying. It has been shown that tracking methods, e.g., Kalman filtering, can be quite effective at estimating the time-varying phase and frequency offsets in each independent transmit/receive oscillator pair. In order to implement a Kalman filter for oscillator tracking, however, it is important to have an accurate dynamic model for the systems including, for example, good estimates of the short-term and long-term stability parameters of the oscillators. This document describes an experimental procedure for collecting data that can be subsequently analyzed for the purpose of developing an accurate dynamic model for the oscillators in a distributed transmission system. While the focus is on Universal Software defined Radio Platforms (USRPs), the procedure is general and can be implemented on other hardware.

B.2 Hardware Description

The devices used for this experiments are USRP N210 software defined radios. These are devices that can be configured to modulate and demodulate baseband signals at various carrier frequencies. Data is transferred using an ethernet connection and processing is performed on a separate general purpose computer. Figure B.1 shows a block diagram of the setup used in most of the experiments. It is important to note that the attached function generator blocks are used to generate a 10MHz clock signal source. However, the internal clock reference provided by an internal 100MHz oscillator could also be used.

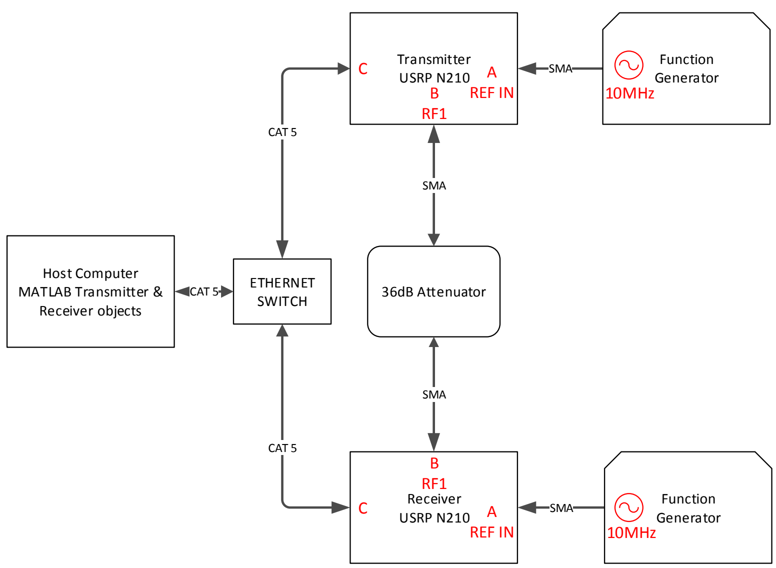

Figure B.1: System block diagram.

The radios used in this experiment have two benefits. One benefit is an FPGA that can be configured to upconvert/downconvert I/Q data and to interface with the host computer. Another benefit is the interchangeable daughterboards that are used to reach different carrier frequency bands, anywhere from DC to 6 GHz. The daughterboards that were used in our experiments are the Basic Tx and Basic Rx, with a frequency range of $1\ \mathrm{MHz} - 250\ \mathrm{MHz}$ and the SBX boards with a frequency range of $400\ \mathrm{MHz} - 4400\ \mathrm{MHz}$. Figure B.2 shows the front of the device with a description of the ports used. Ports A

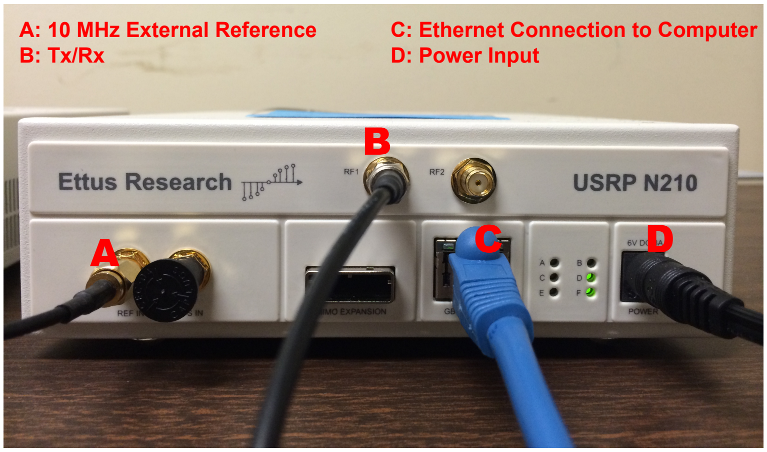

Figure B.2: USRP N210 overview.

and B use SMA cables to connect to the function generator and to the other USRP N210 through the attenuator. The ethernet port allows for gigabit ethernet data transfer between the USRP and the host computer. This connection allows for real time data gathering and analysis even at high sampling rates. The internal clock is a single 100MHz oscillator that is converted to the desired carrier frequencies using PLLs. Our goal is to characterize the behavior of this oscillator as accurately as possible.

Rather than using a separate sampler to record the signals generated by the USRP hardware, we are using two USRPs that have identical oscillators. We believe that by matching the oscillators we will have less uncertainty in the origin of process noise. This way, the combined effect of the two oscillators will statistically be twice the effect of just one oscillator. Thus we can statistically characterize their behavior.

In addition, the USRPs can use an external reference clock. The *Ref In* port accepts a 10 MHz square or sinusoidal input that is used for clock generation. We use function generators which have much better behaved outputs as references to perform additional

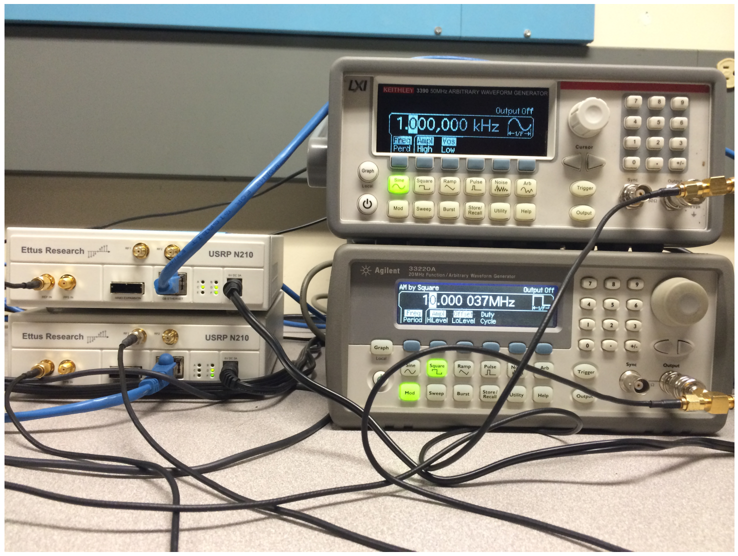

Figure B.3: Test setup.

experiments.

B.3 Experiment Description

Figure B.3 shows an example experiment where two USRP N210s use two separate function generators as external references. The transmit power of the USRP was measured to be approximately -6 dBm and an attenuator of 36 dB was placed on the communication link to have -40 dBm of receive power. The main steps of the experiment are shown below, together with the description of the waveforms at each of the steps.

- In MATLAB, instantiate a *transmit* object and generate a tone at a baseband frequency f.

$$x(t) = A_t e^{j2\pi ft} \tag{B.1}$$

Transmit Object:

```
hSDRu = comm.SDRuTransmitter('IPAddress', '192.168.10.11',
   ...
   'CenterFrequency', 900.0e6, 'InterpolationFactor', 512);
modSignal = exp(1i*2*pi*f*t)';
while 1
   step(hSDRu, modSignal);
end
```

- The transmit USRP modulates the tone with the specified carrier frequency and transmits it over the wire.

$$u(t) = A_t g \cos((2\pi(f + f_c)t + \phi_t(t))) \tag{B.2}$$

Here, $\phi_t(t)$ represents the time-varying phase offset introduced by the transmitter.

- In MATLAB, instantiate a *receive* object and start saving the received data.

Receive Object:

```
hSDRu = comm.SDRuReceiver('192.168.10.12',
   'CenterFrequency', 900e6, ...
   'DecimationFactor', 512,'OutputDataType','double', ...
   'Gain',32,'FrameLength',FrameLength);
data = step(hSDRu);
```

- The receive USRP demodulates the received tone, samples it and sends it to the host computer.

$$y[k] = ge^{j(2\pi fk/f_s)+\phi[k]} \tag{B.3}$$

$\phi[k] = \phi_r[k] - \phi_t[k] + \psi$ represents the total transmitter-receiver phase offset, including the propagation delay ψ.

- The received complex data is stored on the host computer in double precision floating point format for further analysis.

Data collection should be done at a sampling frequency that is at least twice the largest frequency offset of the transmit/receive pair. The largest recorded frequency offset on the USRP N210s was around 45 kHz at a 900 MHz carrier frequency, and on the order of hundreds of MHz for a carrier frequency of 30M Hz. However, the USRP hardware uses a 12-bit ADC with a nominal sampling frequency of 100 MHz that can be later decimated by any value between 4 and 512 leading to a smallest sampling frequency of $100\text{ MHz}/512 = 195,312.5\text{ Hz}$.

All the processing of the data is done on the host computer that is connected to the N210 radios via gigabit ethernet cables. Using MATLAB, transmitter and receiver objects are instantiated on two separate radios. The transmit radio is configured to transmit the 2000Hz complex tone and the receive radio is configured to demodulate the data and save it as a complex variable. Two USRP N210 software defined radios are used with over the wire communication. In these experiments, the *Basic TX* and *Basic RX* daughter boards were used [66]. The parameters used are:

- $fc = 30\text{ MHz}$ - Nominal carrier frequency
- $f = 2000\text{ Hz}$ - Baseband calibration tone
- $f_s = 100 \times 10^6/512\text{ MHz} = 195,312.5\text{ Hz}$ - Sampling frequency of baseband signal

The tone is recorded by the receiver for 70 million samples resulting in around 350 seconds of data. Figure B.4 shows an example of a received complex signal. As mentioned

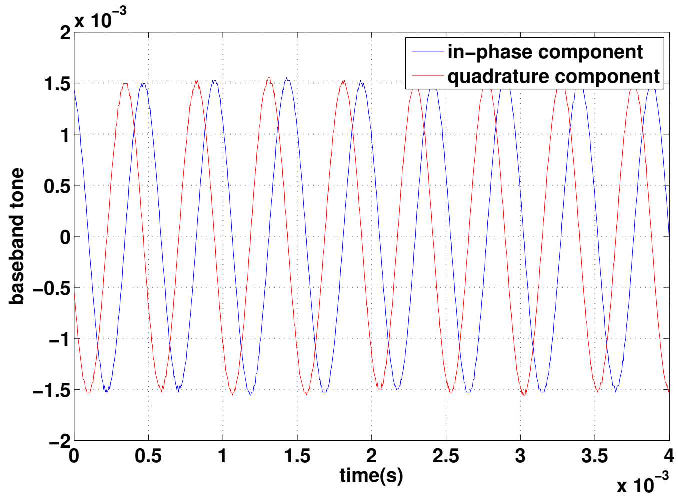

Figure B.4: Complex Measurement

above, the data comes from the 12-bit ADC and is casted into the MATLAB double floating point format. In addition, the radios have automatic gain control (AGC). The complex signal is used for performing phase offset calculations or for frequency estimation.

Bibliography

[1] A. Goldsmith, S. Jafar, N. Jindal, and S. Vishwanath, "Capacity limits of mimo channels," *Selected Areas in Communications, IEEE Journal on*, vol. 21, no. 5, pp. 684 – 702, June 2003.

[2] C. Shepard, H. Yu, N. Anand, E. Li, T. Marzetta, R. Yang, and L. Zhong, "Argos: Practical many-antenna base stations," in *Proceedings of the 18th Annual International Conference on Mobile Computing and Networking*, ser. Mobicom '12. New York, NY, USA: ACM, 2012, pp. 53–64. [Online]. Available: http://doi.acm.org/10.1145/2348543.2348553

[3] S. Xi and M. Zoltowski, "Multiuser transmit beamforming design for sinr maximization in cooperative mimo systems," in *Statistical Signal Processing, 2007. SSP '07. IEEE/SP 14th Workshop on*, Aug 2007, pp. 408–412.

[4] H. Bölcskei, *Space-time wireless systems: from array processing to MIMO communications*. Cambridge University Press, 2006.

[5] L. Zheng and D. Tse, "Diversity and multiplexing: A fundamental tradeoff in multiple antenna channels," *IEEE Trans. on Information Theory*, vol. 49, no. 5, pp. 1073–1096, May 2003.

[6] A. Nosratinia, T. Hunter, and A. Hedayat, "Cooperative communication in wireless networks," *Communications Magazine, IEEE*, vol. 42, no. 10, pp. 74–80, Oct 2004.

[7] D. Gesbert, M. Shafi, D. shan Shiu, P. Smith, and A. Naguib, "From theory to practice: an overview of MIMO space-time coded wireless systems," *IEEE Journal on Selected Areas in Communications*, vol. 21, no. 3, pp. 281–302, April 2003.

[8] G. Foschini, K. Karakayali, and R. Valenzuela, "Coordinating multiple antenna cellular networks to achieve enormous spectral efficiency," *IEE Proceedings on Communications*, vol. 153, no. 4, pp. 548–555, August 2006.

[9] K. Manolakis, S. Jaeckel, V. Jungnickel, and V. Braun, "Channel prediction by doppler-delay analysis and benefits for base station cooperation," in *Vehicular Technology Conference (VTC Spring), 2013 IEEE 77th*, June 2013, pp. 1–6.

[10] E. G. Larsson, F. Tufvesson, O. Edfors, and T. L. Marzetta, "Massive mimo for next generation wireless systems," *submitted to IEEE Communications Magazine*, vol. abs/1304.6690, 2013.

[11] M. Dohler, A. Gkelias, and H. Aghvami, "A resource allocation strategy for distributed mimo multi-hop communication systems," *Communications Letters, IEEE*, vol. 8, no. 2, pp. 99–101, Feb 2004.

[12] R. Mudumbai, G. Barriac, and U. Madhow, "On the feasibility of distributed beamforming in wireless networks," *IEEE Trans. on Wireless Communications*, vol. 6, no. 5, pp. 1754–1763, May 2007.

[13] S. Jafar, S. Vishwanath, and A. Goldsmith, "Channel capacity and beamforming for multiple transmit and receive antennas with covariance feedback," in *Communications, 2001. ICC 2001. IEEE International Conference on*, vol. 7, 2001, pp. 2266 –2270 vol.7.

[14] R. Mudumbai, D.R. Brown III, U. Madhow, and H.V. Poor, "Distributed transmit beamforming: Challenges and recent progress," *IEEE Comm. Mag.*, vol. 47, no. 2, pp. 102–110, Feb. 2009.

[15] R. Preuss and D. Brown, "Retrodirective distributed transmit beamforming with two-way source synchronization," in *Information Sciences and Systems (CISS), 2010 44th Annual Conference on*, march 2010, pp. 1 –6.

[16] R. Preuss and D.R. Brown III, "Two-way synchronization for coordinated multi-cell retrodirective downlink beamforming," *IEEE Trans. Signal Proc.*, vol. 59, no. 11, pp. 5415–27, Nov. 2011.

[17] D. Brown, P. Bidigare, and U. Madhow, "Receiver-coordinated distributed transmit beamforming with kinematic tracking," in *Acoustics, Speech and Signal Processing (ICASSP), 2012 IEEE International Conference on*, Mar. 2012, pp. 5209–5212.

[18] L. Dong, A. Petropulu, and H. Poor, "A cross-layer approach to collaborative beamforming for wireless ad hoc networks," *Signal Processing, IEEE Transactions on*, vol. 56, no. 7, pp. 2981–2993, July 2008.

[19] Y. Tu and G. Pottie, "Coherent cooperative transmission from multiple adjacent antennas to a distant stationary antenna through AWGN channels," in *IEEE Vehic. Techn. Conf. (VTC)*, vol. 1, Birmingham, AL, Spring 2002, pp. 130–134.

[20] G. Barriac, R. Mudumbai, and U. Madhow, "Distributed beamforming for information transfer in sensor networks," in *Proceedings of the 3rd international symposium on Information processing in sensor networks*, ser. IPSN '04. New York, NY, USA: ACM, 2004, pp. 81–88. [Online]. Available: http://doi.acm.org/10.1145/984622.984635

[21] H. Dahrouj and W. Yu, “Coordinated beamforming for the multi-cell multi-antenna wireless system,” in *Conference on Information Sciences and Systems (CISS)*, March 2008, pp. 429–434.

[22] R. Mudumbai, J. Hespanha, U. Madhow, and G. Barriac, “Scalable feedback control for distributed beamforming in sensor networks,” in *IEEE Int. Symp. on Information Theory (ISIT)*, Adelaide, Australia, September 2005, pp. 137–141.

[23] ——, “Distributed transmit beamforming using feedback control,” *IEEE Trans. on Information Theory*, vol. 56, no. 1, pp. 411–426, January 2010.

[24] S. Sayi andli andr, Y.-H. Lu, D. Peroulis, Y. Hu, and B. Jung, “Phase difference and frequency offset estimation for collaborative beamforming in sensor networks,” in *Circuits and Systems (ISCAS), Proceedings of 2010 IEEE International Symposium on*, 30 2010-june 2 2010, pp. 1504 –1507.

[25] S. Sigg and M. Beigl, “Algorithms for closed-loop feedback based distributed adaptive beamforming in wireless sensor networks,” in *Intelligent Sensors, Sensor Networks and Information Processing (ISSNIP), 2009 5th International Conference on*. IEEE, 2009, pp. 25–30.

[26] Y. Jing and H. Jafarkhani, “Network beamforming using relays with perfect channel information,” *IEEE Transactions on Information Theory*, vol. 55, no. 6, pp. 2499 –2517, june 2009.

[27] P. Viswanath, D. N. C. Tse, and R. Laroia, “Opportunistic beamforming using dumb antennas,” *IEEE Trans. Info. Theory*, vol. 48, no. 6, pp. 1277–1294, June 2002.

[28] E. Visotsky and U. Madhow, “Space-time transmit precoding with imperfect feedback,” *Information Theory, IEEE Transactions on*, vol. 47, no. 6, pp. 2632 –2639, sep 2001.

[29] D. Love, J. Heath, R.W., and T. Strohmer, “Grassmannian beamforming for multiple-input multiple-output wireless systems,” in *Communications, 2003. ICC ’03. IEEE International Conference on*, vol. 4, may 2003, pp. 2618 – 2622 vol.4.

[30] O. Somekh, O. Simeone, Y. Bar-Ness, and A. Haimovich, “Cth11-2: Distributed multi-cell zero-forcing beamforming in cellular downlink channels,” in *Global Telecommunications Conference, 2006. GLOBECOM ’06. IEEE*, 27 2006-dec. 1 2006, pp. 1 –6.

[31] S. Jayaweera, “Virtual mimo-based cooperative communication for energy-constrained wireless sensor networks,” *Wireless Communications, IEEE Transactions on*, vol. 5, no. 5, pp. 984 – 989, may 2006.

[32] K. Zarifi, S. Affes, and A. Ghrayeb, “Collaborative null-steering beamforming for uniformly distributed wireless sensor networks,” *IEEE Trans. on Signal Processing*, vol. 58, no. 3, pp. 1889 –1903, Mar. 2010.

[33] A. Kumar, R. Mudumbai, S. Dasgupta, M. Rahman, D. Brown III, M. Madhow, and P. Bidigare, “A scalable feedback mechanism for distributed nullforming with phase-only adaptation,” *Submitted to IEEE Trans. on Signal Processing, currently in review*.

[34] A. Kumar, S. Dasgupta, and R. Mudumbai, “Distributed nullforming without prior frequency synchronization,” in *Control Conference (AUCC), 2013 3rd Australian*, Nov 2013, pp. 207–211.

[35] D.R. Brown III and U. Madhow, “Receiver-coordinated distributed transmit null-forming with channel state uncertainty,” in *Conf. Inf. Sciences and Systems (CISS2012)*, Mar. 2012, to appear.

[36] H. Ochiai, P. Mitran, H. Poor, and V. Tarokh, “Collaborative beamforming for distributed wireless ad hoc sensor networks,” *Trans. Sig. Proc.*, vol. 53, no. 11, pp. 4110–4124, Nov. 2005. [Online]. Available: http://dx.doi.org/10.1109/TSP.2005.857028

[37] D.R. Brown III, P. Bidigare, S. Dasgupta, and U. Madhow, “Receiver-coordinated zero-forcing distributed transmit nullforming,” in *Statistical Signal Processing Workshop (SSP), 2012 IEEE*, Aug. 2012, pp. 269–272.

[38] P. Bidigare, U. Madhow, R. Mudumbai, and D. Scherber, “Attaining fundamental bounds on timing synchronization,” in *Acoustics, Speech and Signal Processing (ICASSP), 2012 IEEE International Conference on*, March 2012, pp. 5229–5232.

[39] M.-H. Hsieh and C.-H. Wei, “A low-complexity frame synchronization and frequency offset compensation scheme for ofdm systems over fading channels,” *Vehicular Technology, IEEE Transactions on*, vol. 48, no. 5, pp. 1596–1609, Sep 1999.

[40] J. Elson, L. Girod, and D. Estrin, “Fine-grained network time synchronization using reference broadcasts,” *ACM SIGOPS Operating Systems Review*, vol. 36, pp. 147–163, 2002.

[41] D.R. Brown III and H.V. Poor, “Time-slotted round-trip carrier synchronization for distributed beamforming,” *IEEE Trans. on Signal Processing*, vol. 56, no. 11, pp. 5630–5643, November 2008.

[42] D. Brown, A. Klein, and R. Wang, “Monotonic mean-squared convergence conditions for random pairwise consensus synchronization in wireless networks,” *Signal Processing, IEEE Transactions on*, vol. 63, no. 4, pp. 988–1000, Feb 2015.

[43] D. Brown and R. David, "Receiver-coordinated distributed transmit nullforming with local and unified tracking," in *Acoustics, Speech and Signal Processing (ICASSP), 2014 IEEE International Conference on*, May 2014, pp. 1160–1164.

[44] D. Brown and A. Klein, "Precise timestamp-free network synchronization," in *Information Sciences and Systems (CISS), 2013 47th Annual Conference on*, March 2013, pp. 1–6.

[45] M. M. Rahman, S. Dasgupta, and R. Mudumbai, "A distributed consensus approach to synchronization of rf signals," in *IEEE Statistical Signal Processing Workshop (SSP)*, Aug. 2012, pp. 281–284.

[46] D.R. Brown III, G. Prince, and J. McNeill, "A method for carrier frequency and phase synch. of two autonomous cooperative transmitters," in *IEEE Signal Proc. Advances in Wireless Comm. (SPAWC)*, New York, NY, June 5-8, 2005, pp. 278–282.

[47] H. Kim, X. Ma, and B. R. Hamilton, "Tracking low-precision clocks with time-varying drifts using kalman filtering," *IEEE/ACM Trans. Netw.*, pp. 257–270, 2012.

[48] G. Giorgi and C. Narduzzi, "Performance analysis of kalman-filter-based clock synchronization in ieee 1588 networks," *IEEE T. Instrumentation and Measurement*, pp. 2902–2909, 2011.

[49] H. Heffes, "The effect of erroneous models on the kalman filter response," *Automatic Control, IEEE Transactions on*, vol. 11, no. 3, pp. 541–543, Jul 1966.

[50] M. Saha, B. Goswami, and R. Ghosh, "Two novel costs for determining the tuning parameters of the Kalman Filter," *ArXiv e-prints*, Oct. 2011.

[51] P. Bidigare, M. Oyarzun, D. Raeman, D. Cousins, D. Chang, R. O'Donnell, and D.R. Brown III, "Implementation and demonstration of receiver-coordinated dis-

tributed transmit beamforming across an ad-hoc radio network," in *Proceedings of the 46th Asilomar Conference on Signals, Systems, and Computers*, Pacific Grove, CA, November 4-7, 2012, p. tbd.

[52] F. Quitin, U. Madhow, M. Rahman, and R. Mudumbai, "Demonstrating distributed transmit beamforming with software-defined radios," in *World of Wireless, Mobile and Multimedia Networks (WoWMoM), 2012 IEEE International Symposium on a*, June 2012, pp. 1–3.

[53] L. Galleani, "A tutorial on the 2-state model of the atomic clock noise," *Metrologia*, vol. 45, no. 6, pp. S175–S182, Dec. 2008.

[54] G. Giorgi and C. Narduzzi, "Performance analysis of kalman filter-based clock synchronization in IEEE 1588 networks," in *International IEEE Symposium on Precision Clock Synchronization for Measurement, Control, and Communication*, October 12-16 2009, pp. 1–6.

[55] D. Allan, "Time and frequency (time-domain) characterization, estimation, and prediction of precision clocks and oscillators," *Ultrasonics, Ferroelectrics, and Frequency Control, IEEE Transactions on*, vol. 34, no. 6, pp. 647–654, Nov 1987.

[56] D. Georgakaki, C. Mitsas, and H. Polatoglou, "Spectral analysis and Allan variance calculation in the case of phase noise," *Journal of Concrete And Applicable Mathematics (JCAAM)*, vol. 9, no. 3, pp. 270–277, Feb. 2012.

[57] C. Zucca and P. Tavella, "The clock model and its relationship with the allan and related variances," *Ultrasonics, Ferroelectrics and Frequency Control, IEEE Transactions on*, vol. 52, no. 2, pp. 289 –296, feb. 2005.

[58] M. A. Lombardi, "Fundamentals of time and frequency," *The Mechatronics Handbook*, 2002.

[59] "Characterization of frequency and phase noise," Report 580 of the International Radio Consultative Committee (C.C.I.R), Tech. Rep., 1986.

[60] R. E. Kalman, "A new approach to linear filtering and prediction problems," *Journal of Fluids Engineering*, vol. 82, no. 1, pp. 35–45, 1960.

[61] D. Simon, "Kalman filtering with state constraints: a survey of linear and nonlinear algorithms," *Control Theory Applications, IET*, vol. 4, no. 8, pp. 1303–1318, August 2010.

[62] P. Closas, C. Fernandez-Prades, and J. Vila-Valls, "Multiple quadrature kalman filtering," *Signal Processing, IEEE Transactions on*, vol. 60, no. 12, pp. 6125–6137, Dec 2012.

[63] R. Mehra, "On the identification of variances and adaptive kalman filtering," *Automatic Control, IEEE Transactions on*, vol. 15, no. 2, pp. 175–184, Apr 1970.

[64] B. J. Odelson, M. R. Rajamani, and J. B. Rawlings, "A new autocovariance least-squares method for estimating noise covariances," *Automatica*, vol. 42, no. 2, pp. 303 – 308, 2006. [Online]. Available: http://www.sciencedirect.com/science/article/pii/S0005109805003262

[65] (2015, Jan.) Usrp n210. [Online]. Available: https://www.ettus.com/product/details/UN210-KIT

[66] (2014, Jun.) Rf daughterboards. [Online]. Available: https://www.ettus.com/product/details/BasicTX

[67] "Rakon RFPO45 SMD oven controlled crystal oscillator datasheet," 2009. [Online]. Available: http://www.rakon.com/Products/Public/Documents/ Specifications/RFPO45.pdf

[68] J. Hoydis, S. ten Brink, and M. Debbah, “Massive mimo: How many antennas do we need?” in *Communication, Control, and Computing (Allerton), 2011 49th Annual Allerton Conference on*, 2011, pp. 545–550.

[69] Y. Bar-Shalom, X. R. Li, and T. Kirubarajan, *Estimation with Applications to Tracking and Navigation*. John Wiley and Sons, 2001.

[70] D. Brown, R. Mudumbai, and S. Dasgupta, “Fundamental limits on phase and frequency tracking and estimation in drifting oscillators,” in *Acoustics, Speech and Signal Processing (ICASSP), 2012 IEEE International Conference on*, Mar. 2012, pp. 5225–5228.

[71] R. Filler, “The acceleration sensitivity of quartz crystal oscillators: a review,” *Ultrasonics, Ferroelectrics, and Frequency Control, IEEE Transactions on*, vol. 35, no. 3, pp. 297–305, May 1988.

[72] M. St-Pierre and D. Gingras, “Comparison between the unscented kalman filter and the extended kalman filter for the position estimation module of an integrated navigation information system,” in *Intelligent Vehicles Symposium, 2004 IEEE*, June 2004, pp. 831–835.

[73]

[74] G. Hexner and H. Weiss, “An extended kalman filter with a computed mean square error bound,” in *Decision and Control (CDC), 2014 IEEE 53rd Annual Conference on*, Dec 2014, pp. 5008–5014.

[75] W. Klepczynski and P. Ward, “Frequency stability requirements for narrow band receivers,” in *32nd Annual Precise Time and Time Interval Meeting*, November 2000.

[76] C.-T. Chen, *Linear System Theory and Design*. Oxford University Press, 1999.

[77] S. M. Kay, *Fundamentals of Statistical Signal Processing Volume I: Estimation Theory*. Upper Saddle River, NJ: Prentice Hall, 1993.

[78] A. Weiss and E. Weinstein, "Fundamental limitations in passive time delay estimation–part i: Narrow-band systems," *Acoustics, Speech and Signal Processing, IEEE Transactions on*, vol. 31, no. 2, pp. 472 – 486, apr 1983.

[79] P. Bidigare, S. Pruessing, D. Raeman, D. Scherber, U. Madhow, and R. Mudumbai, "Initial over-the-air performance assessment of ranging and clock synchronization using radio frequency signal exchange," in *IEEE Stat. Signal Processing Workshop (SSP)*, Aug. 2012, pp. 273–276.

[80] "Analog Devices ADXL103/ADXL203 Precision Dual-Axis iMEMS Accelerometer Datasheet," 2014. [Online]. Available: http://www.analog.com/static/imported-files/data_sheets/ADXL103_203.pdf

[81] Y. Noam and A. Goldsmith, "Blind null-space learning for mimo underlay cognitive radio with primary user interference adaptation," *Wireless Communications, IEEE Transactions on*, vol. 12, no. 4, pp. 1722–1734, April 2013.

[82] L. Shi, K. Johansson, and R. Murray, "Kalman filtering with uncertain process and measurement noise covariances with application to state estimation in sensor networks," in *IEEE International Conference on Control Applications (CCA'07)*, Oct 2007, pp. 1031–1036.